Jül-4328

Institute for Nuclear Physics (IKP-4)

Investigation and Optimization of Transverse Non-Linear Beam Dynamics in the High-Energy Storage Ring HESR

Dominic Markus Welsch

Mitglied der Helmholtz-Gemeinschaft

JÜLICH
FORSCHUNGSZENTRUM

Investigation and Optimization of Transverse Non-Linear Beam Dynamics in the High-Energy Storage Ring HESR

Dominic Markus Welsch

Berichte des Forschungszentrums Jülich; 4328
ISSN 0944-2952
Institute for Nuclear Physics (IKP-4)
Jül-4328

Vollständig frei verfügbar im Internet auf dem Jülicher Open Access Server (JUWEL)
unter http://www.fz-juelich.de/zb/juwel

Zu beziehen durch: Forschungszentrum Jülich GmbH · Zentralbibliothek, Verlag
D-52425 Jülich · Bundesrepublik Deutschland
☎ 02461 61-5220 · Telefax: 02461 61-6103 · e-mail: zb-publikation@fz-juelich.de

Abstract

The High-Energy Storage Ring HESR is part of the upcoming Facility for Antiproton and Ion Research FAIR which is planned as a major extension to the present facility of the Helmholtzzentrum für Schwerionenforschung (GSI) in Darmstadt. The HESR will provide antiprotons in the momentum range from 1.5 to 15 GeV/c for the internal target experiment PANDA. Long beam life time and a minimum of beam loss is inevitable due to the demanding requirements of PANDA in terms of beam quality, luminosity and limited production rate of antiprotons. Therefore, an effective closed orbit correction and a sufficiently large dynamic aperture of the HESR are crucial.

The expected misalignments of beam guiding magnets have been estimated and used to simulate the closed orbit in the HESR. A closed orbit correction scheme has been developed for different ion-optical settings of the HESR and numerical simulations have been performed to validate the closed orbit correction scheme. The proposed closed orbit correction method which utilizes the orbit response matrix has been benchmarked at the Cooler Synchrotron COSY of the Forschungszentrum Jülich.

A chromaticity correction scheme for the HESR has been developed using sextupole magnets in order to reduce tune spread and thus avoid emittance growth caused by betatron resonances. The chromaticity correction scheme has been optimized utilizing dynamic aperture calculations. The estimated field errors of the HESR dipole and quadrupole magnets have been taken into account and investigations concerning their optimization have been carried out. The ion-optical settings of the HESR have been improved using, besides dynamic aperture calculations, the technique of frequency map analysis. The related diffusion coefficient was also used to predict long-term stability based on short-term particle tracking.

With a reasonable reduction of the quadrupole magnets field errors and a different choice of tunes, the dynamic aperture was improved by roughly a factor two. The inner area of the dynamic aperture where the particle motion is stable on a long-term scale increased and includes more than 3σ beam size and the specified maximum closed orbit deviations.

Contents

Chapter 1

Introduction

Experiments with particle accelerators have proven to be an essential instrument for nuclear and particle physics to investigate the structure and the interaction of matter. Such investigations are usually based on scattering experiments where particle beams with known energy are directed onto targets where interactions take place. The reaction products can be observed and measured with particle detectors. This information is used to reconstruct the reactions and to determine properties of elementary particles and the underlying interactions in the subatomic regime.

The kind of accelerated particles and their energy are determined by the physics and the experimental setup. There are primary beams with e.g. protons or electrons and also secondary beams with e.g. antiprotons. For the latter a primary beam is directed onto a target of special material and the interaction products are collected and phase space cooled to form a secondary beam.

The Facility for Antiproton and Ion Research (FAIR) has been proposed by the Helmholtzzentrum für Schwerionenforschung (GSI) in Darmstadt and will provide a multitude of different particle beams (e.g. antiproton beams, beams with rare isotopes or heavy ions) for a wide range of scientific experiments [1, 2]. The FAIR project is planned to be a major extension for the present accelerator facility at GSI where the High-Energy Storage Ring HESR [3] is is one of the new particle accelerators dedicated to antiproton physics. It will deliver antiprotons in the momentum range from 1.5 to 15 GeV/c for the internal target experiment PANDA [4]. The leading institute of a consortium planning the HESR is the nuclear physics institute (IKP) of the Forschungszentrum Jülich.

For the HESR, a long beam life time and a minimum of beam loss is inevitable. This is on one hand due to the demanding requirements of PANDA in terms of beam quality and luminosity and on the other due to usage of antiproton beams where the production rate is a limiting factor. Therefore an effective closed orbit correction and a sufficiently large dynamic aperture are crucial. Investigations and concluding results concerning both topics are covered by this thesis.

In chapter two, the theoretical basis of this thesis described. It is divided into two parts. The first part covers linear beam dynamics. The basic concepts of accelerator physics like twiss parameters and chromaticity are explained. For closed orbit correction, the orbit response matrix method will be used and is therefore

discussed together with the ways of its applications. The second part of this chapter is dedicated to non-linear beam dynamics. Driving terms are introduced to explain the influence of magnets on betatron resonances which affect the beam motion. In order to quantify stability of beam motion, the dynamic aperture is extensively used since it separates stable from unstable one. The calculation of the dynamic aperture is described and the technique of frequency map analysis which is based on the KAM theorem introduced. The definition of the related diffusion coefficient completes this chapter.

The High-Energy Storage Ring HESR with its internal target experiment PANDA as well as the embedding in FAIR is discussed in chapter three. Furthermore, the HESR layout is described together with the HESR magnets and their alignment. Since PANDA has strong requirements on beam quality and luminosity, the beam parameters and the modes of HESR operation are presented. In addition to that, the ion-optical properties of the HESR can be found in this chapter. Finally, the HESR is compared with the Cooler Synchrotron COSY [5, 6] of the Forschungszentrum Jülich to justify benchmarking experiments.

The fourth chapter deals with closed orbit investigations. Magnet alignment errors are estimated for HESR to simulate the closed orbit. A closed orbit correction scheme is developed in order to correct the resulting closed orbit deviations. Additionally, numerical simulations are used to validate the closed orbit correction scheme. At various location in the HESR, the transverse position of the antiproton beam and its angle have to be adjustable. Therefore, local closed orbit bumps are investigated. In addition to the HESR investigations, the measurement of the orbit response matrix at COSY and results of its application for a closed orbit correction is discussed.

Chapter five contains non-linear beam dynamics studies. A chromaticity correction scheme is developed for the HESR and its optimization is described. The field errors of the main HESR magnets are presented and used for non-linear beam dynamics calculations. The non-linear beam dynamics is investigated for the two main experimental setups of the HESR. This is done by using dynamic aperture calculations and frequency map analysis which are used to optimize the ion-optics of the HESR and the field errors of the main HESR magnets.

In the last chapter the results of this thesis are summarized and discussed. Furthermore, an outlook of future topics is given.

Chapter 2

Theory

Electro-magnetic fields are utilized in particle accelerators to guide and accelerate charged particles. If single particle trajectories are assumed which means that no interaction between particles take place, then the only forces being considered are created by external electro-magnetic fields of the accelerator. Electric fields are used to accelerate and decelerate particles. In order to guide a particle beam electric and magnetic fields can be applied although the usage of electric fields is restricted to low beam energies. The motion of particles is solely determined by the setup of these electro-magnetic field and can be classified into linear and non-linear beam dynamics.

2.1 Linear beam dynamics

Linear beam dynamics restricts the influence of electro-magnetic fields to constant or linear forces. Ideally, all particles in an accelerator should move on a single trajectory which is solely determined by the setup of electro-magnetic fields. If this reference trajectory is curved, bending forces are necessary to deflect the particles. But in reality, most particle will not move of the reference trajectory. Their trajectories deviate slightly from the reference trajectory. Therefore, a focusing force has to be applied.

Both, the bending and the focusing forces can be accomplished with electro-magnetic fields.

2.1.1 Charged particles in electro-magnetic fields

All electro-magnetic forces acting on charged particles with charge q and velocity $\vec{v}$ are described by the *Lorentz* force

$$\vec{F}_{\text{Lorentz}} = q(\vec{E} + \frac{\vec{v}}{c} \times \vec{B}) \tag{2.1}$$

where the electrical and the magnetic fields are denoted by $\vec{E}$ and $\vec{B}$. The *Lorentz* force is conservative and holds independently of the considered coordinate system.

2.1.2 Co-moving coordinate system

A co-moving coordinate system (x, y, s) is customarily used in accelerator physics [7] which is righthanded and orthogonal (see Fig. 2.1). The local curvature of the trajectory is denoted with ρ whereas the angle $\theta = \frac{2\pi}{C}$ corresponds to the angular advance in a ring accelerator with C being the circumference of the particle accelerator. A trajectory of a single particle can be expressed in deviations from the reference trajectory in all three directions (x, y, s). The horizontal plane is defined to be the (x, s)-plane because particle accelerators are typically built planar.

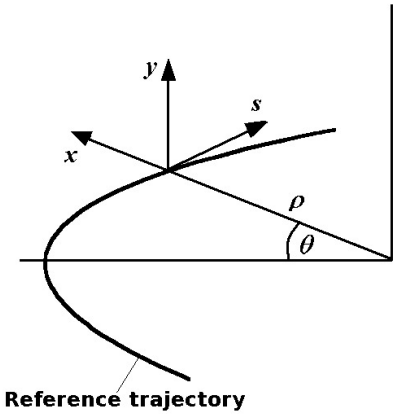

Figure 2.1: Co-moving coordinate system for charged particles in a ring accelerator. The direction of movement is along s. The transverse deviations are given in x and y. The local radius of curvature is denoted by ρ whereas the angular advance is θ.

2.1.3 Hamiltonian

The particle motion is determined by six coordinates at all times: three generalized coordinates $q_i(t)$ and three conjugate momenta $p_i(t)$ where $i = x,\, y,\, s$. All six coordinates span a phase space of the particle motion. The phase space volume is constant although not necessarily in the same shape if only conservative forces are applied. This is described by Liouville's theorem.

The Hamiltonian $\mathcal{H}(q_i,\, p_i,\, t)$ which describes the system under investigation connects the time derivatives of conjugate coordinates:

$$\dot{p} = -\frac{\partial \mathcal{H}}{\partial q},\ \dot{q} = \frac{\partial \mathcal{H}}{\partial p}. \tag{2.2}$$

These differential equations are known as Hamilton equations.

A charged particle in presence of electro-magnetic fields is influenced by two kinds of potentials: a vector potential $\vec{A}(\vec{q},\, t)$ and a scalar potential $\phi(\vec{q},\, t)$. Both types are connected to the electrical and magnetic fields by

$$\vec{E} = -\vec{\nabla}\phi - \frac{1}{c}\frac{\partial \vec{A}}{\partial t},\ \vec{B} = \vec{\nabla} \times \vec{A}. \tag{2.3}$$

The Hamiltonian has the following form in the lab frame

$$\mathcal{H}(q_i,\, p_i,\, t) = \frac{1}{2m}\left(\vec{p} - \frac{q}{c}\vec{A}(\vec{q},\, t)\right)^2 + q\phi(\vec{q},\, t). \tag{2.4}$$

Restricting to a vector potential due to magnetic fields and changing into the co-moving frame, the phase space coordinates are $(x,\, p_x,\, y,\, p_y,\, -p_t,\, ct)$ and depend on s. The Hamiltonian in the co-moving frame reads

$$\begin{aligned}\mathcal{H}(x,\, p_x,\, y,\, p_y,\, -p_t,\, ct;\, s) = &-\left[1 + h_{ref}(s)x\right] \\ &\times \left\{\frac{q}{p_0}A(s) + \sqrt{1 - \frac{2}{\beta}p_t + p_t^2 - \left[p_x - \frac{q}{p_0}A_x(s)\right]^2 - \left[p_y - \frac{q}{p_0}A_y(s)\right]^2}\right\}\end{aligned} \tag{2.5}$$

where

$$p_t \equiv -\frac{E - E_0}{p_0 c},\; h_{ref}(s) \equiv \frac{1}{\rho_{ref}(s)},\; \beta \equiv \frac{v}{c} \tag{2.6}$$

and t the absolute time of flight. Its canonical momentum p_t depends on the difference of particle kinetic energy E and the reference kinetic energy E_0 as well as on the reference momentum p_0. The local radius of curvature along the reference trajectory is denoted with ρ_{ref}. A change of variables to introduce the relative momentum deviation

$$\delta \equiv \frac{p - p_0}{p_0} \tag{2.7}$$

leads to the Hamiltonian

$$\begin{aligned}\mathcal{H}(x,\, p_x,\, y,\, p_y,\, \delta,\, ct;\, s) = &-\left[1 + h_{ref}(s)x\right] \\ &\times \left\{\frac{q}{p_0}A(s) + \sqrt{(1+\delta)^2 - \left[p_x - \frac{q}{p_0}A_x(s)\right]^2 - \left[p_y - \frac{q}{p_0}A_y(s)\right]^2}\right\}\end{aligned} \tag{2.8}$$

where the conjugate coordinate to δ is denoted with T and is given by the canonical transformation

$$-cT = -\frac{\beta\,(1+\delta)\,ct}{\sqrt{1 + \beta^2\,(2\delta + \delta^2)}}. \tag{2.9}$$

This implies that the conjugate coordinate of δ and the time of flight are not equal.

A transformation of variables to the so called action-angle variables J_i and ϕ_i which are defined by

$$J_i = \frac{1}{2\pi}\oint p_i dq_i = const. \tag{2.10}$$

over one oscillation period leads to a Hamiltonian which depends only on the action J_i and not on the angle ϕ_i. The following relations fulfill the last equation:

$$\begin{aligned} q_i &= \sqrt{2J_i}\cdot\cos(\phi_i) \\ p_i &= -\sqrt{2J_i}\cdot\sin(\phi_i) \end{aligned} \tag{2.11}$$

2.1.4 Multipolar expansion of magnetic fields

For simplicity, all magnetic fields are assumed to be orthogonal to the direction of movement. This means that all magnets have only transverse components. The vector potential $\vec{A}(x, y, s)$ can be reduced to the longitudinal component $A_s(x, y, s)$. The charge-free *Laplace* equation of this potential A_s in a cylinder symmetrical coordinate system (r, φ, s) is given by

$$\triangle A_s = \frac{\partial^2 A_s}{\partial r^2} + \frac{1}{r}\frac{\partial A_s}{\partial r} + \frac{1}{r^2}\frac{\partial^2 A_s}{\partial \varphi^2} + \frac{\partial^2 A_s}{\partial z^2} \equiv 0. \tag{2.12}$$

The potential can be expanded in a *Taylor* series for $r = 0$ in this coordinate system to

$$A_s(r, \varphi, s) = \frac{cp_0}{q} \sum_{n>0} \frac{1}{n!} A_n(s) r^n e^{in\varphi}. \tag{2.13}$$

The sub index n should be positive to circumvent non-physical singularities for $r \to 0$. The coefficients A_n can be derived from the *Laplace* equation.

Both, the real and the imaginary part represent a solution and differ by a rotation only. Particle accelerators are typically built planar which motivates the notion of upright (imaginary part) and skewed (real part) magnets. The so called harmonics b_n (imaginary part) and a_n (real part) of a magnetic field are represented by the coefficients $A_n(s) = b_n(s) + ia_n(s)$. The expansion of the magnetic field in harmonics is given by

$$B_y(s) + iB_x(s) = B\rho \sum_{n>0} \left[b_n(s) + ia_{n(s)}\right] \left(re^{i\varphi}\right)^n. \tag{2.14}$$

The sub index n represents a multipole component with $(2n+2)$ poles and $B\rho = \frac{cp_0}{q}$ is known as magnetic rigidity. Field errors of magnets can also be expressed in harmonics. They are usually given in terms of 10^{-4} and are expanded for a specific radius R_0 [8]

$$B_y(s) + iB_x(s) = 10^{-4} B_{R_0} \sum_{n=0}^{\infty} \left[b_n(s) + ia_n(s)\right] e^{in\varphi} \left(\frac{r}{R_0}\right)^n \tag{2.15}$$

where B_{R_0} is the main magnetic field at the radius of expansion.

There is no dependence of the magnetic field on the radius r for $n = 0$ which refers to a constant magnetic field. A particle travelling through such a magnetic field is bent. This kind of magnetic field is related to a dipole magnet. An upright dipole magnet has a vertical magnetic field component only. The second for linear beam dynamics important type is the quadrupole magnet which refers to $n = 1$. Its field has a linear dependence on the radius and is used to focus the beam. It is obvious that an upright quadrupole magnet can focus the beam in one transverse plane only. The beam is defocused in the other one. Therefore at least two quadrupole magnets forming a doublet have to be used to get a net focusing effect in both transverse planes.

Magnets with $n \geq 2$ are related to non-linear beam dynamics but cannot be avoided in an accelerator since

- it is not possible to design and build magnets having only one single magnetic field geometry (field errors)
- higher-order magnetic multipoles may be helpful or even necessary (e.g. for chromaticity correction).

2.1.5 Linear equation of motion and betatron functions

The expansion of the *Hamiltonian* to the second order in the vector potential and thus in the magnetic field, neglecting momentum deviations, and combining the Hamilton's equations lead to the homogeneous differential equation of motion[1]

$$u'' + K(s)u = 0 \tag{2.16}$$

where $K(s) = \frac{1}{\rho_u^2(s)} + k_u(s)$ is the local property of the magnets and u a transverse coordinate (x or y). The functions $\rho(s)$ and $k(s)$ are also periodic and depend on the local radius of curvature and the focusing strength. The homogeneous equation of motion is similar to the one of the harmonic oscillator. Thus a periodic solution can be found by applying the Floquet's theorem with the ansatz [9]

$$u(s) = \sqrt{\varepsilon}\sqrt{\beta_u(s)}\cos(\psi(s) - \psi_{u,0}). \tag{2.17}$$

The integration constants ε and $\psi_{u,0}$ are defined by the system under investigation. The location dependent variable $\beta_u(s)$ is called betatron amplitude. The second order derivative of $u(s)$ reads

$$\begin{aligned} u''(s) = +\sqrt{\varepsilon}\frac{\beta_u\beta_u'' - \frac{1}{2}\beta_u^2}{2\beta_u^{\frac{2}{3}}}\cos\left(\psi_u - \psi_{u,0}\right) - \sqrt{\varepsilon}\frac{\beta_u'}{\sqrt{\beta_u}}\sin\left(\psi_u - \psi_{u,0}\right)\psi_u' \\ - \sqrt{\varepsilon}\sqrt{\beta_u}\sin\left(\psi_u - \psi_{u,0}\right)\psi_u'' - \sqrt{\varepsilon}\sqrt{\beta_u}\cos\left(\psi_u - \psi_{u,0}\right)\psi_u'^2. \end{aligned} \tag{2.18}$$

Putting both u and u'' into equation 2.16 and sorting for sine and cosine terms, the coefficients have to vanish for all phases:

$$\frac{1}{2}\left(\beta_u\beta_u'' - \frac{1}{2}\beta_u'^2\right) - \beta_u^2\psi_u'^2 + \beta_u^2 K(s) = 0 \tag{2.19}$$

$$\beta_u'\psi_u' + \beta_u\psi_u'' = 0. \tag{2.20}$$

Integrating latter equation and setting the integration constant to one, the phase $\psi_u(s)$ is given by

$$\psi_u(s) = \int_0^s \frac{d\tilde{s}}{\beta_u(\tilde{s})} + \psi_{u,0}. \tag{2.21}$$

[1] This kind of equation of motion for periodical systems like accelerator rings are called *Hills* differential equations

The phase difference of two locations is called phase advance. The so called twiss parameters include besides the betatron amplitude[2] two additional ones:

$$\alpha_u = -\frac{1}{2}\beta'_u \qquad and \tag{2.22}$$

$$\gamma_u = \frac{(1+\alpha_u^2)}{\beta_u}. \tag{2.23}$$

The twiss parameters describe the motion of particles around the reference trajectory which is called betatron oscillation. For ring accelerators, the number of oscillations per turn is called tune Q_u

$$Q_u = \frac{\psi_{u,ring}}{2\pi} \tag{2.24}$$

where $\psi_{u,ring}$ is the phase advance per turn.

Equation 2.19 can be rewritten in a simplified form:

$$\beta''_u + 2K\beta_u = 0 \Longleftrightarrow K\beta_u - \gamma_u = \alpha'_u. \tag{2.25}$$

The phase of u and u' has to be eliminated in order to find the invariant of the particle motion:

$$\gamma_u u^2 + 2\alpha_u u u' + \beta_u u'^2 = \varepsilon_u \tag{2.26}$$

where ε is named *Courant-Snyder* invariant or single particle emittance. This emittance is the invariant of the particle motion and is a conserved quantity for a constant particle energy. The single particle emittance decreases during acceleration and increases during deceleration. This dependence on the particle energy effect is called adiabatic damping. In order to be able to compare emittances for different particle energies, an energy-independent emittance $\varepsilon_{u,normalized}$ is introduced

$$\varepsilon_{\mathrm{u,normalized}} = \beta\gamma\varepsilon_u. \tag{2.27}$$

Equation 2.26 matches an ellipse equation with area $\pi\varepsilon$. Figure 2.2 shows the phase space ellipse of the motion of a single particle. The phase space ellipse changes its shape and rotates with the twiss parameters while the particle moves along its trajectory. A beam emittance can be defined to parametrize an ensemble of particles in a beam. It covers the whole phase space area of all single particle emittances. The emittance of a beam can be specified e.g. in standard deviations or as a 90% beam emittance[3]. The choice strongly depends on the particle distribution of the beam.

The transverse beam width at a location s depends on the transverse beam emittance ε_u and the local beta function $\beta_u(s)$:

$$\sigma_u = \sqrt{\beta_u \varepsilon_u}. \tag{2.28}$$

It can be specified according to the beam emittance and the phase space distribution.

[2] also called beta function

[3] contains 90% of the particles inside the beam

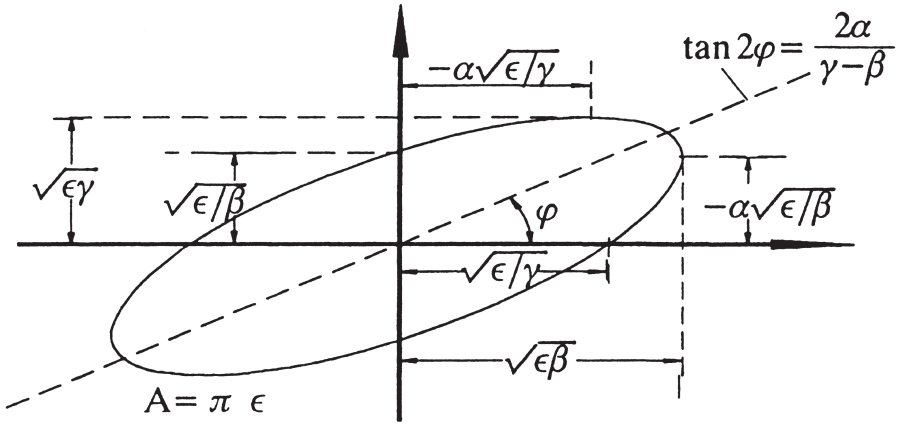

Figure 2.2: Phase space ellipse of the motion of a single particle in one transverse plane. The area A of the phase space ellipse is given by $A = \pi\varepsilon$ where ε is the emittance.

2.1.6 Matrix formalism

The linear transverse equations of motion including momentum deviations in first order can be written as

$$\begin{aligned} x' &= \tfrac{p_x}{1+\delta} + \mathcal{O}(2) \\ p'_x &= \tfrac{1}{\rho(s)}\delta - \left(\tfrac{1}{\rho^2(s)} + k_x(s)\right) x + \mathcal{O}(2) \\ y' &= \tfrac{p_y}{1+\delta} + \mathcal{O}(2) \\ p'_y &= k_y(s) y + \mathcal{O}(2) \end{aligned} \tag{2.29}$$

where a vertical radius of curvature has been assumed to be negligible small. A linear transfer map can be constructed by the integration of these equations. The transfer maps represent a linear coordinate transformation. With the assumption of a stepwise constant Hamiltonian, a matrix representation M of each element in the accelerator can be found. One property of transfer matrices is of great importance: symplecticity. Symplectic matrices perform according to the Hamiltonian. This means that they are energy conserving and fulfill

$$MSM^T = S \tag{2.30}$$

where

$$S = \begin{bmatrix} 0 & 1 & 0 & 0 \\ -1 & 0 & 0 & 0 \\ 0 & 0 & 0 & 1 \\ 0 & 0 & -1 & 0 \end{bmatrix}. \tag{2.31}$$

The matrix S is the symplectic unit matrix and a reflection of the structure of the Hamilton's equations.

The concatenation of transfer matrices is performed by the usual matrix multiplication

$$M_{1\to3} = M_{2\to3}M_{1\to2}. \tag{2.32}$$

The concatenation of all matrix representations creates the one-turn map. Some of the global properties like the tunes can be derived from the one-turn map.

The 4×4 matrices based on equation 2.29 act on the four-dimensional phase space with the coordinates $\vec{x} = (x,\, p_x,\, y,\, p_y)^T$. They are sufficient to describe pure transverse motion. The inclusion of longitudinal motion leads to the necessity to increase the dimensionality to 6×6. The 6×6 transfer matrices act on a six-dimensional phase space and a matrix representation of physical elements can be found e.g. in chapter 5 of ref. [10].

2.1.7 Dispersion and Chromaticity

The deflection of a particle beam using a dipole magnet is dependent on the momentum. This means that the deflection angle of a dipole magnet is different for each particle in a non-monochromatic[4] beam. The perturbation is given by $\frac{\delta}{\rho}$ where the momentum deviation should be small ($\delta \ll 1$). The linear parts of the transverse equation of motion reads

$$u'' + K(s)u = \frac{\delta}{\rho(s)}. \tag{2.33}$$

Particles with a momentum deviation move along dispersion trajectories $x_D = D_x^{(1)}\delta$ where $D_u^{(1)}(s)$ denotes the periodical horizontal[5] linear dispersion function:

$$D_u^{(1)}(s) = \frac{\sqrt{\beta_x(s)}}{2\sin(\pi Q_x)} \oint \frac{\sqrt{\beta_x(\tilde{s})}}{\rho(\tilde{s})} \cos\left(\psi_x(\tilde{s}) - \psi_x(s) - \pi Q_x\right) d\tilde{s}. \tag{2.34}$$

Also the focusing strength of quadrupole magnets is dependent on the momentum of particles. This momentum dependency leads to changes of the phase advances and in second consequence of the tunes. This effect is the so called natural chromaticity ξ_0 which is given by

$$\xi_{u,0} = \frac{\partial Q_u}{\partial \delta} = -\frac{1}{4\pi} \oint k_u(s)\beta_u(s)ds. \tag{2.35}$$

The momentum spread of the circulating beam introduces a tune spread. This should be prevented since a tune spread can lead to particle loss e.g. due to overlap of resonance or to instabilities like the head-tail instability [11]. The most efficient way to correct chromaticity is the usage of sextupole magnets [12]. Ideally they are placed close to quadrupole magnets where the chromatic effects occur. Localized correction is not always possible e.g. due to space restrictions or economical reasons.

[4] monochromatic: all particles have the same momentum

[5] The vertical dispersion is negligible small in planar accelerator rings

A global chromaticity correction can be achieved by the use of sextupole magnets at places with non-zero horizontal dispersion:

$$\begin{aligned}\frac{\partial Q_x}{\partial \delta} =& \frac{1}{4\pi} \oint \beta_x(s) r(s) D_x(s) ds \\ \frac{\partial Q_y}{\partial \delta} =& -\frac{1}{4\pi} \oint \beta_y(s) r(s) D_x(s) ds,\end{aligned} \tag{2.36}$$

where $r(s)$ is the sextupole gradient.

2.1.8 Momentum compaction and transition energy

The trajectory and its length L of a particle alters with the particles momentum due to dispersion. The momentum compaction factor α_c is a measure for the relative change of the trajectory length in dependence of the momentum deviation:

$$\alpha_c = \frac{\triangle L/L}{\delta} = \frac{1}{L} \oint \frac{D(s)}{\rho(s)} ds. \tag{2.37}$$

The time T which a particle needs for one turn

$$T = \frac{L}{\beta c} \tag{2.38}$$

is also changed

$$\frac{\triangle T}{T} = \frac{\triangle L}{L} - \frac{\triangle \beta}{\beta} = -\left(\frac{1}{\gamma^2} - \alpha_c\right) \delta \tag{2.39}$$

where $\frac{\triangle T}{T}$ denotes the relative change. This momentum dependence of the travelling time for one turn results in a spread Δf of the revolution frequency $f = \frac{1}{T} = \frac{\beta c}{C}$.

In order to accelerate particles, the phase of on-momentum particles and the accelerating RF signal has to be kept fixed. This boundary condition depends on the revolution frequency f_{RF} of the RF signal, the velocity of particles and is given by

$$f_{RF} = h \frac{\beta c}{C} \tag{2.40}$$

where h is the integer harmonic number which reflects the number of possible bunches in the accelerator. If particles are off-momentum, they oscillate in the longitudinal phase space around the reference phase. This oscillation is called synchrotron oscillation. The phase of the RF signal has to be chosen that off-momentum particles with longer travelling time through the accelerator ring are affected by a higher acceleration voltage compared to the on-momentum particles and vice versa. This is the so called phase focusing.

The derivative of the revolution frequency with respect to the momentum deviation crosses zero for a certain beam energy which is called transition energy E_{tr}. This non-physical energy in independent of the particle mass but depends only on the ion-optics of the accelerator and its geometry. At transition energy, the phase focusing vanishes leading to an increase of the momentum deviation of particles.

If the momentum deviation becomes larger than the momentum acceptance of the accelerator, particle loss is inevitable.

The ratio of the transition energy and the particles energy at rest is called

$$\gamma_{tr} = \frac{E_{tr}}{E_{rest}} = \frac{1}{\sqrt{\alpha_c}}. \tag{2.41}$$

Its value is close to the horizontal tune in case of a regular lattice. The frequency spread of the beam is related to its momentum spread via the so called frequency slip factor

$$\eta = \frac{1}{f_0}\frac{df}{d\delta} = \frac{1}{\gamma^2} - \frac{1}{C}\frac{dC}{d\delta} = \frac{1}{\gamma^2} - \frac{1}{\gamma_{tr}^2}. \tag{2.42}$$

2.1.9 Orbit response matrix

Besides dispersion, other effects like alignment errors or multipole field errors of magnets affect the trajectories of particles resulting in deviations from the reference trajectory. Even then, particles oscillate around a distorted orbit which refers to the reference particle. This trajectory of the reference particle is still closed and is therefore called *closed orbit*.

The method of orbit response matrix [13] can be utilized to correct the closed orbit. The matrix entries R_{di} reflect changes of an orbit deviation Δu_d at beam position monitors [14] at location d due to changes in deflection strength $\Delta\theta_i'$ of orbit correction dipole magnets located at position i and are given by

$$R_{di} = \frac{\Delta u_d}{\Delta\theta_i'} = \sqrt{\beta_{u,i}\beta_{u,d}}\frac{\cos\left(\pi Q_u - \Delta\psi_{u,di}\right)}{2\sin\left(\pi Q_u\right)} \tag{2.43}$$

where $\Delta\psi_{u,di}$ denotes the phase advance between both locations d and i. For locations with a non-zero dispersion, a correction term $+\frac{D_{u,d}D_{u,i}}{\left(\frac{1}{\gamma^2}-\alpha_c\right)C}$ can be added to the right hand side of equation 2.43 where D_u denotes the dispersion function, α_c the momentum compaction factor and C the circumference of the accelerator.

The orbit response matrix depends on the transverse tune Q_u, on the beta function β_u at beam position monitors and correction dipole magnets and on the phase differences $\Delta\psi_u$ of their locations. This means that the orbit response matrix can even be calculated from a computer model which mathematically describes the particle accelerator under investigation [15].

The orbit response matrix can be used in an iterative process to successively optimize the closed orbit. Its application can be performed in two possible ways:

It can be used as it is in an feed-forward process

$$\vec{S} = R \cdot \vec{\Theta} \tag{2.44}$$

where $\vec{S}$ is a vector containing all orbit deviations at beam position monitors and $\vec{\Theta}$ a vector with deflection strengths of orbit correction dipole magnets respectively. The best correction can be achieved by variation of $\vec{\Theta}$ to reproduce the measured orbit deviations at the beam position monitors, e.g. with a χ^2 minimization. Then, the vector $-\vec{\Theta}$ contains the proper settings of all orbit correction dipole magnets

to correct the closed orbit deviations. The orbit response matrix can include errors due to measurement errors or due to deviations of the computer model and the real accelerator which explains why an iterative process is recommended. A thorough investigation concerning the comparison of both orbit response matrices (measured and calculated) can lead to an improvement of the accelerator model. The other possibility to apply the orbit response matrix is via its inversion

$$\vec{\Theta} = R^{-1}\vec{S}. \tag{2.45}$$

Each methods has its advantages and disadvantages. While the feed-forward method is always applicable, the inversion of R is not. If R is not square or is degenerated, a pseudo-inverse has to be constructed e.g. using SVD[6]. On the other hand side, the inversion has to be calculated once only and matrix vector multiplications should be much faster than variation methods, especially if convergence of the iterative process is slow.

2.1.10 Influence of electron coolers toroid magnets on closed orbit

A stored beam of ions can be cooled using beam cooling techniques like electron cooling. In order to cool the ion beam, a nearly monochromatic and parallel electron beam is caused to overlap with the circulating ion beam. The velocity of electrons has to adjusted to be equal to the average velocity of the ions in the circulating beam. If the observation is moved to a frame which moves with the electron velocity, the latter will be at rest forming some kind of grid. The ions in the circulating beam will pass through the electron beam from all directions and with a variety of velocities. The ions will be affected by Coulomb scattering at the resting electrons while loosing energy which is transferred to the electrons. The loss of energy corresponds to transverse and longitudinal cooling at the rest frame. Ideally, all ions in the circulating beam have the same velocity and no transverse momentum after the electrons are removed. Since the electrons are constantly renewed, the ions are cooled during each passing through the electron cooler.

An electron cooler itself usually consists of an electron gun and a collector (see Figure 2.3) as well as of beam transportation devices. The interaction region where electrons and ions are overlapping is located inside a solenoid magnet which has a longitudinal magnetic field. At both end of the interaction region, there are toroid magnets used to guide the electron beam in and out of the circulating ion beam. Toroid magnets are basically bent solenoid magnets with an additional dipole field to compensation centrifugal force and do not only affect the electron beam but also the circulating ion beam. The effect is differently strong for both transverse directions.

In the following, it is assumed that the toroidal bending is vertical. The equation for the vertical deflection of the circulating beam can be derived from simple geometry [16]:

$$x' = -\frac{B_0 R_e}{B\rho} \ln\cos\left(\varphi_{Toroid}\right) \tag{2.46}$$

[6]Singular Value Decomposition

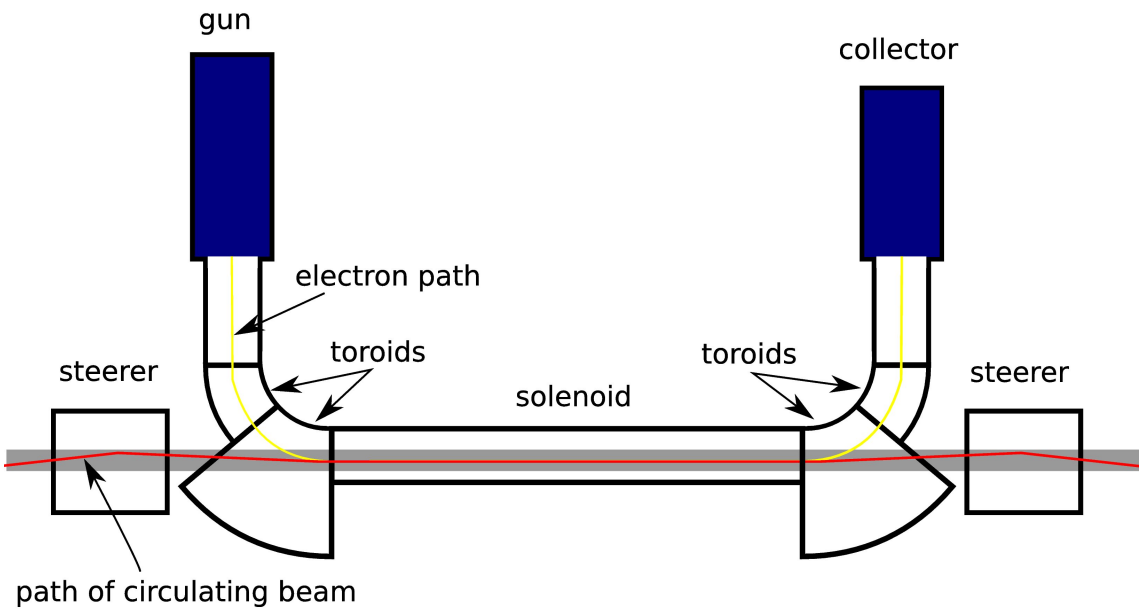

Figure 2.3: Schematic view of an electron cooler. The circulating beam (red) travels from left to right. The electrons of the electron beam (yellow) are generated in the electron gun and accelerated. The electron beam travels through both toroid magnets below the electron gun and the interaction straight inside the solenoid magnet. Behind it, the electron beam is bend upwards by the second two toroids, decelerated and dumped in the electron collector. In the lower two toroid magnets, both beam are merged and after the cooling section separated again. These toroid magnet are larger dimensioned to include the vacuum chamber of the circulating beam (gray). Next to the electron cooler, there are correction dipole magnets (steerer) to correct the deflections of the circulating beam caused by the lower toroid magnets.

where B_0 denotes the toroidal magnetic field strength at the reference radius R_e of the electrons and φ_{Toroid} is the bending angle of the toroid magnet itself. The magnetic rigidity of the circulating ion beam is given by $B\rho$. In addition to the magnetic field of the toroid magnet, the dipole field contributes to the horizontal deflection adding up to

$$y' = \frac{\int B_\perp ds + \int B_{dip} ds}{B\rho} \quad \text{where} \tag{2.47}$$

$$\int B_\perp ds = -\int_0^{\varphi_{Toroid}} \frac{B_0^2 R^2}{B\rho} \ln\left(\cos\left(\varphi\right)\right) d\varphi \quad \text{and} \tag{2.48}$$

$$B_{dip} = \frac{\sqrt{T_e\left(2E_e + T_e\right)}}{qcR} \tag{2.49}$$

where $E_e = m_e c^2$ denotes the electrons energy at rest and T_e their kinetic energy. Whereas the horizontal deflection angle x' scales linearly with the beam momentum via the magnetic rigidity $B\rho = \frac{cp}{q}$, the vertical one does not. The vertical deflection angle y' scale differently since the integral $\int B_\perp ds$ depends on the magnetic rigidity itself.

2.2 Non-linear beam dynamics

The stability of the particle beam of major concern. Particle motion can become non-linear e.g. in presence of higher-order multipoles like the necessary sextupoles or field errors. These non-linearities make the beam behavior unpredictable and lead to the necessity of particle tracking. Furthermore the higher-order multipoles can drive resonances which restrict the area of stable motion in phase space. Generally, dynamic aperture calculations are used to find the stable area in multi-dimensional phase space.

2.2.1 Symplectic Maps

A more generalized form of transport matrices are symplectic transfer maps which are per definition symplectic and not necessarily linear.

The Poisson bracket which is defined by

$$[f(\vec{x}),\, g(\vec{x})] \equiv \sum_{i=1}^{n} \left[\frac{\partial f(\vec{x})}{\partial x_i} \frac{\partial g(\vec{x})}{\partial p_i} - \frac{\partial f(\vec{x})}{\partial p_i} \frac{\partial g(\vec{x})}{\partial x_i} \right]. \tag{2.50}$$

can be used to express the total time derivative for any function $f(\vec{x}; s)$ of the phase space variables $\vec{x} = [x,\, p_x,\, y,\, p_y,\, \delta,\, ct]^T$ as

$$\frac{df(\vec{x})}{ds} = -\,[\mathcal{H},\, f(\vec{x}; s)] + \frac{\partial f(\vec{x}; s)}{\partial s} \tag{2.51}$$

where time was replaced by s and $\mathcal{H}$ denotes the Hamiltonian. The total time derivative is reduced to the Poisson bracket solely

$$\frac{df(\vec{x})}{ds} = -\,[\mathcal{H},\, f(\vec{x}; s)] \tag{2.52}$$

if the function $f(\vec{x}; s)$ is not explicit dependent on s. One important feature of the Poisson bracket is the invariance under canonical transformations (e.g. to action-angle variables $[J, \phi]$). Furthermore it has the three properties which define a Lie algebra [17]: It is antisymmetric and distributive and also fulfills Jacobi's identity. Thus it can be written in Lie operator form

$$: f(\vec{x}) : g(\vec{x}) \equiv [f(\vec{x}),\, g(\vec{x})] \tag{2.53}$$

which changes equation 2.52 to

$$\frac{df(\vec{x})}{ds} = -\,: H : f(\vec{x}). \tag{2.54}$$

It can be shown that two Lie operators are equal if the underlaying functions only differ by an arbitrary constant. Thus the Lie operators also form a Lie algebra.

A map representation of a Hamiltonian which acts on functions (of phase space coordinates) and commutes at different times can be expressed in the following form:

$$\mathcal{M}_{\vec{\xi}_{0\to 1}} = \exp\left(: -\int_{s_0}^{s_1} \mathcal{H}(s) ds : \right). \tag{2.55}$$

This is valid due to the Hamiltonian being the generator of an infinitesimal coordinate transformation. The corresponding transfer map $\vec{\xi}$ acting on phase space coordinates is given by

$$\vec{x}_1 = \vec{\xi}_{0\to1}(\vec{x}_0) \tag{2.56}$$

Under the assumption of a stepwise constant Hamiltonian, a functional map of an element with length L reads

$$\mathcal{M}_{\vec{\xi}_{0\to1}} = \exp\left(: -L\mathcal{H} :\right). \tag{2.57}$$

Concatenation of functional transfer maps is done in reverse order compared to concatenation of transfer matrices:

$$\mathcal{M}_{\vec{\xi}_{0\to1}}\mathcal{M}_{\vec{\xi}_{1\to2}} \equiv \mathcal{M}_{\vec{\xi}_{0\to2}}. \tag{2.58}$$

Non-linearities are introduced by thin non-linear kicks applied on phase space variables and are connected by linear maps. A one-turn functional map looks then like

$$\mathcal{M}_{\vec{\xi}_{0\to n}} = \mathcal{M}_{\vec{\xi}_{0\to1}} e^{:V_1:}\mathcal{M}_{\vec{\xi}_{1\to2}} e^{:V_2:}\mathcal{M}_{\vec{\xi}_{2\to3}} \ldots\ e^{:V_{n-1}:}\mathcal{M}_{\vec{\xi}_{n-1\to n}} \tag{2.59}$$

where V_i represent a thin non-linear kicks at position i and n is the number of elements in the accelerator. With the introduction of

$$\hat{V}_i \equiv \mathcal{A}_0\mathcal{M}_{\vec{\xi}_{0\to i}} V_i = \mathcal{R}_{0\to i} V_i, \tag{2.60}$$

all thin kicks can be shifted to the beginning of the lattice. The operator $\mathcal{R}$ is the rotation operator. The one-turn map reads then

$$\mathcal{M}_{\vec{\xi}_{0\to n}} = \mathcal{A}_0^{-1} e^{:\hat{V}_1:} e^{:\hat{V}_2:} \ldots e^{:\hat{V}_{n-1}:}\mathcal{R}_{0\to n}\mathcal{A}_n \tag{2.61}$$

After that, all thin kicks can be lumped into a single kick by the Baker-Campbell-Hausdorff (BCH) theorem for non-commuting operators

$$e^a e^b = e^{a+b+[a,\,b]/2+\ldots} \tag{2.62}$$

and the one-turn map finally looks like

$$\begin{aligned}\mathcal{M}_{\vec{\xi}_{0\to n}} &= \mathcal{A}_0^{-1} e^{:h:}\mathcal{R}_{0\to n}\mathcal{A}_n \\ &= \mathcal{A}_0^{-1} \exp\left(: \sum_{i=1}^{N} \hat{V}_i + \frac{1}{2}\sum_{i<j}^{N}\left[\hat{V}_i,\, \hat{V}_j\right] + \ldots :\right)\mathcal{R}_{0\to n}\mathcal{A}_n\end{aligned} \tag{2.63}$$

2.2.2 Driving terms

The driving terms represent the contribution of multipoles to specific effects, e.g. betatron resonances. Exemplary, they will be derived for sextupole magnets in first order concerning their contribution to the sextupole betatron resonances.

The vector potential for a thin sextupole magnet is given by

$$V_i = \frac{q}{p_0} A_s\left(s_i\right) = -\frac{b_{2,i}}{3}\left(x^3 - 3xy^2\right) \tag{2.64}$$

where s_i is an arbitrary location. The thinness of sextupoles implies a step wise constant potential $A_s(s_i)$. With

$$\mathcal{A}_i x = \sqrt{\beta_{x,i}}x + D^{(1)}_{x,i}\delta \tag{2.65}$$

where $D^{(1)}_x$ represents the first-order horizontal dispersion, the transformation acts like

$$\begin{aligned} \tfrac{1}{3}\mathcal{A}_i(x^3 - 3xy^2) &= \tfrac{1}{3}\sqrt{\beta_{x,i}}\left(x + D^{(1)}_{x,i}\delta\right)^3 - \left(\sqrt{\beta_{x,i}}x + D^{(1)}_{x,i}\delta\right)\beta_{y,i}y^2 \\ &= \sqrt{\beta_{x,i}}\left(D^{(1)}_{x,i}\right)^2 x\delta^2 + \tfrac{1}{3}\beta^{3/2}_{x,i}x^3 - \sqrt{\beta_{x,i}}\beta_{y,i}xy^2 \\ &\quad + \left(\beta_{x,i}x^2 - \beta_{y,i}y^2\right)D^{(1)}_{x,i}\delta + \mathcal{O}(\delta^3). \end{aligned} \tag{2.66}$$

There are no terms with first-order vertical dispersion. The eigenvalues of the rotational operator $\mathcal{R}$ in terms of a resonance basis

$$h^{\pm}_x \equiv \sqrt{2J_x}e^{\pm i\phi_x} = x \mp ip_x \tag{2.67}$$

are

$$\mathcal{R}_{i\to j}h^{\pm}_x = \mathcal{R}_{i\to j}\sqrt{2J}e^{\pm i\phi_x} = \sqrt{2J}e^{\pm i(\phi_x + \psi_{i\to j,\,x})} = e^{\pm i\psi_{i\to j,\,x}}h^{\pm}_x \tag{2.68}$$

where $\psi_{i\to j}$ is the phase advance between locations i and j. Expressing x and y in terms of the resonance basis, applying the rotational operator, and sorting for orders in x and y delivers

$$\begin{aligned} \mathcal{R}_{0\to i}x &= \tfrac{1}{2}\left(h^+_x e^{i\psi_{xi}} + c.c.\right), \\ \mathcal{R}_{0\to i}x^2 &= \tfrac{1}{4}\left(h^{+2}_x e^{i2\psi_{xi}} + c.c. + 4J\right), \\ \mathcal{R}_{0\to i}x^3 &= \tfrac{1}{8}\left(h^{+3}_x e^{i3\psi_{xi}} + 3h^{+2}_x h^-_x e^{i\psi_{xi}} + c.c.\right), \\ \mathcal{R}_{0\to i}xy^2 &= \tfrac{1}{8}\left(h^+_x h^{+2}_y e^{i(\psi_{xi}+2\psi_{yi})} + h^+_x h^{-2}_x e^{i(\psi_{xi}-2\psi_{yi})}\right. \\ &\quad \left. + 2h^+_x h^+_y h^-_y e^{i\psi_{xi}} + c.c.\right). \end{aligned} \tag{2.69}$$

The Lie generator $:h:$ can be determined to have in first-order the following form

$$h^{(1)} \equiv \sum_{|\bar{I}|} h_{\bar{I}} h^{+i_1}_x h^{-i_2}_x h^{+i_3}_y h^{-i_4}_y \delta^{i_5} \tag{2.70}$$

where $\bar{I} = [i_1,\, i_2,\, i_3,\, i_4,\, i_5]$ and $\left|\bar{I}\right| \equiv i_1 + i_2 + i_3 + i_4 + i_5$. Stating this, the first-order driving terms can be extracted by comparison of equations 2.66 and 2.69 and collecting geometric[7] terms

$$\begin{aligned} h_{21000} &= h^*_{12000} &&= -\tfrac{1}{8}\textstyle\sum_{i=1}^{N}(b_{2,i}L)\beta^{3/2}_{x,i}e^{i\psi_{x,i}}, \\ h_{30000} &= h^*_{03000} &&= -\tfrac{1}{24}\textstyle\sum_{i=1}^{N}(b_{2,i}L)\beta^{3/2}_{x,i}e^{i3\psi_{x,i}}, \\ h_{10110} &= h^*_{01110} &&= \tfrac{1}{4}\textstyle\sum_{i=1}^{N}(b_{2,i}L)\beta^{1/2}_{x,i}\beta_{y,i}e^{i\psi_{x,i}}, \\ h_{10200} &= h^*_{01020} &&= \tfrac{1}{8}\textstyle\sum_{i=1}^{N}(b_{2,i}L)\beta^{1/2}_{x,i}\beta_{y,i}e^{i(\psi_{x,i}+2\psi_{y,i})}, \\ h_{10020} &= h^*_{01200} &&= \tfrac{1}{8}\textstyle\sum_{i=1}^{N}(b_{2,i}L)\beta^{1/2}_{x,i}\beta_{y,i}e^{i(\psi_{x,i}-2\psi_{y,i})}. \end{aligned} \tag{2.71}$$

[7] non-chromatic

The driving terms marked with an asterisk are the complex conjugates. Since driving terms are in general complex numbers, the contributions of the single sextupole magnets are as well. Thus the driving terms can be written as

$$h_{jklmq} = \sum_{i=1}^{N} A_{jklmq,i} e^{i\phi_{jklm,i}} \tag{2.72}$$

where $A_{jklmq,i}$ and $\phi_{jklm,i}$ represent the amplitude and the driving term phase at the locations of the sextupole magnets. The indices are related to their dependencies e.g. on the beta functions or betatron phases

$$\begin{aligned} A_{jklmq,i} &\propto \beta_{x,i}^{(j+k)/2} \beta_{y,i}^{(l+m)/2} \left(D_{x,i}^{(1)}\right)^q \\ \phi_{jklm,i} &\propto (j-k)\,\psi_{x,i} + (m-l)\,\psi_{y,i}. \end{aligned} \tag{2.73}$$

Driving terms with $q > 0$ are chromatic ones. To give one example: The driving terms h_{11001} and h_{00111} depend linearly on dispersion and beta functions, but not on the betatron phases. Both driving terms are related to chromaticity and reflect equations 2.36. Driving terms are geometric for $q = 0$. Those have pure oscillatory character and drive betatron resonances. The frequencies of the resonances are determine by the other four indices by

$$(j-k) \cdot Q_x + (l-m) \cdot Q_y \tag{2.74}$$

Stating this, the driving terms in equation 2.71 contribute to betatron resonances with the frequencies:

$$Q_x,\ 3Q_x,\ Q_x,\ Q_x + 2Q_y,\ Q_x - 2Q_y. \tag{2.75}$$

All of these driving terms are first-order driving terms only. According to BCH theorem and the corresponding expansion of the symplectic map in equation 2.63, two sextupolar potentials and thus driving terms contribute in second order to octupole resonances and so forth.

2.2.3 Tracking code

Tracking codes are utilized to simulate particle trajectories. They are based on transfer maps either linear or non-linear. The maps have to be symplectic in order to track particles realistic without unphysical energy loss or gain. They represent a physical element or if concatenated even whole sections of an accelerator. Such a transfer map performs a coordinate transformation and lets a particle or a bunch of particles "travel" through an accelerator. The so called one-turn map is the concatenation of all transfer maps and a representation of the whole accelerator. Between coordinate transformations certain actions can be performed e.g. calculation of space charge forces[8] [18] or application of non-linear kicks.

The tracking code which has been used for this thesis is named SIMBAD [19] which is based on ORBIT [20].

[8]Force of charged particles acting on other charged particles within the beam or bunch

SIMBAD SIMBAD[9] is a symplectic tracking code which is based on linear maps. It is able to read transfer matrices produced by the linear modelling code MAD[10] version 8 [21] or X [22]. SIMBAD tracks six-dimensional phase space coordinates using these matrices. In order to include non-linearities, between coordinate transformations non-linear kicks are included. These non-linear kicks represent field errors and sextupole magnets. Furthermore phase space coordinates can be dumped to an output file. Those turn by turn data can be analyzed afterwards (e.g. with frequency map analysis). SIMBAD is written in C++ with a modular structure. Therefore it is rather easy to extend. To speed up computation SIMBAD uses the message passing interface (MPI) environment to run on multiple cores, processors and/or computers.

2.2.4 Dynamic aperture

The dynamic aperture is commonly referred as the transition border from regular, stable motion to irregular, unstable or chaotic motion. Symplectic tracking codes are used to find the trajectories of particles over a certain number of turns. The dynamic aperture is mostly defined as the border of multi-dimensional phase space area of the starting coordinates of particles which survive a predefined number of turns [23]. The number of turns which particles have to survive is a question of time scale. For the so called short-term dynamic aperture, it is sufficient to track several hundreds up to a few thousands of turns to see betatron resonances [24] arising. Betatron resonances are commonly referred by the condition

$$m \cdot Q_x + n \cdot Q_y = p \tag{2.76}$$

where m, n, and p have to be integer and the resonance order is often referred as $|m|+|n|$. Resonances with n being even are commonly referred as normal whereas with n being odd as skew resonances. The density of resonances in the tune diagram can be reduced by the introduction of symmetry to the accelerator lattice [25] which means resonances can be suppressed. For an accelerator lattice with M equal periods, the integer p in the resonance condition can be replaced by $p = M \cdot r$ where r has to be integer. The long-term dynamic aperture is typically in the order of 10^9 turns to proof long-term stability. The long-term dynamic aperture has according to the Nekhoroshev theorem an inverse logarithmic dependence on the number of turns ([26, 27]).

For all dynamic aperture calculations, computation time is the major restriction. Starting particles in a dense six-dimensional phasespace over several million turns can easily take weeks, months or even years. Thus, a proper choice of starting coordinates is inevitable. There is a trade-off between accuracy (number of particles, density of phase space coordinates), number of turns, and computation time.

There are other approaches which help to find limiting resonances: Analysis of resonance driving terms or frequency map analysis.

[9] Symplectic tracking code from BNL
[10] Methodical Accelerator Design

2.2.5 KAM theorem

The KAM theorem goes back to the work of **K**olmogorov, **A**rnold, and **M**oser [28]. The KAM theorem states for a system which can be described by a Hamiltonian $\mathcal{H}$ with an integrable part $\mathcal{H}_0$ and a small perturbation $\varepsilon\mathcal{H}_1$ that the motion is regular and confined to so called KAM tori if three conditions are fulfilled [29]:

1. Linear independence of frequencies $\omega_i = \frac{\partial \mathcal{H}}{\partial J_i}$
2. Smoothness condition of the perturbation [30]
3. Sufficient distance of initial condition to a resonance

The KAM tori can be observed in phase space as circles if the scales of the axes are properly chosen and the motion is regular. If a perturbation is present and small enough to fulfill the three conditions, the KAM tori will be deformed. Such a deformation can be e.g. triangular for sextupolar perturbations.

In a phase space plot of a disturbed motion, three regions can be identified. The inner region of stable motion is filled with KAM tori. Islands which represent fixpoints of the motion can appear in this stable region between the KAM tori. Inside those thin chaotic layers, conditions three is violated. Further outside, there is a transition to the second region of chaotic motion. In this regions the second and the third condition is violated and no KAM tori can be observed. Island can appear at fixpoints. The last transition to the region of unbound motion is reached if condition one is not fulfilled anymore.

There are in principle two kinds of fixpoints: elliptic and hyperbolic ones. Elliptic fixpoints are stable and particles are able to reach them forming islands potentially surrounded by KAM tori. The hyperbolic fixpoints are unstable forming empty spots.

2.2.6 Frequency map analysis

Although the frequency map analysis was developed for celestial mechanics, it is now widely used for studies from atomic physics [31] to galactical dynamics [32] and nowadays even in accelerator physics [25]. This technique is based on a revised Fourier analysis which constructs the so-called frequency map from the space on initial conditions to the tune space. To do this, the NAFF algorithm [33] or variants of it like SUSSIX [34] searches for quasiperiodic approximation of the transverse motion over a finite time span or turns T. Starting a particle with two initial conditions ($x'_0 = y'_0 = 0$), the discrete trajectory is recorded in a four-dimensional surface of section $x(t)$, $x'(t)$, $y(t)$, $y'(t)$. Applying the refined Fourier technique, the quasiperiodic approximation, truncated to order N, of the form $z_w(t) = w(t)+iw'(t)$ reads

$$z_u(t) = a_u e^{iQ_u t} + \sum_{k=1}^{N} a_{\vec{m}_k} e^{i<\vec{m}_k,\vec{Q}>t},$$

where $\vec{Q} = (Q_x, Q_y, 1)$ is the fundamental frequency vector, $\vec{m}_k = (m_{1k}, m_{2k}, m_{3k})$ is a multi-index, $< \vec{m}_k, \vec{Q} >= m_{1k}Q_x + m_{2k}Q_y + m_{3k}$, and the complex amplitude $a_{\vec{m}_k}$ is ordered by decreasing magnitudes.

The frequency map F^T itself is defined as the mapping of starting coordinates to the transverse tunes

$$\begin{array}{rccc} F^T: & \mathbb{R}^2 & \rightarrow & \mathbb{R}^2 \\ & (x,\, y) & \mapsto & (Q_x,\, Q_y). \end{array} \tag{2.77}$$

The initial momenta can be neglected and thus arbitrarily chosen (e.g. $x'_0 = y'_0 = 0$) because the image of F^T is largely independent of them in the frequency plane [35]. The revised Fourier technique converges with $1/T^4$ [25] when applying an Hanning window [36] (FFT converges with $1/T$ [37]) . That reduces the number of necessary turns to typically 1000 which saves a lot of computation time.

If the approximation is a regular KAM solution, the frequency map F^T is invariant by time translations which means that the tunes are fixed over time. If this is not the case, the time variation of the tunes is related to the orbit diffusion[11] and hence can be used as a stability criterion. Thus the study of the regularity of the frequency map can provide information about resonances and non-linear behavior.

A stability criterion or a measure of stability related to the orbit diffusion is the so called diffusion coefficient D. The diffusion coefficient is defined as the root mean square of tune differences of two adjacent finite periods of time (e.g. 1000 turns)

$$D = \log_{10}\left[\sqrt{\left(Q_x^{(2)} - Q_x^{(1)}\right)^2 + \left(Q_y^{(2)} - Q_y^{(1)}\right)^2}\right] \tag{2.78}$$

where Q_x and Q_y are the transverse tunes calculated from (1) the first time period and (2) the second time period. A diffusion coefficient of $D \leq -7$ is considered to belong to stable motion whereas a diffusion coefficient of $D \geq -2$ is related to strongly chaotic and unbound motion [38].

[11] The general term is Arnold diffusion

Chapter 3

The High-Energy Storage Ring HESR

The High-Energy Storage Ring HESR is part of the upcoming Facility of Antiproton and Ion Research at the Helmholtzzentrum für Schwerionenforschung and dedicated to antiproton physics. It is a ring accelerator which is able to store, accelerate and provide antiprotons in a momentum range from 1.5 to 15 GeV/c for the internal target experiment PANDA [39, 4]. The HESR is designed by a consortium. Its members are Institut für Kernphysik at Forschungszentrum Jülich (Germany) as leading laboratory, GSI in Darmstadt (Germany), The Svedberg Laboratory in Upsala (Sweden), Soltan Institute for Nuclear Studies in Warsaw (Poland), CAD/CAM Engineering Center in Tbilisi (Georgia), National Institute for Research and Development in Electrical Engineering ICPE-CA in Bucharest (Romania), and IAP in Sumy (Ukraine).

3.1 Antiproton beams at FAIR

As the name states, a whole branch of the FAIR facility is dedicated to antiprotons from production over storage to experimental use. A central part of this branch is the HESR with its internal target experiment PANDA dedicated to antiproton physics.

3.1.1 HESR at FAIR

The Facility for Antiproton and Ion Research is an international project and will be a major extension of the present facility of the Helmholtzzentrum für Schwerionenforschung (GSI) in Darmstadt. It offers forefront science for European and international users in various fields which include radioactive ion beams, antiproton physics, compressed baryon matter, plasma physics, and atomic physics. The new facility itself consists of different experimental sites which enable unprecedented experimental possibilities. A schematic overview is shown in Fig. 3.1.

The international PANDA collaboration with a rich scientific program is working on a new experiment with antiprotons in the energy range between the AD and Tevatron regime. The HESR with its special equipment like multi harmonic

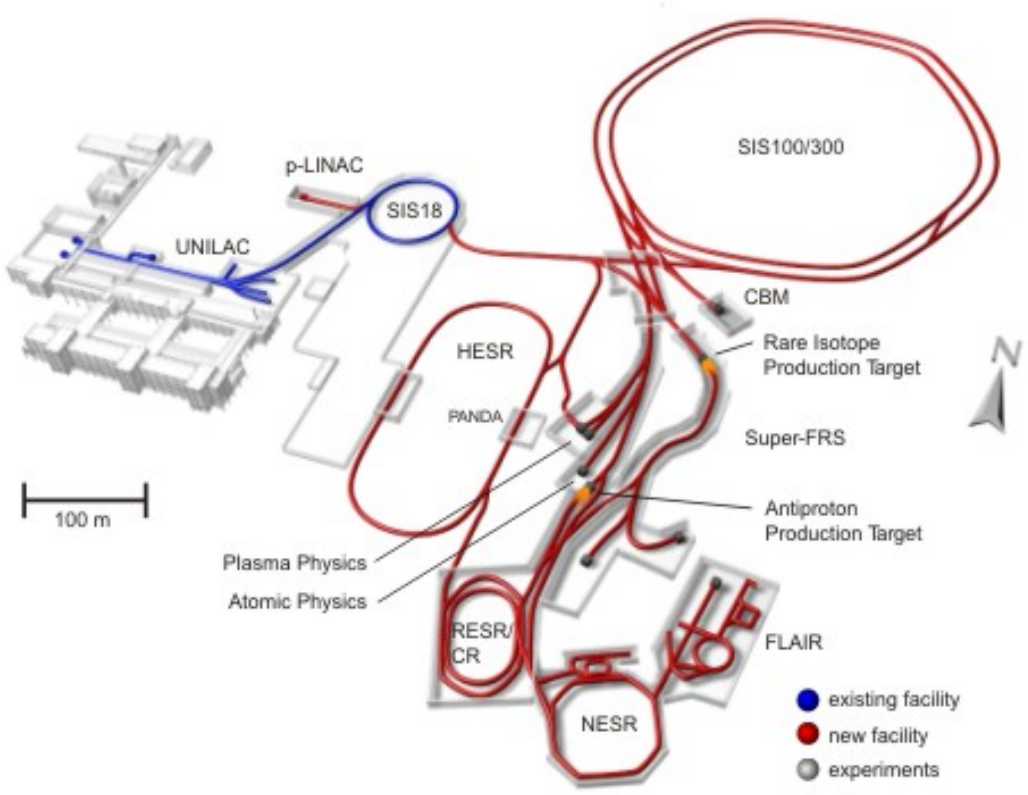

Figure 3.1: Schematic view of the FAIR site. The new accelerators are drawn in red, the present GSI accelerators in blue and experiments in gray. Important for the HESR are the following parts in the injection chain: p-LINAC, SIS18, SIS100, antiproton production target, CR, RESR. The HESR is aligned along an north-south axis. On the right hand side of the HESR, there is the PANDA experiment. The gray building on the left hand side of the HESR will house the electron cooler. The upper direct injection way from the SIS18 to the HESR is a possible upgrade which will allow the operation with protons moving in the opposite direction of antiprotons.

RF cavity [40], electron cooling[41] and stochastic cooling[42] make high precision experiments feasible which have not been possible before. Besides PANDA, other experimental groups namely PAX and ASSIA expressed their interest in using the HESR for spin physics related experiments [43, 44, 45]. Thus, sufficient space is reserved in the HESR design to allow an upgrade for polarized beams [46, 47].

3.1.2 Injection chain for antiprotons

A high-intensity proton beam of $35\,mA$ and pulse length of $36\,\mu s$ is accelerated in the new proton linac [48] to $70\,MeV$. The repetition rate is $4\,Hz$. The proton beam is then injected into the existing SIS18 [49]. Per cycle, roughly $2 \cdot 10^{12}$ protons are accelerated to $2\,GeV$ and then injected into SIS100 [50]. After a stack using eight injections from SIS18, up to $4 \cdot 10^{13}$ protons per cycle are accelerated to an energy of $29\,GeV$. Afterwards the bunches are compressed to $25\,ns$, ejected, and

shot on an antiproton production target [51]. The beam guiding system behind the antiproton production target is capable of transporting antiprotons with a beam energy of $3\,GeV$ and a maximum relative momentum spread of $\Delta p/p = 3\%$ which corresponds to approximately $2 \cdot 10^8$ antiprotons. The antiprotons are separated and guided to the collector ring CR [52] where the antiprotons are collected and cooled for $10\,s$ using a stochastic cooling system to reduce the beam emittance. After the beam cooling, the beam is rotated in the longitudinal phase space (bunch rotation) to achieve an even lower momentum spread. The cooled and rotated antiproton beam is then injected into the RESR [53] where it is further cooled using the RESR stochastic cooling system. The described injection chain can provide antiprotons with a production rate of $\dot{N}_{\bar{p}} = 2 \cdot 10^7\,s^{-1}$.

3.1.3 PANDA experiment

PANDA (Anti**P**roton **An**nihilation at **Da**rmstadt) is a universal detector and will be used to study interactions between antiprotons and fixed target protons and nuclei over the whole momentum range of the HESR. The target is planned to be a dense frozen H_2 pellet jet target. The scientific program of the PANDA collaboration includes several measurement which will address fundamental questions of QCD mostly in the non-perturbative regime [4].

The study of QCD bound states is fundamental importance. It will help to improve the quantitative understanding of QCD. Precision measurements are necessary in order to distinguish between different approaches. The PANDA measurements include charmonium, D meson and baryon spectroscopy. The non-perturbative QCD dynamics is going to be investigated. This will be carried out by the study of the creation mechanism of quark-antiquark pairs and their arrangement to hadrons. Also hadrons in nuclear matter are part of the PANDA physics program. The origin of hadron masses in the context of spontaneous chiral symmetry breaking in QCD is going to be studied by medium modifications of hadrons embedded in hadronic matter. Part of this investigation is also related to the partial restoration of the chiral symmetry in hadronic matter. Since earlier experiments related to this topic have been restricted to the light quark sector, PANDA is an extension to the charm sector for hadron with open and hidden charm. PANDA also competes with planned dedicated hypernuclei facilities. The availability of antiprotons beams at FAIR will allow an efficient way to produce hypernuclei with more than one strange hadron with opens new perspectives for nuclear structure spectroscopy. Also the study of forces between hyperons and nucleus is planned. The possibility of high-intensity antiproton beam in the HESR allows the production of large numbers of D-mesons which can be used to observe rare weak decays in order to study electroweak physics.

All measurements will profit firstly from the high yield of antiprotons induced reactions and secondly from the fact that all non-exotic quantum number combinations for directly formed states are allowed, whereas states with exotic quantum number can be observed in production. Significant progress beyond the present understanding of all topics is expected due to improvements in statistics and precision of the data.

3.2 HESR design

The HESR is designed as a storage ring with a racetrack shape and acceleration capabilities. Its magnetic rigidity ranges from 5 to 50 Tm which corresponds to the momentum range of 1.5 to 15 GeV/c. With its circumference of 575 m it covers an area of 120 m by 250 m.

3.2.1 Layout

The HESR layout is shown in Figure 3.2. Both arcs have a length of 155.5 m. They are designed to be symmetric and have a 180° bending. The straight sections have a length of roughly 132 m. Each straight section has a larger installation, namely the electron cooler and the PANDA experiment with target, and are therefore named after those.

Target straight section The target straight section will house the internal experiment PANDA with its target and other experimental installations. The design of the PANDA experimental setup requires the target to be embedded inside of a solenoid magnet. Another solenoid magnet will be installed in front of the target solenoid magnet to compensate for or at least minimize the effects of the target solenoid magnet on the antiproton beam (e.g. coupling). In order to separate secondary particles at small laboratory angles, a large aperture dipole magnet is part of the experimental installations of PANDA. This PANDA dipole magnet affects not only the charged particles created by reactions of the antiprotons with the hydrogen pellets of the target but also the circulating antiproton beam. Therefore, a chicane with two additional dipole magnets is necessary to compensate for the deflections of the PANDA dipole magnet. Furthermore parts of the stochastic cooling namely the pick-ups as well as the injection equipment and the accelerating RF cavities will be installed in the target straight section. There are two injection points planned. The first one will be used to inject protons and antiprotons from the RESR. The second injection from SIS18 which is planned as an upgrade allows protons to circulate in the opposite direction without changing the polarity of the magnets installed in the HESR.

Cooler straight section The electron cooler will be installed in the other straight section called the cooler straight section. At both ends of the electron cooler, compensation solenoid magnets are foreseen to compensate for the effects of the cooler solenoid magnet. Next to the compensation solenoid magnets, sufficient space is reserved for an upgrade of the electron cooler for a Siberian snake [47]. This upgrade consists of skew quadrupole magnets and additional solenoid magnets. For a full Siberian snake, a helix dipole magnet is needed in addition to the solenoidal fields. It is planned to be installed downstream of the electron cooler. An H^0 detector is part of the electron cooler setup and will be used to detect hydrogen atoms created by recombination of electrons and protons in the electron cooler. Since the count rate is a measure of the beam overlap, the H^0 detector will be used for commissioning and optimization of the electron cooler whenever proton beams are injected into

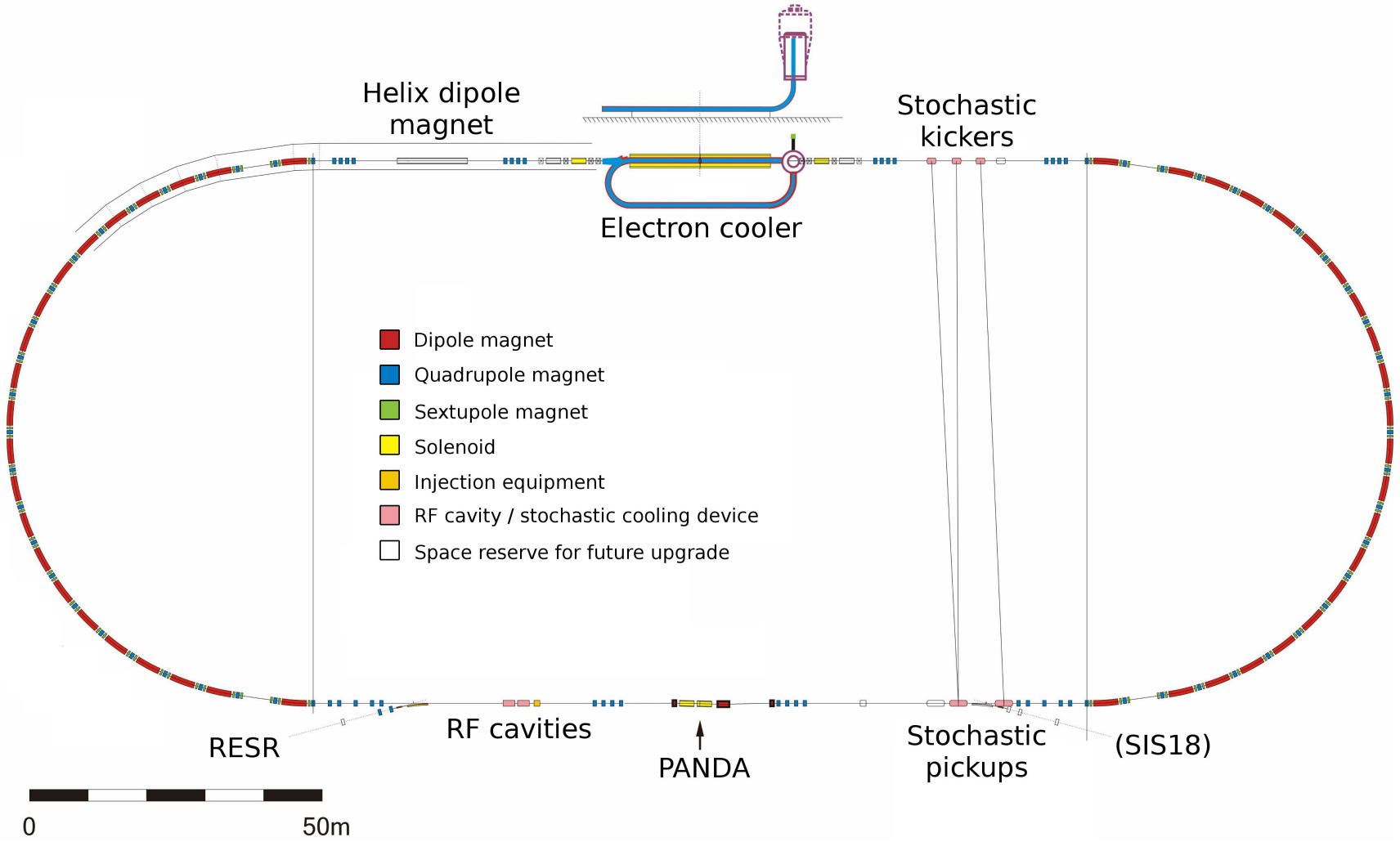

Figure 3.2: A schematic view of HESR lattice. The injection from the RESR is on the lower left and from SIS18 (upgrade) on the lower right. The lower straight houses the PANDA experiment with its three dipole magnets of the chicane, the target (arrow), the solenoid magnet around the target and the compensation solenoid magnet. Injection septa and kickers, the RF cavities left of PANDA, and the stochastic cooling pickups right of PANDA are also installed in this straight. The upper straight section houses the electron cooler. Compensation solenoid magnets as well as upgrade space reserve for a Siberian snake for polarized antiprotons is indicated left and right of the cooler. The helix dipole magnet is part of the cooler upgrade. The upper straight houses also the stochastic cooling kickers. The signal lines of the stochastic cooling system are drawn. At the upper left corner, the HESR tunnel is indicated.

the HESR instead of antiprotons. Without the injection branch from SIS18, protons have to move in the same direction as antiprotons. This implies a change of polarity of all magnets due to the different charge and the location of the H^0 detector being also downstream of the electron cooler from the view of antiprotons.

The stochastic kickers will be installed at the beginning of the cooler straight section.

Arcs The design of the arcs is based on regular FODO[1] structures. There are two demands which require a change to the FODO setup: The straight sections have to be dispersion-free and the transition energy has to be adjustable in the range from $\gamma_{tr} = 6.2$ to $\gamma_{tr} = 15$. While a regular FODO lattice uses two quadrupole magnet families (one horizontal and one vertical) to adjust the phase advance of the arcs, the revised design of the arcs include four quadrupole magnet families: Three horizontal and one vertical. One of the horizontal and the single vertical quadrupole magnet family is used to adjust the tunes of the arcs and of the HESR itself. The second horizontal quadrupole family is dedicated to the adjustment of the transition energy. The second last dipole magnets at each end of the arcs has been removed. This missing dipole magnet concept form together with the third horizontal quadrupole magnet family a dispersion suppressor for the straight sections. Since the dispersion in the straight sections has to be minimized, sextupole magnets for chromaticity correction must be placed in the arcs. Due to the necessary flexibility and the resulting design of the arcs, the places for sextupole magnets and orbit correction devices are limited to 48 per arc.

3.2.2 Magnets

The main magnet types [54] will be discussed in this subsection. All magnets of the HESR will be normal-conducting and thus iron-dominated.

Dipole magnet The HESR dipole magnet is a laminated room-temperature magnet. Its yoke has a length of $4.126\,m$ and a width of $1.142\,m$. The yoke cannot be straight but has to have a bending itself due to space restrictions of the HESR tunnel. Since the HESR design of the arcs requires 44 dipole magnets, each dipole magnet has to have a bending angle of 8.182° and a deflection radius of $29.432\,m$. This corresponds to a maximum magnetic field of $1.7\,T$ for a beam momentum of $15\,GeV/c$. The maximum magnetic field can be achieved by a current of approximately $2930\,A$. Since the necessary magnetic field scales linearly with the momentum, the lowest magnetic field is in the order of $0.17\,T$. However, the dipole magnets are designed and optimized for a nominal magnetic field of $1.0\,T$ which corresponds to a momentum of $8.9\,GeV/c$ since the main PANDA experiment will take place at this momentum.

[1] A regular structure where dipole magnets (O) are located between horizontally focusing (F) and defocusing (D) quadrupole magnets

Quadrupole magnet The design of the quadrupole magnets which are in total 84 in the HESR is based on the COSY one [55]. One important difference though is the yoke of the HESR quadrupole magnet which consists of four parts whereas the COSY quadrupole magnet has a two-part yoke. The length of the iron yoke is $0.58\,m$ whereas the effective length of the quadrupole magnet is $0.6\,m$. The other dimensions of the yoke are $1.06\,m$ in width and also in height. The aperture has a diameter of $100\,mm$ and is large enough to fit the vacuum chamber which has a diameter of $89\,mm$. The maximum gradient for operation has a design value of $20\,T/m$. This corresponds to a current of $426\,A$. Depending on acceleration strategy to overcome the transition energy, the gradient of $20\,T/m$ might not be sufficient. From the design of the HESR quadrupole magnet, a gradient of $25\,T/m$ is possible although not desired to be used regularly due to saturation effects. In order to reach a desired gradient of $25\,T/m$, a current of more than $700\,A$ has to be applied leading to a higher power consumption and the necessity of stronger water cooling of the quadrupole magnet.

Sextupole magnet The HESR lattice includes 52 places for sextupole magnets in the arcs which are going to be used for chromaticity correction (see section 5.2). Furthermore, there are four locations reserved within each straight section for possible installations of sextupole or higher-order multipole magnets which will be used for multipole compensation or resonance manipulation if that may be necessary.

The sextupole magnet has a two-part yoke. The yoke has a length of $0.3\,m$. Also the sextupole magnet design has equal dimension in width and height of $0.45\,m$. The diameter of the aperture is $140\,mm$. This is a 40% increase compated to the aperture of a quadrupole magnet. The purpose of the large aperture of the sextupole magnet is to house a beam position monitor which is caused besides others by the space restrictions in the arcs. With a current of $290\,A$, a sextupole magnet generates are gradient of $45\,T/m^2$. This corresponds to an overall integrated sextupole magnet strength of $0.25\,m^{-2}$.

Orbit correction dipole magnets The orbit correction dipole magnets are designed to deflect in one plane only. Because of the mounting, the design differs slightly for horizontally and for vertically deflecting orbit correction dipole magnets. Each of them are available as two types with different deflection strengths. The first type has a deflection strength of $1\,mrad$ at $15\,GeV/c$ for orbit correction purposes. The second type is designed for a maximum deflection of $2\,mrad$ at $15\,GeV/c$ where $1\,mrad$ is planned for orbit correction purposes and the second $1\,mrad$ for wanted displacements (closed orbit bumps) of the beam e.g. to bypass obstacles or to direct the beam onto the target. The increase of the deflection strength by a factor two is performed by doubling the windings per coil from 22 to 44. The maximum deflection strength corresponds to a current of roughly $304\,A$. The gap height is with $100\,mm$ equal to the diameter of the quadrupole magnets aperture.

3.2.3 Beam parameters

The quality of the antiproton beam delivered by the RESR is depending on the number of accumulated antiprotons. Both, the transverse beam emittance and the momentum spread grow with the number of antiprotons. The rms values are given by [3]

$$\begin{aligned} \epsilon_{x,y} &= \frac{1 mm\, mrad}{\beta\gamma} \left(\frac{N}{N_0}\right)^{4/5} \\ \frac{\sigma_p}{p} &= \frac{1.33 \cdot 10^{-3}}{\beta\gamma} \left(\frac{N}{N_0}\right)^{2/5}, \end{aligned}$$

where N denotes the number of injected antiprotons and $N_0 = 3.5 \cdot 10^{10}$ the reference number of antiprotons.

There are two defined modes of operation: A high luminosity mode and a high resolution mode. The high luminosity mode will deliver a luminosity of up to $2 \cdot 10^{32} cm^{-2} s^{-1}$ with 10^{11} antiprotons in the beam and a momentum spread of $\sigma_p/p \approx 10^{-4}$. To achieve this high luminosity, a pellet target of frozen hydrogen with an areal density of $4 \cdot 10^{15}$ atoms$/cm^2$ is planned to be used. The high momentum resolution of $\sigma_p/p \geq 4 \cdot 10^{-5}$ is only available with a reduced number of antiprotons in the order of 10^{10}. Its upper momentum limit is defined at $8.9\, GeV/c$ where the main PANDA experiment takes place.
To prevent an unbound beam blow up due to interactions with the target, beam cooling namely stochastic and electron cooling is used to cool into an equilibrium. This is especially important for the high resolution mode due to the strong demands concerning the momentum spread. Simulations of beam equilibria for both cooling methods have been performed [56, 57, 58]. The beam loss and beam luminosity are more important for the high luminosity mode. In order to estimate the luminosity, the HESR cycle has been determined [59]. The beam loss is dominated by hadronic interactions, Coulomb single scattering, and the energy loss caused by the scattering on the target.

The beam parameters at injection are listed in Table 3.1. The experimental requirements of PANDA for the antiproton beam as well the beam parameters at both operation modes can be found in Table 3.2.

Beam parameters at injection	
Transverse Emittance	$1\, mm\, mrad$ (norm., rms) at $3.5 \cdot 10^{10}\ \bar{p}$
Relative momentum spread	$1.33 \cdot 10^{-3}$(norm., rms) at $3.5 \cdot 10^{10}\ \bar{p}$
Bunch length	$200\, m$
Momentum	$3.8\, GeV/c$
Injection method	Within a single turn (kicker injection)

Table 3.1: Beam parameters of the injected antiproton beam

Experimental beam requirements by PANDA	
Kind of particles	antiprotons
Antiproton production rate	$2 \cdot 10^7\, s^{-1}$
Momentum range	1.5 to 15 GeV/c (0.83 to 14.1 GeV)
Number of antiprotons	$10^{10}$to 10^{11}
Areal target density	$4 \cdot 10^{15}$ atoms/cm^2
Beam size at target	$\approx 1\, mm$ (rms)

Beam parameters of mode	high luminosity	high resolution
Maximum luminosity	$2 \cdot 10^{32}\, cm^{-2}s^{-1}$	$2 \cdot 10^{31}\, cm^{-2}s^{-1}$
Momentum spread (rms)	$\sigma_p/p \geq 4 \cdot 10^{-5}$	$\sigma_p/p \approx 10^{-4}$
Momentrum range	1.5 to 15 GeV/c	1.5 to 8.9 GeV/c

Table 3.2: Beam parameter requirements of PANDA and both operation modes

3.2.4 Electron cooler

The electron cooler of the HESR[60, 3] is of special interest since this thesis covers the calculations of an closed orbit correction and compensation scheme concerning the deflections of the bending toroid magnets. The electron cooler of the HESR is capable to cool the antiproton beam in the momentum range from 1.5 to 8.9 GeV/c. This corresponds to an electron energy in the range from 400 keV to 4.5 MeV since the velocity of the electrons has to match the one of the antiprotons. The design of the HESR electron cooler includes the possibility for a later upgrade to a maximum electron energy of 8 MeV. This upgrade will allow electron cooling over the whole momentum range of the HESR.

The electron cooler will be used together with stochastic cooling to achieve the demanding requirements of the PANDA experiment. The circulating antiproton beam can e.g. be pre-cooled with the stochastic cooling system if that may be necessary.

The voltage of the electron cooler's acceleration column will be kept constant during one cycle. This has to be done in order to achieve the desired stability of the electron energy. This implies that the electron cooler can only be used at injection when this coincides with the experimental energy. The electron cooler has to compensate for heating effects of the the circulating antiproton beam introduced by the interaction with the internal PANDA target. Such a compensation can only be performed with magnetized cooling using a sufficiently strong longitudinal magnetic field [61, 62, 63]. The necessary magnetic field strength of the interaction straight has to be at least 0.2 T. This value was chosen to be the design value in order to allow a larger diameter of the electron beam in the interaction region. The resulting electron beam radius in the interaction straight of the electron cooler was determined to be in the order of 5 mm. The length of that interaction straight was chosen to be 24 m to match the requirements since the cooling rate is proportional to the product of the electron cooler length and the applied electron current. A maximum electron current of 1 A was chosen according to the recommendations in [61, 62, 63].

Avoiding to small beam spots, a controlled angular misalignment of the overlap of both beams can be applied.

A schematic view of the HESR electron cooler is shown in Figure 3.3. It presents the beam path of the electrons from the electron cooler's tank through the guiding system back to the tank again. The beam path includes the bends caused by the toroid magnets. The toroid magnets adjacent to the interaction straight affect not only the electrons but also the circulating antiproton beam. The design parameters of both relevant toroid magnets are equal although the toroid magnets are differently aligned (one horizontal and the other one vertical). In order to compensate for the deflection of the circulating antiproton beam, two orbit correction dipole magnets on each side of the electron cooler have to be included into the HESR design. There is only a compensation solenoid magnet in between of two correction dipole magnets on one side. Since the compensation solenoid magnet has only a longitudinal magnetic field and the beta functions have to be equal at the electron cooler, a solution for one toroid magnet can be applied for both sides since the necessary correction dipole magnets which are used for compensation have only to be tilted by 90°.

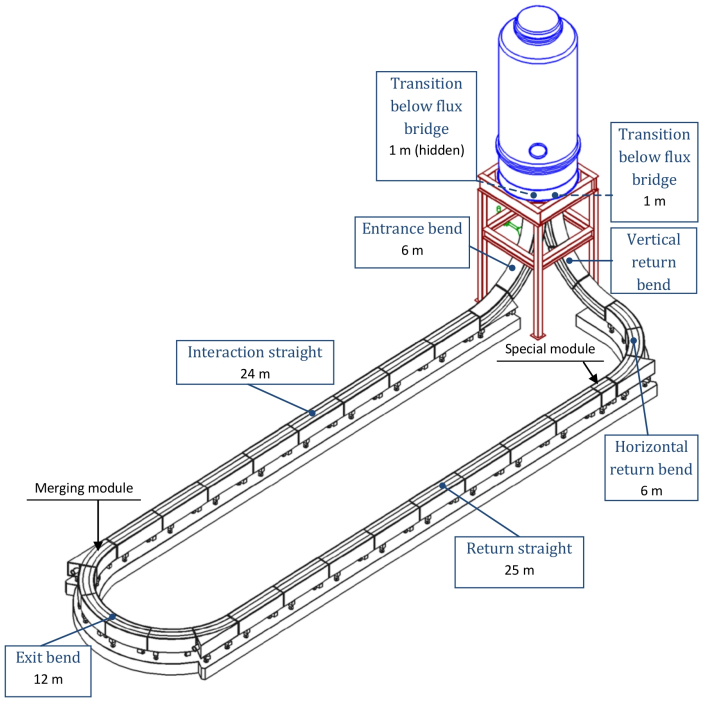

Figure 3.3: The layout of the HESR electron cooler consists of a high voltage terminal and a beam path surrounded by solenoid and toroid magnets. The tank atop houses besides the electron gun and the acceleration column also the collector and is extendable for the 8 MeV upgrade. The toroid magnets which are part of the electron guiding system can be seen a the end of the interaction and return straights. Below the tank, there is a vertical bend whereas a horizontal one is at the end of the interaction straight.

3.2.5 Ion-optical properties

Transition energy and defined ion-optical settings The transition energy of the HESR lattice can be adjusted in the range from $\gamma_{tr} = 6$ to $\gamma_{tr} = 15$. This flexibility is very important for the stochastic cooling system since the frequency slip factor η has to be sufficiently small to reduce unwanted mixing from the stochastic pickup to kicker [64]. Depending on the HESR operation, the transition energy may have to be be readjusted in order to match the requirements of the stochastic cooling system since the frequency slip factor changes with the beam energy. Therefore two essential ion-optical settings with $\gamma_{tr} = 6.2$ and $\gamma_{tr} = 13.3$ have been defined which will be used for specific ranges of the beam energy. The $\gamma_{tr} = 6.2$ setting will be used for beam energies above the injection energy of $3\,GeV$. This means that the $\gamma_{tr} = 6.2$ lattice will also be used for the main PANDA experiment at $8.9\,GeV/c$ and is therefore very important. The $\gamma_{tr} = 13.3$ setting is designed for low momenta of the antiproton beam. The ion-optical setting for injection is based on the $\gamma_{tr} = 6.2$ layout but with reduced beta functions around the target since no focusing at the target is needed during injection. The ion-optics for both lattice settings are shown in Figure 3.4.

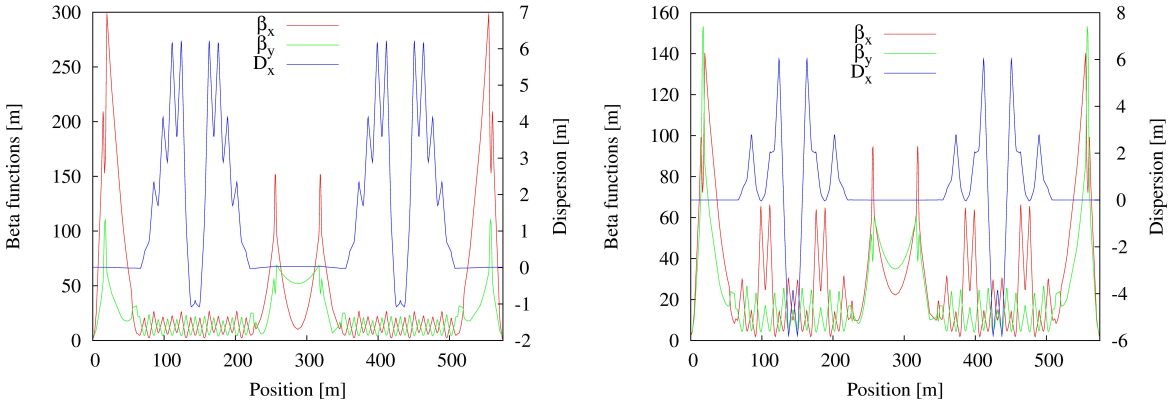

(a) The $\gamma_{tr} = 6.2$ lattice

(b) The $\gamma_{tr} = 13.3$ lattice

Figure 3.4: Ion-optics of the HESR for both lattices a) $\gamma_{tr} = 6.2$ and b) $\gamma_{tr} = 13.3$. The target is located at the origin. The center of the electron cooler is at $s \approx 288\,m$. Both plots show the modulation of the horizontal dispersion (blue) function to achieve dispersion-free straight sections. The beta functions (red and green) are much larger around the target than in the arcs which is caused by the focusing at the target. The comparison of both ion-optics reveals the differently large maximum beta functions around the target. Also the dispersion functions have different shapes.

Beta functions The beta functions can be adjusted at several points in the HESR: At the target, at the electron cooler, and at the stochastic cooling devices.

The beta functions at the target are adjustable in the range from 1 to $20\,m$. This is significant in order to match the beam to the target size. Due to the energy dependence of the geometric emittance, a change of the beam width has to be

compensated for by the adjustment of the beta functions resulting in a constant beam size of roughly $1\,mm$ (rms). The necessary focusing lead to an increase of the beta functions in the adjacent quadrupole triplets.

The beta functions at the electron cooler interaction region are adjustable in a range from 20 to $200\,m$. This is necessary to match the size of both beams because the transverse dimensions of the antiproton beam change significantly with the energy through adiabatic shrinking whereas the electron beam radius is fixed at $5\,mm$.

At the stochastic cooling devices, the beta functions can be varied to optimize the operation of the stochastic cooling system.

Natural chromaticity The natural chromaticity introduced by momentum dependence of the focusing of the quadrupole magnets ranges for the HESR from -10 to -15. It is $\xi_x = -14.82$ and $\xi_y = -10.31$ for the $\gamma_{tr} = 6.2$ lattice. For the $\gamma_{tr} = 13.3$ lattice, the natural chromaticity is with $\xi_x = -14.53$ horizontally slightly smaller whereas it is larger for the vertical one: $\xi_y = -11.13$.

A significant part of the chromaticity is created by the strong focusing and the large beta functions at quadrupole triplets close to the PANDA target.

3.3 Comparison with COSY

Alike the HESR, the Cooler Synchrotron COSY of the Forschungszentrum Jülich is a storage ring with similar cooling equipment: an electron cooler and a stochastic cooling system. COSY can store and accelerate polarized and unpolarized proton and deuteron beams in a momentum range from approximately 0.30 (0.54 for deuterons) up to $3.7\,GeV/c$ [65, 66]. An overview of the whole COSY facility with its internal and external experiments and preaccelerating cyclotron is show in Figure 3.5.

COSY has, similar to the HESR, a race track shape and consists of two symmetric arcs with a 180° bending and two straight sections. It has a circumference of $183.4\,m$ and is approximately a factor three shorter than the HESR. The straight sections have a length of $40\,m$ each. The ion-optics of the straights are adjustable to perform an identity mapping where the phase advance is then $\psi_{\mathrm{Straight}} = 2\pi$. Both arcs are mirror-symmetric and each of them is constructed out of three unit cells. Each unit cell itself consists of two mirror-symmetric halfcells using a FODO - DOFO arrangement.

Although the injection types of COSY and HESR differ (COSY has a stripping injection whereas the HESR is designed with a kicker injection), there are several similarities between both accelerators. The HESR as well as COSY feature e.g. the same beam cooling techniques and offer an electron cooler and a stochastic cooling system. Although the HESR will have only one internal experiment installed and COSY has several internal and also external experiments, there is one COSY experiments of special interest for the HESR development. This is the internal WASA experiment [70] which alike PANDA uses a pellet target. All of the similarities between both accelerators justify the usage of COSY as a benchmarking facility for the HESR. Thus, there are a lot of on-going experiments at COSY which cover hardware

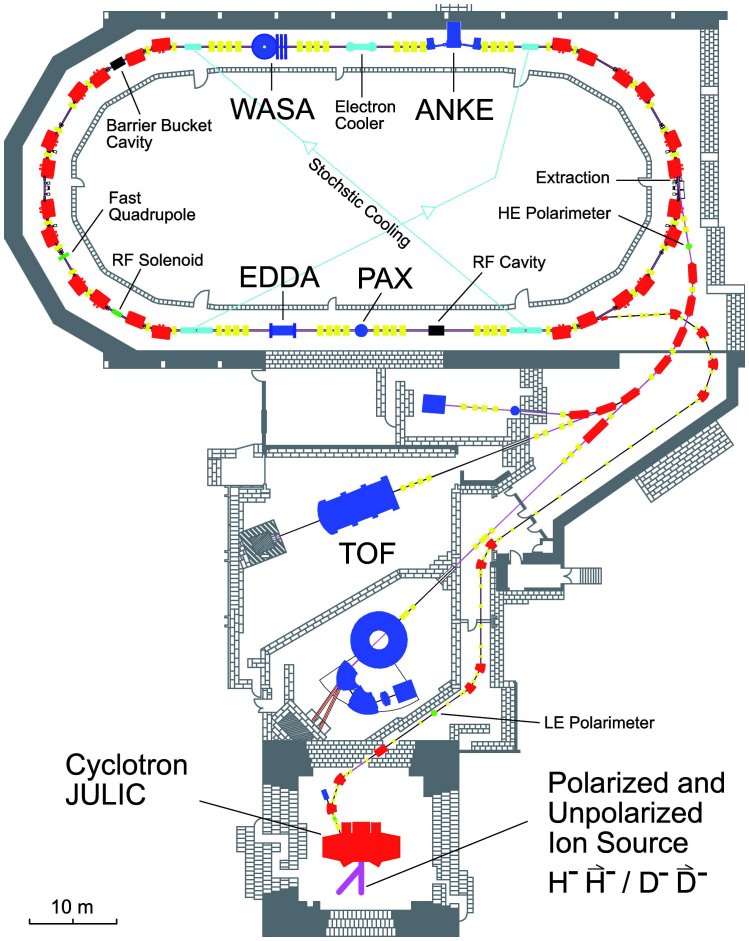

Figure 3.5: Schematic overview of cooler synchrotron COSY. The location of the ion sources for polarized and unpolarized beams are indicated. The cyclotron Julic is used for pre-acceleration. The electron cooler and the stochastic cooling devices of COSY are shown and the signal lines of the stochastic cooling system are indicated. The positions of the accelerating RF cavities and the barrier bucket cavity as well as fast quadrupole and RF solenoid magnet for polarization preservation and manipulation are designated. The locations of the internal experiments EDDA [67, 68], ANKE [69], WASA [70] including its pellet target and PAX [44] are marked. Injection, extraction and the external experiment TOF [71] are shown as well.

tests and proofs of experimental techniques which are relevant for HESR design and future operation.

New cavities have been designed and built to be used e.g. a barrier bucket cavity [40] in order to compensate for the mean energy loss induced by the internal pellet target. Cooling hardware has also been developed. The stochastic cooling system for the HESR will utilize hardware e.g. stochastic pickups with slot coupler [40] which have not been used at COSY before. Therefore prototypes have been built and tested at COSY. Besides new hardware, stochastic cooling techniques like the time-of-flight cooling have been successfully applied [64] and compared to notch-filter cooling. Furthermore, the combination of a barrier bucket cavity and stochastic cooling which is used to compensate for beam-target interactions was verified to be

effectively working. As a step toward the high energy electron cooler planned for the HESR, a $2\,MeV$ electron cooler is going to be built and installed into COSY to investigate the cooling forces and possibilities at high energies [72]. Also hardware related to beam diagnostics like a beam profile monitor was tested at COSY [73].

The proposed orbit response matrix method for closed orbit correction at HESR has been applied at COSY. Since COSY has a an electron cooler like the HESR, the local toroid magnet compensation bumps have to be taken into account for closed orbit corrections resulting in similar conditions as for the HESR. The orbit response matrix method could be validated as it is described in sction 4.2.

Chapter 4

Closed orbit correction

Alignment errors of accelerator components like magnets have been estimated and used to calculate closed orbit deviations. An orbit correction concept has been developed to allow efficient closed orbit corrections in the HESR. The for HESR proposed orbit response matrix method has been used to correct the closed orbit at COSY. Furthermore, the feasibility of local closed orbit bump at various locations has been checked.

4.1 Closed orbit correction system for HESR

4.1.1 Alignment errors

Magnets have to be aligned in three spatial and three rotational degrees of freedom. All deviations from the ideal alignment lead to orbit distortions. For simulation purposes the assumed Gaussian distribution of alignment errors can be truncated where $2.5\,\sigma$ is a reasonable value [74]. The utilization of a uniform distribution with proper values for the misalignment leads to similar orbit deviations [75] and thus was not checked again. Besides beam guiding magnets like dipole or quadrupole magnets, errors were applied to all other elements especially to beam position monitors and orbit correction dipole magnets. The applied alignment errors which are taken from COSY are shown in Table 4.1. The nomenclature corresponds to the MAD-X one. The angular errors have been calculated based on the spatial errors and the element dimensions.

The COSY accelerator is surrounded by concrete walls and roof, the so called COSY tunnel, inside the COSY hall. There are two central reference points in the center of COSY hall. These reference points are used to span an alignment grid inside the COSY tunnel. The latter has been used to align all magnets and elements of COSY. For the HESR this will be different. FAIR will have a primary alignment grid on the surface which will be transferred to local machines [77]. In opposite to COSY, the HESR is inside a tunnel which is surrounded by soil. Thus, there will be no central reference points as for COSY. Instead, there will be a certain number of reference points transferred from the primary to the local alignment grid inside the HESR tunnel. From these reference points, the local alignment grid for HESR is spanned. The necessary number of those transfers can be estimated by simulations

Magnet type	$ds\,[mm]$	$dx\,[mm]$	$dy\,[mm]$
Dipole magnet	1.0	0.2	0.2
Quadrupole magnet	0.2	0.5	0.2
Sextupole magnet	0.5	0.5	0.2
Correction dipole magnet	0.2	0.5	0.8

Table 4.1: Alignment errors of elements based on COSY alignment accuracy [76]. The alignment errors are given in the local co-moving coordinate system which means that ds is a shift along the beam axis whereas dx and dy are transverse misalignments.

but was not done so far. The individual elements and magnets will be aligned using a laser tracker system on the local alignment grid. The final, global accuracy is not known by now since simulations of tunnels, detailed lattices etc. have to be performed first.

4.1.2 Simulation of orbit distortions

The simulation of the orbit deviations has been performed using MAD-X. Since MAD-X is not capable to calculate twiss parameters and closed orbit with respect to field errors, the field errors of magnet have been neglected in the first step. Alignment errors have been applied to all elements according to Table 4.1. The pseudo-random number generator has been fed with a variety of different seeds resulting in different closed orbits. An example of ten orbits calculated with different seeds is shown in Figure 4.1. The biggest orbit deviations occur around the target and have a value of up to approximately $0.1\,m$. Elsewhere in the HESR, the maximum orbit deviations are with $< 0.04\,m$ a factor 2.5 smaller. This differences are caused by the very large beta functions of several $100\,m$ around the target. Nevertheless, the resulting uncorrected orbits are approximately one order of magnitude smaller than of the superconducting version of the HESR [75]. This can be traced back to the fact that the alignment of superconducting magnets inside cryostats is not as precise as of normal-conducting ones. Whereas normal-conducting magnets can be aligned in a direct way, superconducting ones have to be aligned first inside a cryostat which also has to be aligned itself.

4.1.3 Orbit correction elements

While the design of the orbit correction dipole magnets allows a deflection of the beam in one transverse direction only, the proposed beam position monitors can measure in both transverse directions.

Accuracy of beam position monitors and orbit correction dipole magnets
Besides the alignment errors, measurement errors [78] are applied to all beam position monitors according to Table 4.2. There are two different types of measurement errors. The first one is the relative scaling error and the second is the offset. For both

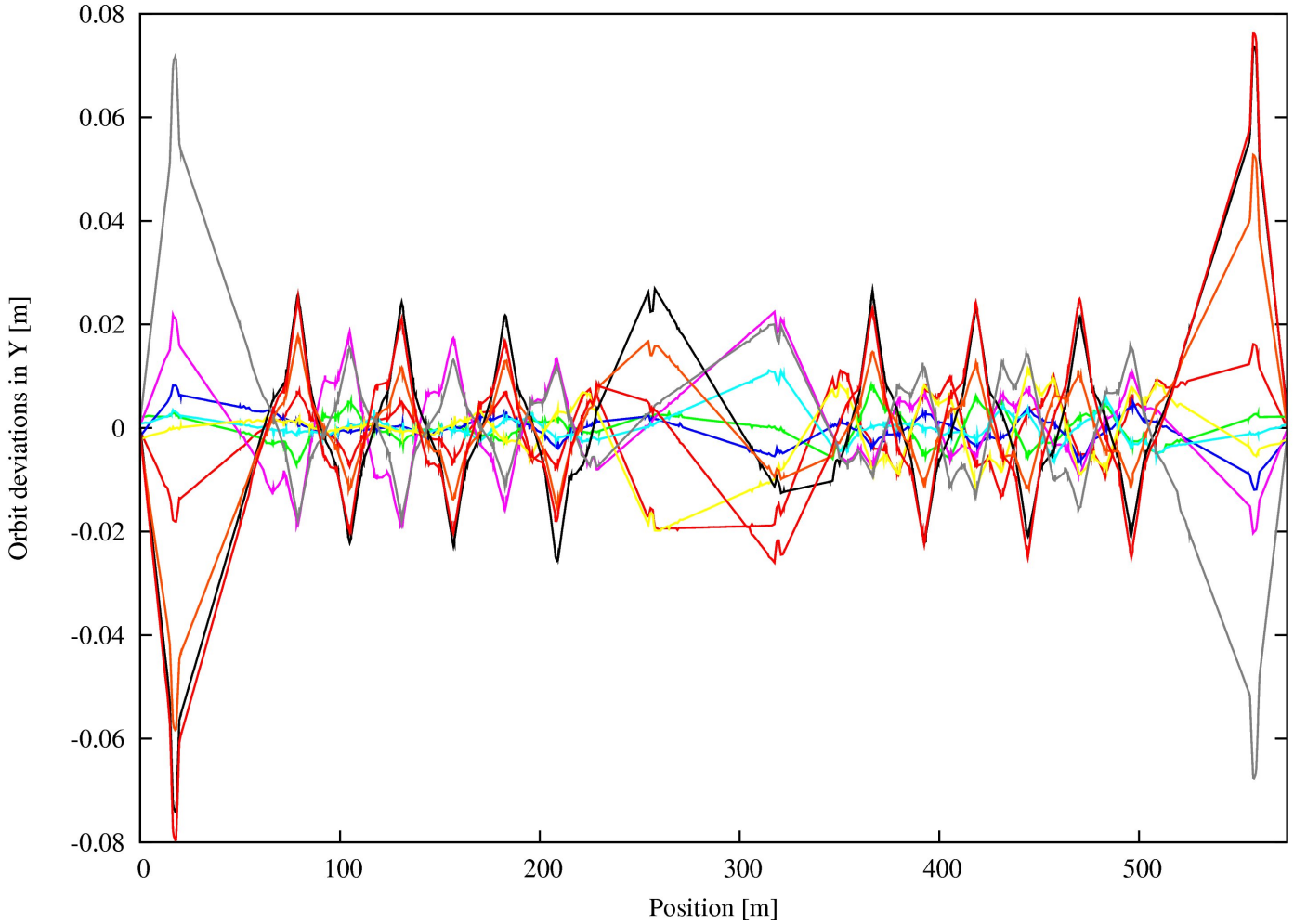

Figure 4.1: Example of uncorrected closed orbits in Y calculated with ten different seeds. The calculations are based on the $\gamma_{tr} = 6.2$ lattice. The origin is set to the target. The middle of the electron cooler solenoid magnet is located at $287.5\,m$. The $24\,m$ long cooler solenoid magnet is easy to identify since it does not include orbit correction dipole magnets. The largest deviations are located around the target which is mainly biased by large beta functions. Everywhere else in the HESR, the closed orbit deviations are a lot smaller.

	Accuracy
Scaling	0.1
Offset [mm]	0.1

Table 4.2: Measurement accuracy of beam position monitors

error types, *Gaussian* distributions have been used because they represent simulated measurement errors.

The orbit correction dipole magnets are also misaligned (see Table 4.1). Other errors like calibration errors are not taken into account. This is no limitation because an iterative and converging method like the application of an orbit response matrix is able to compensate for this. Errors of polarity of beam position monitors and orbit correction dipole magnets are easy to identify with a comparison of a measured and a calculated orbit response matrix. Thus there is no need to simulate this kind of error.

Location of beam position monitors and orbit correction dipole magnets The type of beam position monitor which will be used in the HESR is able to measure the orbit in both transverse planes. As it was described in chapter 3.2.2, they will be integrated in the sextupoles. In order to find the best locations for beam position monitors and orbit correction dipole magnets, some constraints have to be considered. On one hand the efficiency of pairs of beam position monitors and orbit correction dipole magnets scales with the square root of beta function and the phase advance in between (see equation 2.43). For chromaticity correction the efficiency of a sextupole scale with the horizontal dispersion.

Arcs There are 48 possible locations per arc for sextupoles with beam position monitors and orbit correction dipole magnets due to space restrictions. This implies that the phase advances are fixed and thus are not as important as beta functions and horizontal dispersion. The locations for beam position monitors were chosen through the sextupoles and do not break the described mirror symmetry of both arcs.

To be precise, calculations have shown that the number of necessary beam position monitors in the arcs is by four per arc lower than the number of sextupoles required by the chromaticity correction. In order to have a common design, beam position monitors will be included in all of the sextupoles.

Straight sections The straight sections have different characteristics concerning the ion-optical properties and thus beta functions due to different requirements of e.g. PANDA target or electron cooler. The placement of correction elements within the straights are characterized by beta functions which results in the correction elements being placed close or within the quadrupole triplets where possible. The mirror symmetry of the straights is maintained where possible.

Amount and distribution of correction elements The proposed orbit correction scheme consists of 64 BPMs and 48 orbit correction dipole magnets.. The orbit correction elements are distributed as follows:

- 26 BPMs per arc
- 6 BPMs per straight
- 6 horizontal and 6 vertical orbit correction dipole magnets per arc
- 6 horizontal and 6 vertical orbit correction dipole magnets per straight.

4.1.4 Closed orbit correction for HESR

The orbit response matrix method is used for the HESR. The orbit response matrix is inverted using SVD[1] because it is easy to implement in a computer code and thus in a control system for an automatic orbit correction. A computer program has been written which is able to calculated the ideal orbit response matrix from the MAD-X orbit calculations. "Ideal" means that no orbit deviations and no field errors are taken into account. After calculation of the orbit response matrix, the computer program generates the alignment errors and starts MAD-X to calculate the resulting distorted closed orbit. The distorted closed orbit is read in at the locations of the beam position monitors by the computer program including measurement errors. The necessary deflection strengths are calculated using the ideal orbit response matrix. If this correction exceed are predefined correction strength, all values of the correction are scaled by the same factor in order to match the boundary condition. This correction is applied to the MAD-X input which is used to calculate the resulting closed orbit again. This iterative process converges in a few steps and is stopped if the change of the calculated deflection strengths from one step to the other becomes smaller than 10^{-7}. The iterations are stopped if a predefined resulting closed orbit limit is reached or after ten steps anyway which was never reached.

The closed orbit correction system has to fulfill the following two requirements [75]: The maximum deflection strength of orbit correction dipole magnets shall not exceed $1\,mrad$ which is a typical value, e.g. for SIS100/300. The orbit deviations shall be corrected to below $5\,mm$.

The simulated closed orbits shown in Figure 4.1 have been corrected. For comparison purposes, they are shown in the same color code in Figure 4.2. The scale of the plot immediately shows that all presented corrected orbits are confined within the requested $5\,mm$ range. The closed orbit corrections have been performed for several thousand different seeds. Furthermore it was done for both defined ion-optical settings. The results are summarized in Table 4.3.

[1] Singular Value Decomposition

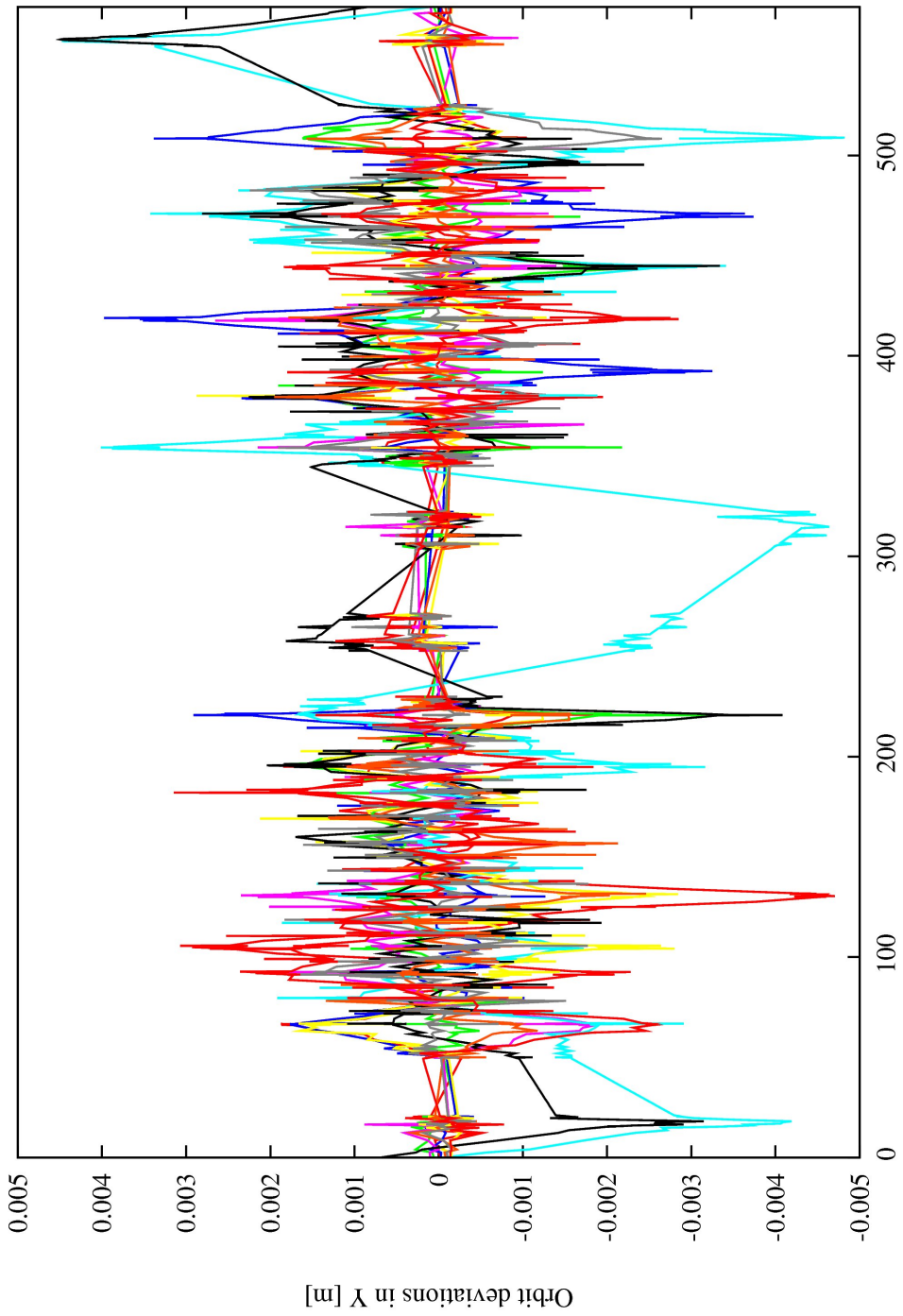

Figure 4.2: Example of corrected closed orbits in Y with ten different seeds. For comparison reasons, the seeds and colors are the same as for the uncorrected ones shown in Figure 4.1. Naturally, the calculations are also based on the $\gamma_{tr} = 6.2$ lattice. The origin is set to the target. The middle of the electron cooler solenoid magnet is located at $287.5\,m$. The corrected closed orbits are within the desired range of $\pm 5\,mm$.

Lattice	$\gamma_{tr} = 6.2$	$\gamma_{tr} = 13.3$
$X_{mean}\,[mm]$	3.34 ± 0.54	3.35 ± 0.54
$X_{min}\,[mm]$	1.88	1.92
$Y_{mean}\,[mm]$	3.51 ± 0.71	3.42 ± 0.68
$Y_{min}\,[mm]$	1.70	1.59

Table 4.3: Statistical summary of closed orbit correction simulations for different seeds and ion-optical settings. The index *mean* indicates the mean value evaluated over all maximum closed orbit deviations and *min* the minimum. The statistics for both lattice settings have been calculated from corrections with 10000 different seeds.

The minimum values do not belong to the same seeds and the goal of this investigation was the optimization concerning the $5\,mm$ constraint. The latter means that the optimization of the closed orbit correction was stopped whenever the $5\,mm$ were reached and that there is still some potential left. It also why the underlying distribution is not Gaussian as it can be observed in Figure 4.3.

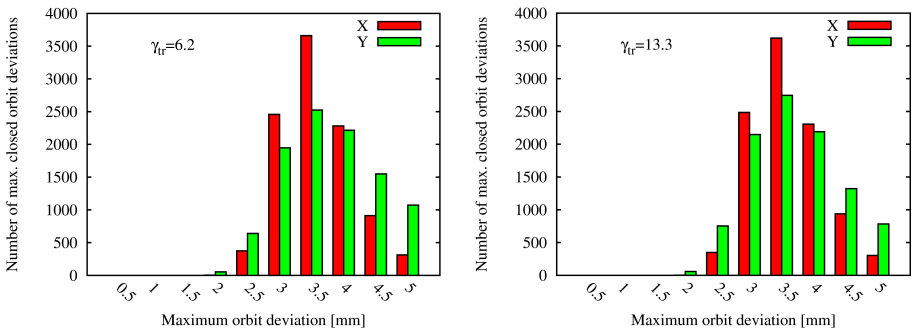

(a) $\gamma_{tr} = 6.2$ (b) $\gamma_{tr} = 13.3$

Figure 4.3: Histograms of maximum deviation of 10000 corrected closed orbits for both ion-optical settings, a) the $\gamma_{tr} = 6.2$ lattice and b) the $\gamma_{tr} = 13.3$ lattice. The scale of the abscissa marks the maximum deviation of corrected closed orbits where the numbers represent the upper limit of a range, e.g. 5 corresponds to the range of 4.5 to 5. The ordinate shows the number of maximum closed orbit deviations for the given ranges. Both histograms clarify that the distributions are not Gaussian.

The comparison of both histograms show that the distributions look very similar. This indicates that the closed orbit correction system works almost equally well for both investigated ion-optical settings.

4.1.5 Orbit correction including field errors

In order to investigate the influence of field errors on the closed orbit, MAD-X cannot be used because it takes field errors only into account for tracking. Therefore the PTC[2] module [79] of MAD-X has been used to investigate the relevance of field

[2]Polymorphic Tracking Code

errors. Closed orbit correction simulations including field errors have been performed according to the following procedure:

1. Simulate and correct closed orbit without field errors (MAD-X)
2. Retrieve needed strengths for closed correction dipole magnets
3. Use PTC with field errors and apply correction strength to orbit correction dipole magnets
4. Determine resulting maximum closed orbit deviations

This investigation was done for a smaller amount of seeds, namely 500 per ion-optical setting, which is sufficient for a cross check. The field errors which have been used can be found in chapter 5.3. The dipole errors at $1.7\,T$ main field have been used for the $\gamma_{tr} = 6.2$ lattice and at $0.17\,T$ for $\gamma_{tr} = 13.3$ one. The used quadrupole errors are the ones for a current of $550\,A$ ($\gamma_{tr} = 6.2$) and $200\,A$ ($\gamma_{tr} = 13.3$). It could be shown that the resulting closed orbits are slightly changed by the field errors. For those exceeding the $5\,mm$ border, further optimization with MAD-X has been performed. This was sufficient to fulfill the $5\,mm$ constraint even when including field errors.

The dipole field can be influenced by surrounding magnets which cause a shortening of the effective field length. Furthermore ripples of the power supplies and remanence effects also influence the close orbit. Since these effects change during a cycle and are thus dynamic, they have not been investigated. The closed orbit correction and simulations are only performed for static accelerator settings and magnet properties. Therefore, such investigations concerning dynamical changes of the accelerator and magnets have to be carried out.

4.1.6 Closed local orbit bumps for HESR

In the HESR, a good beam alignment is necessary at various locations, e.g. at the target. Closed local orbit bumps will be used to locally create controlled closed orbit deviations without affecting the global closed orbit outside of the local orbit bump. These orbit bumps have to provide enough flexibility to adjust the beam in the desired way. Typically, four correction dipole magnets will be used in the HESR to achieve an adjustment of size of the closed orbit deviation and of the transverse beam angle. Except for the toroid magnet compensation and for the H^0 closed orbit bump, a deflection angle of $1\,mrad$ is sufficient for all necessary correction dipole magnets used for local closed orbit bumps.

At the target To maximize the interactions of the circulating beam with the internal PANDA target, a good beam target overlap is crucial. There are two BPMs planned near the target to determine beam position and angle. Using a local closed orbit bump, it is possible to optimize beam target overlap by adjusting the location of the beam until the count rate found its maximum. In order to this, the beam has to be adjustable in the range from $+5$ to $-5\,mm$. Simulations have shown that $1\,mrad$ is sufficient to achieve this even with a global orbit of $5\,mm$. The simulation have been performed with an angle adjustment to $0°$. During the simulations, it

could be observe that the orbit is not fully closed and there was a slight change of the global closed orbits. This is due to the simulation where the deflection strengths are calculated from the ideal computer model whereas the closed orbit is based on a computer model which takes alignment errors into account. Such deviations can be minimized by an optimization of the computer model.

At injection The beam location and its angle have to be very accurate at the injection kicker. If the injected beam is not properly matched to the circulating one (or vice versa), this mismatch would lead to unwanted emittance growth. There are two possible ways to match both beams:

1. Change closed orbit of circulating beam, or
2. Local closed orbit bump around injection kicker.

The latter is definitely preferable since changing the global closed orbit will also change position and angle of the beam at all locations in the ring

At the H^0 detector The circulating beam has to have a good overlap with the electron beam inside the solenoid magnet. For commissioning and optimization of the electron cooler, circulating proton beams together with an H^0 detector will be used. Thus such a detector is included in the HESR design.

The designated place of the H^0 detector will be behind the electron cooler and in the middle between both quadrupole triplets. Since one wants to detect the atomic hydrogen and not the protons of the circulating beam, the beam has to be deflected away from the H^0 detector. The are two possible solutions to install the H^0 detector:

1. with a kink in the beam pipe and the H^0 detector placed outside the beam pipe or
2. placing the H^0 detector within the beam pipe and deflecting the beam around it.

The space between both triplets is $25.3\,m$. Thus, the distance from beginning of the electron cooler to the H^0 detector is approximately $57.16\,m$. Since the H^0 atoms are not charged, one has to handle the distance between recombination and detection as a drift. It is assumed in the following that both transverse phase space ellipses lie within the electron cooler which implies $|\alpha_{x,y}| \ll 1$.

The beta functions at the electron cooler are adjustable to keep the diameter of the circulating beam constant (see Table 4.4). The resulting $1\,\sigma$ radius of the atomic hydrogen beam at the detector is smaller than or equal to $10.29\,mm$. The maximum $1\,\sigma$ radius (at $1.5\,GeV/c$) of the circulating beam is in the range of $3.66\,mm$ at the detector. For injection energy ($3.8\,GeV/c$), the $1\,\sigma$ radius of the H^0 beam is much smaller (approximately $4\,mm$).

p $[GeV/c]$	ε $[mmmrad]$	β $[m]$	$u_{\max,1\sigma}$ $[mm]$	$p_{\mathrm{u,max},1\sigma}$ $[mrad]$	$u_{H_0,1\sigma}$ $[mm]$
1.5	0.637	19.6	3.53	0.18	10.29
3.8	0.250	50.0	3.54	0.07	4.00
8.9	0.107	116.0	3.52	0.03	3.52
15	0.064	196.0	3.54	0.02	3.54

Table 4.4: Preferred beta functions at electron cooler where p denotes the momentum, ε the transverse geometric emittance and β the beta functions at the electron cooler. The resulting beam radius and angle as well as the resulting H^0 beam radius at the H^0 detector are also shown. u has to be replaced by x or y.

Compensation of toroid magnet deflections at the electron cooler Toroid magnets are part of beam guiding systems of electron coolers and are bent solenoid magnets with an additional dipole field to compensate for centrifugal force. With these, the electron beam is deflected into and out of the beam pipe of the circulating beam. Since the magnetic rigidity of antiprotons and electrons differ, the deflections of antiprotons are smaller than of electrons. The deflections caused by the toroid magnets are biggest for lowest momenta. The toroid magnet design parameters are given in Table 4.5.

Bending radius of electron beam	$R_0 = 4\,m$
Magnetic strength on	$B_0 = 0.2\,T$
Bending angle of toroid magnets	$\varphi_0 = 30^\circ$

Table 4.5: Design parameters of electron cooler toroid magnets

To compensate for the deflection, four additional correction dipole magnets have to be included in the HESR lattice, two on each side of the electron cooler. The inner ones should be placed very close to the toroid magnets to keep orbit deviations introduced by transverse momenta as small as possible. At least they should correct in both planes due to space restrictions. The strengths of the correction dipole magnets have to be for $1.5\,GeV/c$ beam momentum: $28.75\,mrad$ and $3.32\,mrad$ for both planes of the the inner correction dipole magnets and $1.42\,mrad$ and $0.05\,mrad$ for both planes of the outer ones. Depending on the distance between extrapolated toroid magnet deflection and inner steerers, these values will increase. To give an example: If the distance is $0.3\,m$, the strengths increase to $31.03\,mrad$ and $3.58\,mrad$ for the inner steerers and $1.98\,mrad$ and $0.06\,mrad$ for the outer ones. As expected the increase of strength of the inner steerers is bigger than of the outer steerers.

The toroid at the entrance of the electron cooler below the cooling tower has a vertical bent whereas the toroid at the end of the interaction straight has a horizontal one (see Figure 3.3. Thus the presented solution is not symmetric on both ends of the electron cooler but can be rotated by 90° to be applicable.

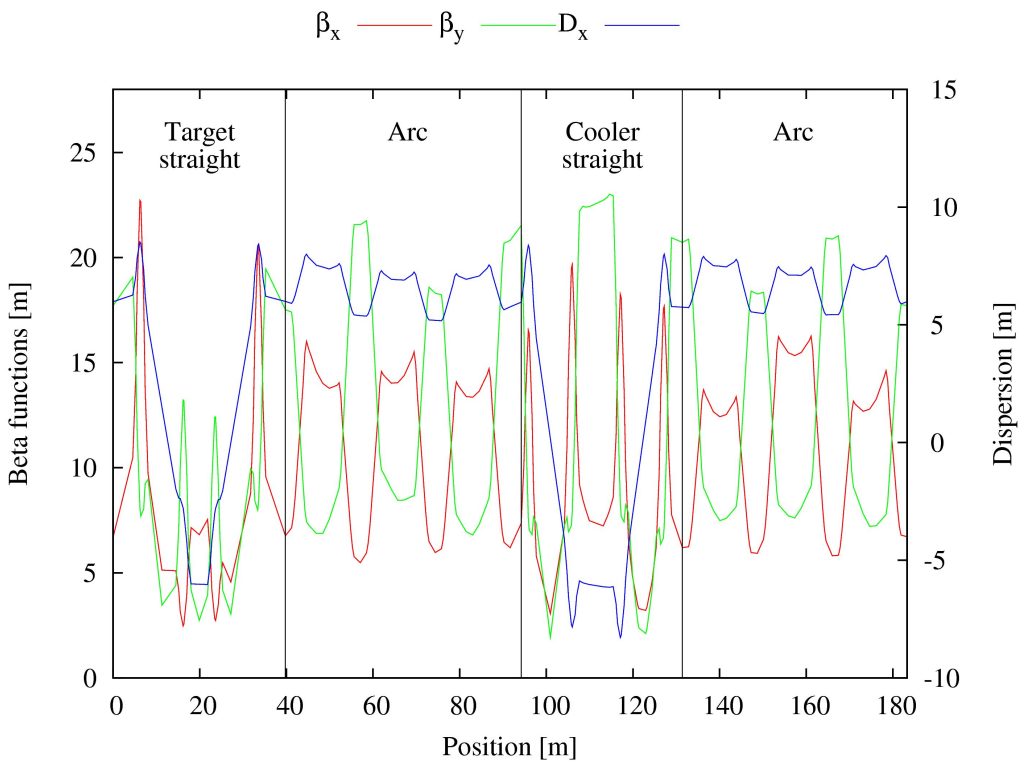

Figure 4.4: COSY ion-optics with $D \neq 0$ in straights. The main sections are indicated. The center of the electron cooler is at $s = 111.5\,m$.

4.2 Closed orbit correction at COSY

During a PAX [44, 80] beam time, an orbit response matrix was measured and applied to correct the closed orbit afterwards.

4.2.1 COSY settings

Two main settings have been used [81]. One with dispersion suppression in the straight sections. The other setting was without dispersion adjustments in the straight sections. The proton beam energy was set to 45.01 MeV which corresponds to a momentum of 294.08 MeV/c. The proton beam was electron cooled. The tunes were set to different values in the range from 3.568 to 3.623 depending on the dispersion setting as it is shown in Table 4.6. The ion-optics are exemplary shown for the $D \neq 0$ setting in Figure 4.4.

Dispersion setting	$D \neq 0$	$D = 0$
Q_x	3.620	3.580
Q_y	3.582	3.623

Table 4.6: Tune settings during experiment

4.2.2 Measuring an orbit response matrix

During the orbit response matrix measurements the $D \neq 0$ setting was used. Neglecting coupling and due to time limitations, only the uncoupled orbit response matrices for both transverse planes have been measured. For both measurements, 29 beam position monitors were available including those in the electron cooler. Although one of the electron cooler's beam position monitors is known to measure the closed orbit with an offset of approximately $3\,mm$, the measurement of the orbit response matrix is not affected since only orbit differences are taken into account. All 20 horizontal orbit correction dipole magnets, two horizontal back-leg-windings on ANKE dipole magnets, and both compensation dipole magnets next to the electron cooler toroid magnets (only deflecting horizontally) where used for the measurement of the horizontal orbit response matrix. For the measurement of the vertical orbit response matrix, 17 orbit correction dipole magnets were available.

The measurement procedure was to deflect the beam in both directions (left and right; up and down respectively) with a change of 5% in terms of current. The 5% were used as long as no beam loss was indicated by the BCT[3] signal. Otherwise the adjustment of the deflection current was reduced. The orbit changes normalized to a 1% change of current correspond to the entries in the orbit response matrix. Thus, the measured COSY orbit response matrices can be used to calculate orbit changes in terms of current changes of the deflecting devices.

4.2.3 Comparison of measured and calculated orbit response matrix

As described in section 2.1.9 the orbit response matrix can be calculated from a computer model of the accelerator. A comparison with a measured orbit response matrix can provide useful information of and optimization capabilities for the accelerator model. Besides extensive optimization and calibration routines like LOCO[82], an easy and simple check is the ratio of corresponding matrix elements. If the ratio is equal to one for all indices, the model describes the accelerator perfectly at least from the orbit response point of view. If a column or a row has only negative values, this indicates that the corresponding correction element has wrong polarity. In order to be able to compare both matrices, the measured orbit response matrix was renormalized to deflection angles in *mrad* using the calibration table of the COSY control system.

The check of the COSY orbit response matrix showed that the ratio averaged over all matrix elements is in the order of 92%. The deviations are mainly introduced by small values of matrix elements where small differences between both matrices lead to large ratios.

4.2.4 Closed orbit correction

Although the orbit response matrix was measured for one specific optical setting, its application for other optical settings like the dispersion suppressed one worked

[3]Beam current transformer

considerably well. The orbit response matrix was used as it is which means that it was not inverted but a χ^2 minimization with a feed-forward method was applied. This kind of application takes more time for calculations due to the variation of corrector strengths but is easier and faster to set up.

A problem that occurred during the measurement of the orbit response matrix was related to the electron cooler and its toroids. A usual machine setup would be to correct the closed orbit and then to set up the toroid magnet compensation for the electron cooler on top of it. Instead, the local orbit bump for the electron cooler was set up with an uncorrected closed orbit and could not be easily adjusted afterwards. Thus, the closed orbit correction using the orbit response matrix was performed to correct the closed orbit under the constraint that the toroid magnet compensation had to be artificially maintained. This was done to prevent a change of the closed orbit within the electron cooler and therefore not to limit the cooling capabilities. The application of the orbit response matrix with local boundary conditions led to not fully corrected closed orbits. A distortion of the local closed orbit bump around the electron cooler could not be prevented and caused worse beam overlap of the proton and electron beams resulting in weaker cooling. The orbit correction had to be stopped after two iterations since the cooling capabilities were restricted too strongly after the third iteration.

Figure 4.5 shows the results of the orbit correction for both planes together with the uncorrected closed orbit as well as the distortion of the local closed orbit bump around the electron cooler.

4.3 Discussion of results

Based on the alignment errors of COSY, closed orbit simulations have been performed for the HESR. They show that the uncorrected closed orbit deviations can be nearly as large as $100\,mm$ which is more than twice the beam pipe radius of $44.5\,mm$. The most serious excursion occur near the target which is biased by the large beta functions in the surrounding triplets. Elsewhere is the HESR, the closed orbit deviations are by more than a factor two smaller and at least close to the beam pipe radius. Even so, the situation is not as worse as for the superconducting version of the HESR.

In order to limit the closed orbit deviations, a closed orbit correction consisting of 48 closed orbit correction dipoles and 64 beam position monitors has been developed and tested by various simulations. The boundary conditions of $1\,mrad$ maximum deflection strength at $15\,GeV/c$ and a resulting closed orbit of less than $5\,mm$ have been satisfied. Statistical investigations have also shown that the developed closed orbit correction system works almost equally well for both ion-optical settings, the $\gamma_{tr} = 6.2$ and the $\gamma_{tr} = 13.3$ lattice. The necessary closed orbit bumps have been checked not to exceed an additional $1\,mrad$.

The orbit response matrix has been measured for COSY. Its application has shown that the for the HESR proposed correction method performs as expected except for the cooler bump. The correction below $7.5\,mm$ was not possible due to the toroid magnet compensation bump around the electron cooler. The compen-

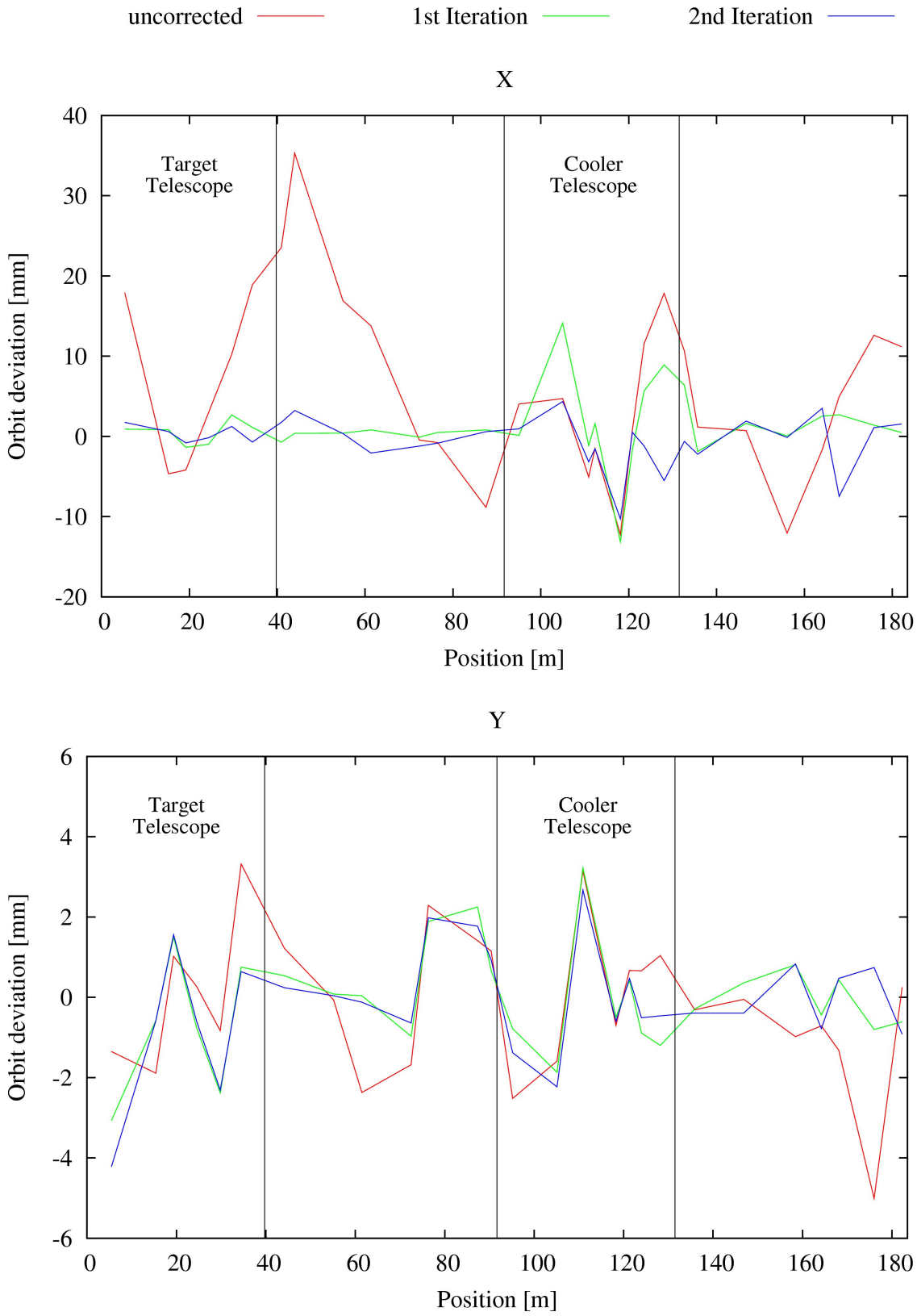

Figure 4.5: Horizontal (top) and vertical (below) closed orbit correction for COSY. The electron cooler is located at nearly 111 m. The toroid magnet compensation from approximately 104 m to about 120 m around the electron cooler becomes distorted. The vertical orbit is in general much better. The third iteration is not shown because it could not be used due to the weak electron cooling.

sation bump could not be adjusted and had to be artificially maintained during orbit correction. On one hand, this restricted the number of iterations to two (For comparison: The HESR closed orbit simulations were performed with up to ten iterations). The third iteration which was not shown restricted the cooling capabilities of the electron cooler too much and thus could not be used. On the other hand, there was no chance to correct all orbit deviations larger than the intended $5\,mm$ due to overcompensation and the use of a global correction scheme with the local boundary conditions. Therefore it is necessary for future closed orbit corrections at COSY and the HESR to adjust the orbit bump around the electron cooler after each iteration step of the closed orbit correction in order to regain the cooling capabilities as it was done for the closed orbit simulations.

Chapter 5

Dynamic aperture and frequency map analysis

This chapter contains the calculations of dynamic aperture and frequency map analysis. In addition the choice of sextupole locations for chromaticity correction is discussed.

5.1 Dynamic aperture calculations

Dynamic aperture calculations are always related to the question of computation time. Tracking a whole six dimensional phase space can take easily weeks, months, and even year depending on its density and number of turns. Thus a proper reduction of the problem is inevitable.

Several restrictions had to be made to match the available computation time and power:

- The phase space of start coordinates of all particles has been restricted to the x,y-plane which is a common procedure [23]. Cross checks have been performed to prove this restriction to be valid.

- The dynamic aperture calculations are limited to the short term region which ranges from several hundreds to a few thousands of turns. This is justified by the kind of investigation performed in this thesis. The betatron motion and related resonances which are driven by field errors of the magnets develop in this range of turns [24]. Furthermore 2000 turns are sufficient to calculate the diffusion coefficient [25].

- The relative momentum deviation is also taken into account but for discrete values only. Calculations have been performed for on-momentum particles and off-momentum particles with a maximum relative momentum deviation of $\pm 3\sigma$.

In order to be able to compare the dynamic aperture with the geometric acceptance limit which is determined by the beam size and the dimensions of the vacuum chamber, all dynamic aperture calculations have its starting point at the geometric

acceptance limit. This is located in the triplets around the target with the maximum beta functions.

The calculation of the dynamic aperture is performed in the following way: The linear lattice is calculated by MAD-X and read into SIMBAD. The non-linearities of field errors and sextupole magnets are introduced in SIMBAD via thin non-linear kicks. The individual field errors of magnets are generated by a pseudo random number generator and are Gaussian distributed. The seed of the generator can and has been changed for statistical purposes. A grid of starting coordinates of particles is created in the x,y-plane. Using SIMBAD, particles are tracked through the HESR non-linear computer model for a specified amount of turns. The starting coordinates of surviving particles are transformed into transverse emittances using the twiss parameters. The boundary condition of equal transverse emittances restricts the dynamic aperture to be the largest circle covering the stable area in this emittance-based, two dimensional phase space.

The dynamic aperture calculations have been used to develop and optimize a chromaticity correction scheme using sextupoles and to optimize the field errors of the beam guiding magnets. Naturally, there will be other non-linearities in the HESR which are not covered by this thesis e.g. space charge effects [18] or the non-linear kicks caused by the electron cooler's beam [83, 84]. Both act on different time scales.

5.2 Arrangement of sextupole magnets for chromaticity correction

Chromaticity leads to a tune spread induced by the momentum spread of the beam. Thus a chromaticity correction scheme had to be developed for the HESR [85]. Chromaticity can be corrected at places with non-zero dispersion only which means that all sextupole magnets for chromaticity correction have to be installed in the arcs. Sextupole magnets are the lowest multipole creating non-linear forces. The non-linear effect on beam dynamics should be as small as possible or compensated for if manageable to prevent the dynamic aperture from shrinking.

The usage of driving term techniques led not to the desired results. This is no surprise since firstly the dynamic aperture defines the border to the chaotic motion and thus far away from the area where those techniques can be applied [86]. Secondly, the sextupole magnets contribute to ten first order driving terms. All phase dependent ones need two families to be properly controlled. This adds up to 12 families for correction of first order chromaticities and geometric driving terms which drive betatron resonances. This does not even regard e.g. second order dispersion. But, the HESR lattice does not provide the necessary conditions like phase advances and there are not enough sextupoles to justify a splitting into the desired number of sextupole magnet families. Instead of a driving term approach, a kind of brute-force computation was used where the effect of pairs of sextupole magnets on the dynamic aperture is evaluated. This means that that the investigation search for pairs of sextupole magnets which decrease the dynamic aperture as little as possible. These pairs compensate for best at design tune for which this investigations have

been performed. The calculations are based on the linear lattices ($\gamma_{tr} = 6.2$ and $\gamma_{tr} = 13.3$) and the sextupole magnets being the only no-linear elements.

The best compensating sextupole magnets pairs are different for both ion-optical settings. And unfortunately there are not enough of those pairs to fully correct chromaticity. Thus additional pairs of sextupole magnets have to be used. The natural grouping into two families of horizontal focusing and of vertical focusing sextupole magnets is sufficient to correct chromaticity. But if split further into four families to separate the best compensating from the weaker compensating sextupoles, the negative effects on stability can be reduced by powering best compensating sextupoles stronger than the other ones.

There are two more vertical focusing sextupole magnets per arc than horizontal. These are necessary because the shape of the horizontal dispersion function is different for both ion-optical settings (see Figure 3.4). The overall sum of sextupole magnets in the arcs is 52.

The dynamic aperture was calculated for both ion-optical settings and with two and four sextupole families: The dynamic aperture of the $\gamma_{tr} = 6.2$ lattice could be increased from 817 $mm\,mrad$ to 1125 $mm\,mrad$ by using four families. The dynamic aperture of the $\gamma_{tr} = 13.3$ is in general much smaller. It is 79 $mm\,mrad$ for the design tunes. A different choice of tunes can help to increase this value. It is not easy if not impossible to determine if the tunes in general or the phase advances between the sextupoles are worse than for the $\gamma_{tr} = 6.2$ lattice. Even so, it is possible to improve the dynamic aperture with the same grouping into four sextupole families with different strengths. The maximum improvement achieved is in the order of 15% with a value of 91 $mm\,mrad$.

5.3 Field errors of the HESR magnets

Since no magnet can be designed and built to provide a single wanted magnetic field configuration like a pure dipole field, field errors have to be taken into account:

Dipole magnet The field errors of the dipole magnets have been estimated using 3D field calculations [87] (see Table 5.1) which is an explanation why field errors consist of upright field components only. The dipole magnet is optimized for $1\,T$ which is reflected by the relative field errors for $1\,T$ main field since all of them are smaller than 10^{-4}. Further away from the design main field, the relative field errors increase partially by more than one order of magnitude.

The first dipole magnet design inherited a sextupole field component with a relative strength of $b_2 = 28.16 \cdot 10^{-4}$ at $1.7\,T$ main field. Such a sextupole field component affects chromaticity strongly. The integrated sextupole field strength of a dipole magnet at $1.7\,T$ is with a value of nearly $0.75\,m^{-2}$ roughly three times larger than the maximum integrated strength of a single sextupole magnet (see chapter 3.2.2). The resulting chromaticity was in the order of $\xi_x > 70$ and $\xi_y < -70$ which the regular sextupole magnets were not able to compensate for.

Thus the dipole magnet design has been further optimized. With the introduction of gaps into the iron yoke the relative sextupole field component could be

	First design			Optimized design		
Component	$0.17\,T$	$1.0\,T$	$1.7\,T$	$0.17\,T$	$1.0\,T$	$1.7\,T$
4-pole	-0.03	0.01	0.10	-0.03	0.01	0.10
6-pole	-4.32	0.72	28.16	-1.57	0.88	3.52
8-pole	0.04	0.06	0.09	0.04	0.06	0.09
10-pole	-1.62	-0.05	6.03	-0.44	0.53	7.96
12-pole	0.01	0.01	0.01	0.01	0.01	0.01
14-pole	-0.06	0.10	0.43	0.03	0.13	0.79
16-pole	$< 10^{-2}$	$< 10^{-2}$	$< 10^{-2}$	$< 10^{-2}$	$< 10^{-2}$	$< 10^{-2}$
18-pole	0.06	0.04	-0.10	0.06	0.05	-0.23
20-pole	$< 10^{-2}$	$< 10^{-2}$	$< 10^{-2}$	$< 10^{-2}$	$< 10^{-2}$	$< 10^{-2}$

Table 5.1: Relative field errors of the bending dipole magnet retrieved from 3D calculations. All values are in units of 10^{-4}. Values are upright values only. The field of $0.17\,T$ corresponds to $1.5\,GeV/c$, $1.0\,T$ to $8.9\,GeV/c$, and $1.7\,T$ to $15\,GeV/c$ respectively. The reference radius of this multipole expansion is $33\,mm$.

reduced by a factor eight to $b_2 = 3.52 \cdot 10^{-4}$ at $1.7\,T$ without making the situation worse at $0.17\,T$ [54]. The value for $0.17\,T$ decreased by roughly a factor three resulting in a chromaticity which is very close to the natural chromaticity for $0.17\,T$ main field. The chromaticity becomes $\xi_x \approx -4.80$ and $\xi_y \approx -17.96$ for $1.7\,T$ main field. A small drawback of the dipole optimization is the increase of the relative decapole field component by 32% to $b_4 = 7.96 \cdot 10^{-4}$ at $1.7\,T$ main field. But at $0.17\,T$ the relative decapole even decreased by nearly by a factor four. In general, the relative field errors are smaller than $1 \cdot 10^{-4}$ except for the sextupole and decapole field components.

For the following dynamic aperture calculations which take field errors into account, the field errors for $1.7\,T$ and $0.17\,T$ have been used.

Quadrupole magnet Since the HESR quadrupole magnet design is based on the COSY quadrupole magnets, the field errors of the latter are used for calculations and have been taken from field measurements (see Table 5.2). The four-part yoke of the HESR quadrupole magnets compared to the two-part yoke of the COSY ones lead to an estimated increase of the field errors of 10% [55]. This increase is taken into account for all calculations although the values in Table 5.2 do not include it since the measured field errors of the COSY quadrupole magnets are shown.

Although there exist also measurements for a current of $400\,A$, it was preferred to use $550\,A$ for a worst case estimate due to saturation effects. The by far strongest relative field errors are the 12- and 20-pole ones. For the highest current of $550\,A$ the normal 12-pole relative field component has a strength of $b_5 = 49.03 \cdot 10^{-4}$. The 20-pole relative field component is even stronger more than doubling the 12-pole one. All other except from the skew 12-pole ($a_5 = 13.37 \cdot 10^{-4}$) field component are smaller than $5.5 \cdot 10^{-4}$. For low currents near $200\,A$, the absolute value of normal and skew 12-pole relative field component are almost equal ($b_4 \approx -a_4 \approx 10 \cdot 10^{-4}$). Still the 20-pole is dominant being approximately a factor eight larger.

	200 A		550 A	
Component	Normal	Skew	Normal	Skew
6-pole	0.37 ± 0.33	0.91 ± 0.21	1.75 ± 0.24	4.73 ± 0.67
8-pole	0.25 ± 0.63	2.05 ± 1.72	-1.13 ± 0.68	-0.02 ± 0.22
10-pole	-0.70 ± 0.28	0.91 ± 0.61	-0.13 ± 0.23	-0.09 ± 0.34
12-pole	-10.33 ± 0.82	10.28 ± 0.47	49.03 ± 2.14	13.37 ± 0.41
14-pole	-0.73 ± 0.20	2.82 ± 2.25	-1.17 ± 0.26	-1.17 ± 0.19
16-pole	3.19 ± 0.38	6.51 ± 0.58	3.08 ± 0.29	5.49 ± 0.54
18-pole	-0.09 ± 0.40	0.03 ± 0.66	0.02 ± 0.16	0.22 ± 0.15
20-pole	83.66 ± 0.83	2.99 ± 0.81	107.76 ± 0.62	3.34 ± 0.25

Table 5.2: Relative field errors of COSY quadrupole magnets. All values are given in units of 10^{-4}. The errors of quadrupole magnets do not include the 10% increase due to the iron yoke of the HESR type. The reference radius of this multipole expansion is $70\,mm$. The current of $200\,A$ corresponds to a gradient of approximately $3.6\,T/m$ and $550\,A$ to $10\,T/m$.

5.4 The $\gamma_{tr} = 6.2$ lattice

The most frequently used ion-optical setting will be the $\gamma_{tr} = 6.2$ lattice. This is justified by the main PANDA experiment. Therefore a simulation for $15\,GeV/c$ is a worst case estimate due to field errors and important for possible future upgrades. The geometric emittance is $\varepsilon = 0.0637\,mm\,mrad$ ($\varepsilon_{norm} = 1\,mm\,mrad$) at $15\,GeV/c$ or $\varepsilon = 0.107\,mm\,mrad$ at $8.9\,GeV/c$. The emittance at $15\,GeV/c$ is used in the following if not stated otherwise. The field errors which are taken into account are errors of the dipole magnet at $1.7\,T$ main field and of the quadrupole magnet at $550\,A$. The design tunes are $Q_x = 7.618$, $Q_y = 7.624$.

5.4.1 Tune scans

While the frequency map analysis indicate which resonances are driven at a specific tune setting, a tune scan provides information about strongest resonances over a whole area in the tune diagram. Since momentum spread and other effects can lead to coherent and incoherent tune spread, tune scans are also used to find tune areas with enough space and large dynamic aperture. Such a tune scan for $\frac{\Delta p}{p} = 0$ is shown in Figure 5.1.

The strongest resonance seen in the tune scan corresponds to the octupole resonance line $2 \cdot Q_x + 2 \cdot Q_y = 31$. This can be indeed a fourth order resonance driven mainly by the 12- and 20-pole field components of the quadrupole magnets. But the skew octupole resonance $3 \cdot Q_x + Q_y = 31$ is presumably the eighth order resonance $6 \cdot Q_x + 2 \cdot Q_y = 62$ which reflect the fact that the skew field components of the quadrupole magnets are relatively small compared to the upright ones. Stating this, the main contribution to the first fourth order resonance line $2 \cdot Q_x + 2 \cdot Q_y = 31$ can also be the eighth order resonance $4 \cdot Q_x + 4 \cdot Q_y = 62$ or an overlap. A separation is almost impossible since different driving terms contribute to the resonances.

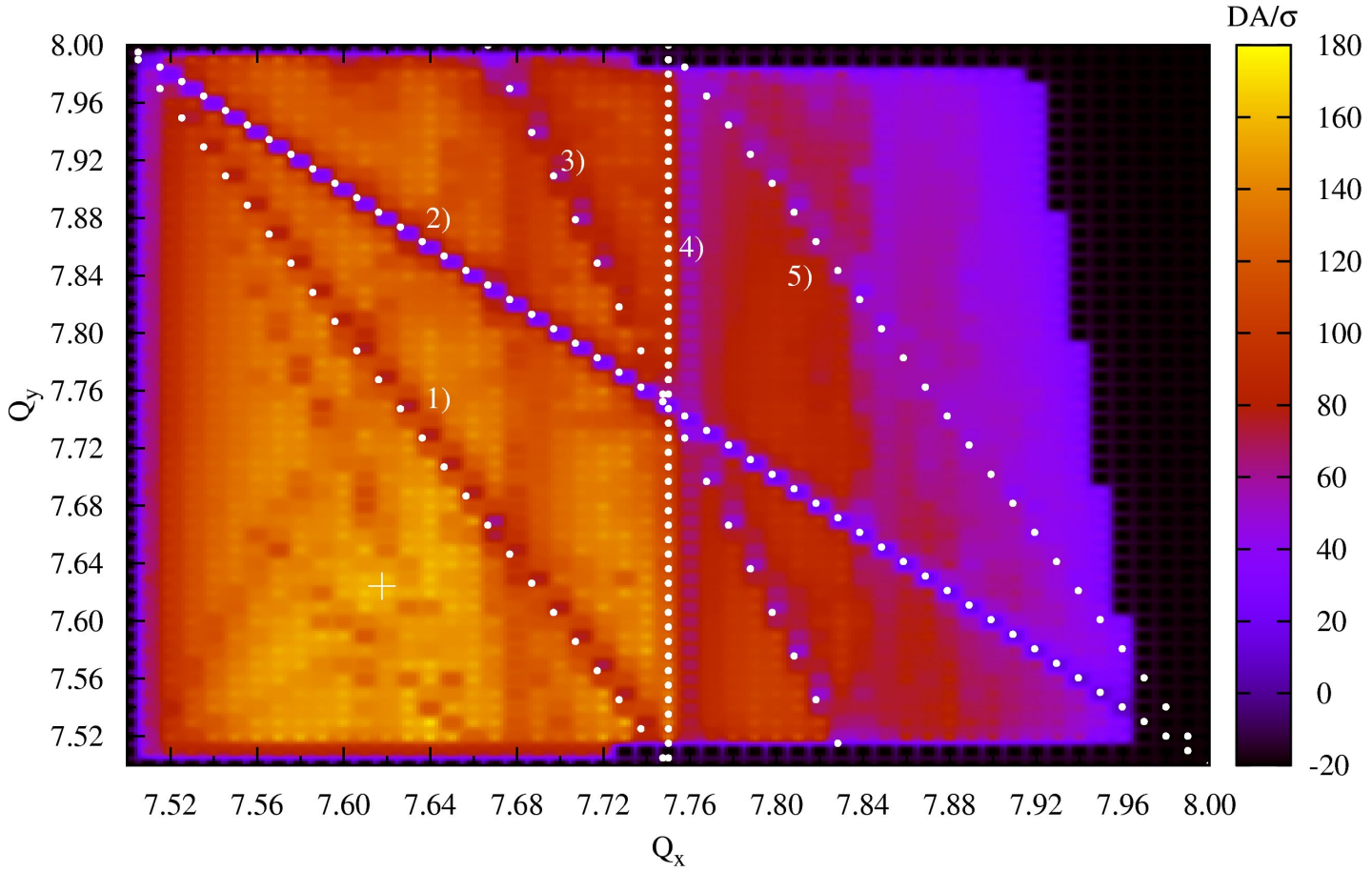

Figure 5.1: Tune scan for $\gamma_{tr} = 6.2$ lattice and on-momentum particles tracked over 1000 turns. The color scale is given in DA/σ. This is the dynamic aperture divided by the 1σ emittance. The value of -20 is artificial and represent an unstable linear lattice. It is used to separate unstable tunes of the linear modell from zero dynamic aperture. The strongest resonance lines have been identified and marked: 1) Skew Sextupole $2 \cdot Q_x + Q_y = 23$; 2) Octupole $2 \cdot Q_x + 2 \cdot Q_y = 31$; 3) Skew Octupole $3 \cdot Q_x + Q_y = 31$; 4) Octupole $4 \cdot Q_x = 31$; 5) 12-pole $4 \cdot Q_x + 2 \cdot Q_y = 47$. The design tunes are marked by a cross.

One example: The resonance line $2 \cdot Q_x + 2 \cdot Q_y = 31$ is a fourth order resonance. The corresponding first order octupole driving term is h_{20200}. The 12-pole first order driving terms which contribute to the very same resonance are h_{31200} and h_{20310}. For the 20-pole there are even more: h_{53200}, h_{42310}, h_{31420}, and h_{20530}. Other multipole field components can also contribute in first order. And it gets even worse: The resonance lines $4 \cdot Q_x + 4 \cdot Q_y = 62$ and $2 \cdot Q_x + 2 \cdot Q_y = 31$ overlap which means that even more driving terms are relevant. The driving terms h_{51400} and the h_{40510} are the corresponding first order 20-pole driving terms. Even so, all those driving terms contribute in first order solely. Higher orders can and do also contribute, e.g. two sextupole driving terms contribute to octupole driving terms and thus to fourth order resonances.

Coming back to the resonance identification: Also the resonance like $2 \cdot Q_x + Q_y = 23$ belongs most likely not to a skew sextupole resonance. The next higher order resonance overlapping is the sixth order resonance $4 \cdot Q_x + 2 \cdot Q_y = 46$ which would correspond to the strong 12-pole component in the quadrupole magnets. A second evidence is the other sixth order resonance (marked by a 5) seen in the tune scan: $4 \cdot Q_x + 2 \cdot Q_y = 47$.

The resonance line $4Q_x = 31$ can be observed but with a slight shift to the horizontal integer tune. From the resonance condition, it should be located at $Q_x = 7.75$ as the dotted line indicates. But in fact the resonance line is moved to $Q_x = 7.76$. This is partly caused by the grid density and data processing. But a closer look reveals that the resonance seems to be indeed shifted and also asymmetric. The left shoulder has a sharper fall than the right one. The same can be observed for the third order resonance $3Q_x = 23$ at $Q_x = 7.68$ which is one of the observable weaker resonances. Similar behavior could be observed during the development of the chromaticity correction scheme. Simulations with a single sextupole and a single octupole magnet have shown that this resonance line can be shifted depending on the octupole strength. And also the shapes of the shoulders and the depth of the resonance changed with the octupole magnet strength. This is caused by a frequency mixing which affects the resonance characteristics.

The dynamic aperture decreases approaching the horizontal integer resonance $Q_x = 8$. This can be explained by a mismatch of the arcs and straight sections leading to large beta functions in the triplets around the target. This translates via increase of beam size together with the field errors in the quadrupole magnets to stronger non-linearities and results in a decrease of the dynamic aperture. The dynamic aperture shrinks until even the linear lattice becomes unstable due to the mismatch. This is denoted by a black area on the right hand side near the integer resonance. Since the design tune and thus the tune area of main interest is far from being integer, this is no restriction at all.

One important information though cannot be displayed in a two-dimensional tune scan: The relation of geometric acceptance limit and dynamic aperture. A reduction to one-dimensional tune scans, e.g. with one of the tunes fixed, can be an appropriate way for such a comparison. This kind of tune scans are exemplary shown in Figure 5.2.

The tune scan reflects the behavior of the linear lattice. The change of tunes lets the maximum beta functions grow due to the mismatch which reduces the ge-

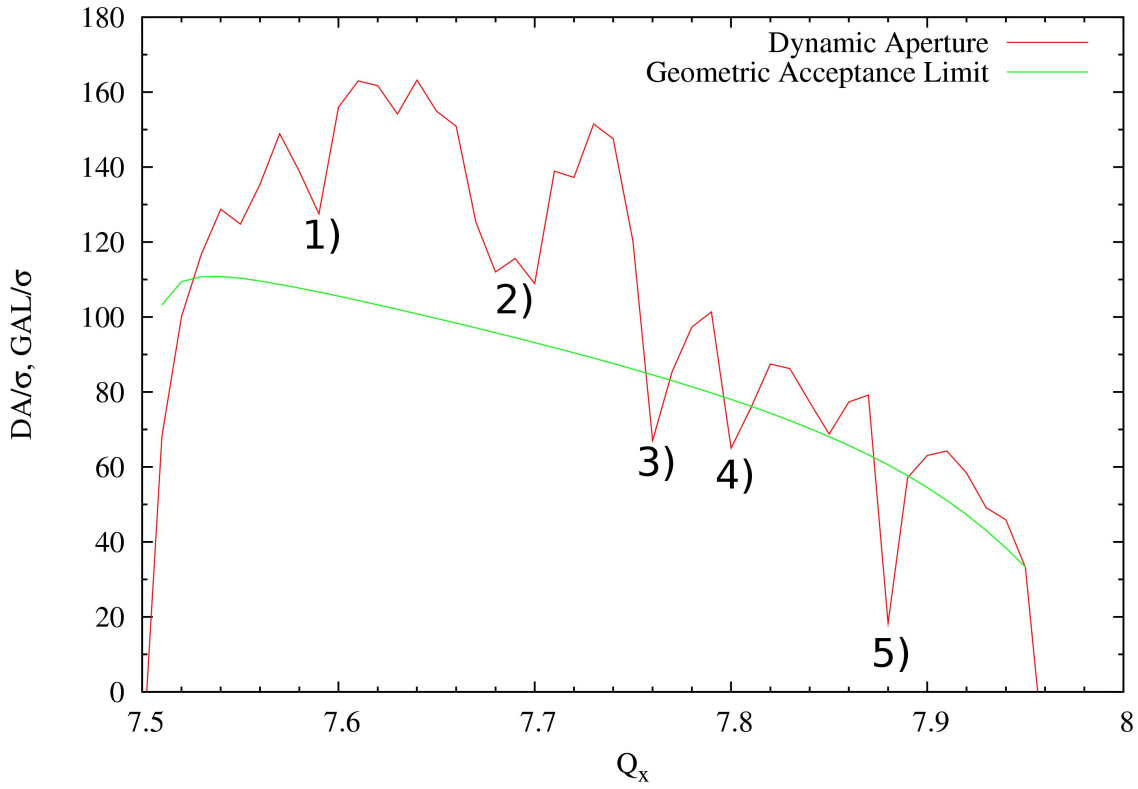

(a) Tune scan with vertical tune fixed at $Q_y = 7.62$

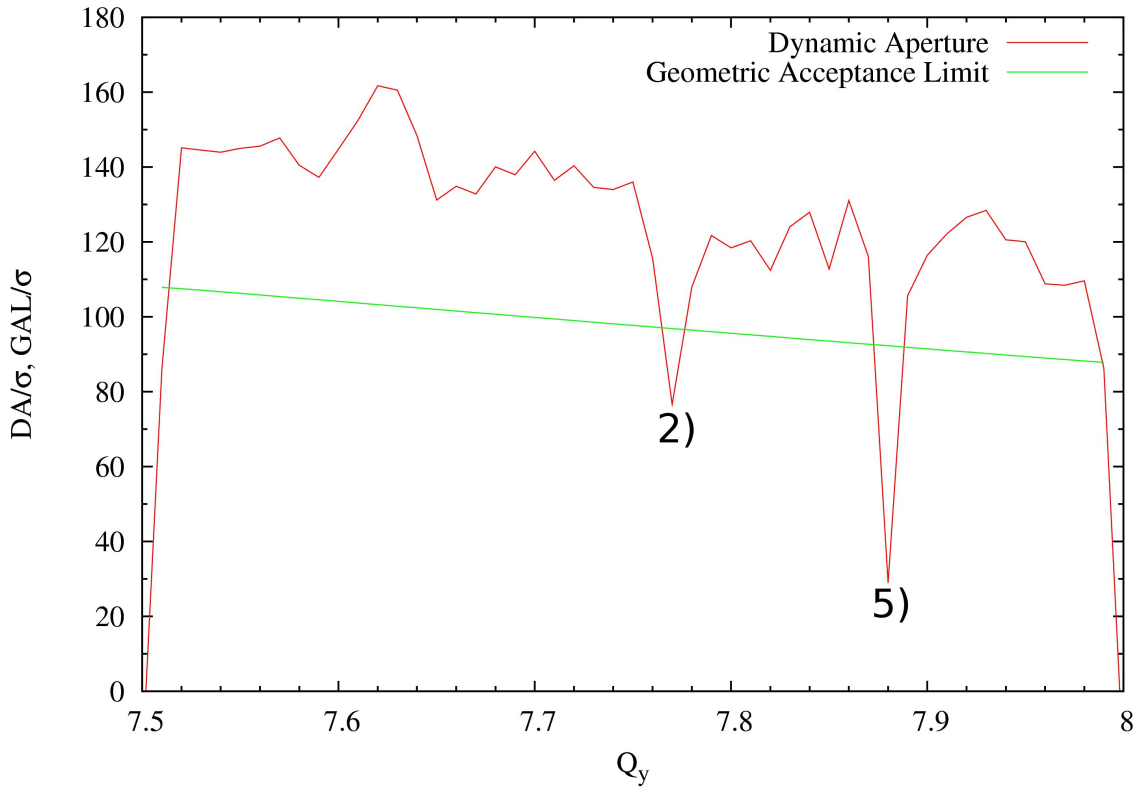

(b) Tune scan with horizontal tune fixed at $Q_x = 7.62$. The mark 2) refers in this case to resonance line $2 \cdot Q_x + Q_y = 23$ only.

Figure 5.2: Tune scan for fixed vertical tunes $Q_{x,y} = 7.62$. The geometric aperture plotted in green clarifies the described increase of maximum beta functions until linear lattice becomes unstable. Strongest resonance lines have been identified using 2D tune scan: 1) $6 \cdot Q_x + 4 \cdot Q_y = 77$; 2) overlap of resonances lines $2 \cdot Q_x + Q_y = 23$ and $3 \cdot Q_x = 23$; 3) $4 \cdot Q_x = 31$; 4) $3 \cdot Q_x + Q_y = 31$; 5) $2 \cdot Q_x + 2 \cdot Q_y = 31$

ometrical acceptance limit until the linear lattice becomes unstable. This happens close to the integer and also close to the half integer tune values in the case of the horizontal tune being fixed. It also shows a linear decrease of the geometric acceptance limit. For a fixed vertical tune it is different: The decrease is not linear and the transition to an unstable linear lattice occurs further away from the integer tune value. Overall, the linear lattice is clearly more sensitive to changes of the horizontal tune. The consideration of the geometrical acceptance limit is an advantage of this kind of data representation since it also provides information of acceptance reserve. Although one-dimensional tune scans show a resonance structure, an identification of resonances is easier to performed using two dimensional tune scans. Although it is possible to estimate the depth and width of resonances from one dimensional tune scans, the direction of approaching the resonances and possible overlap make things difficult.

5.4.2 Design tunes

The design tunes of the $\gamma_{tr} = 6.2$ lattice are $Q_x = 7.618$, $Q_y = 7.624$ and therefore close to the $Q_x - Q_y = 0$ skew quadrupole difference resonance.

The frequency map analysis does not only provide information about tunes of single particles but also a stability criterion, the diffusion coefficient. The combination of tunes and diffusion coefficient in a single plot reveals the web of resonances[1] affecting particle stability. Furthermore the dynamic aperture is of another quality if combined with the diffusion coefficient since it transports resonance structures into the dynamic aperture plots. Besides the resonance structure long-term predictions are made possible.

Both types of plots are shown in Figure 5.3 for on-momentum particles ($\frac{\Delta p}{p} = 0$). The first plot shows the frequency map where a resonance knot can be seen at $Q_x = Q_y = 7.625$. A second resonance knot at$Q_x = Q_y = 7.666$ is too far away to be displayed. The strongest resonances have been identified and are marked by resonance lines. The resonance lines themselves can be identified by a tiplet of integers written at one end. A triplet is given in form of m, n, p which represents the resonance condition $m \cdot Q_x + n \cdot Q_y = p$. Resonances do not necessarily correlate with the order of a multipole driving it although first order effects are in general the strongest.

The resonance web is split by the skew quadrupole difference resonance $Q_x - Q_y = 0$ into a main part on the left hand side and an island on the right hand side. This resonance is one of the strongest resonances accumulating particles on it and only few particles surrounding it. It also crosses both resonance knots. The resonance knot at $Q_x = Q_y = 7.625$ is closest to the design tunes. Most of the relevant resonances which cross this resonance knot are of eighth order.

This is reflected by eight hyperbolic fixpoints in the chaotic region of the horizontal phase space plots in Figure 5.4. The phase space plots show a thin chaotic layer inside the stable region. This layer is located at $15\,mm$ which is closely located to the transition of the very stable, dark blue area in the dynamic aperture plot to

[1] so called Arnold web [28]

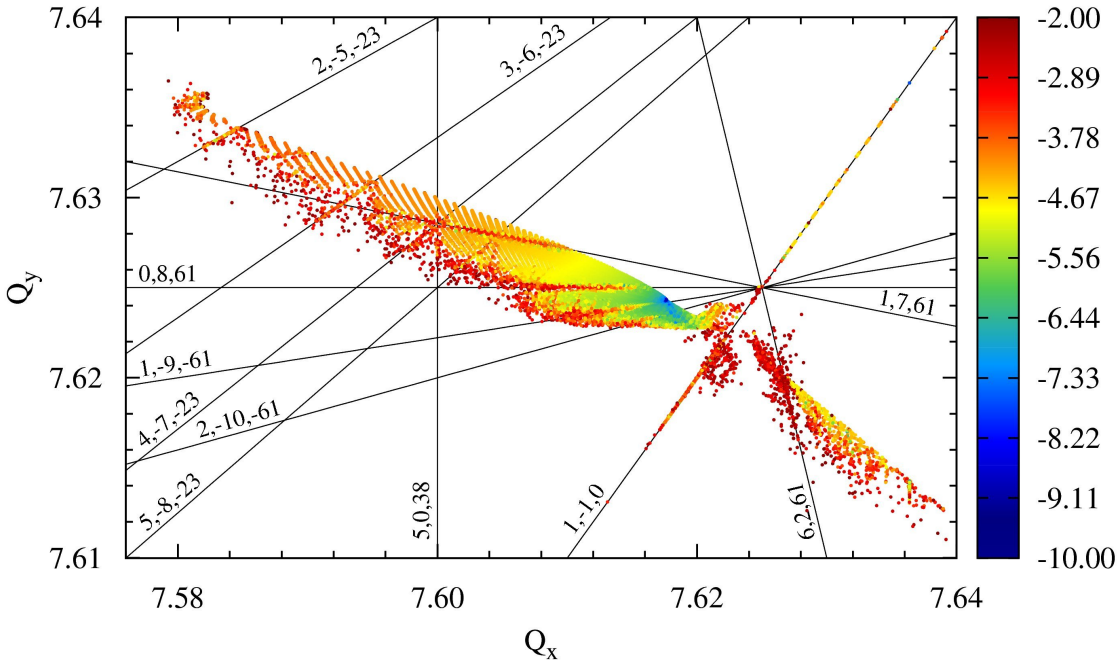

(a) Frequency Map with identified resonances

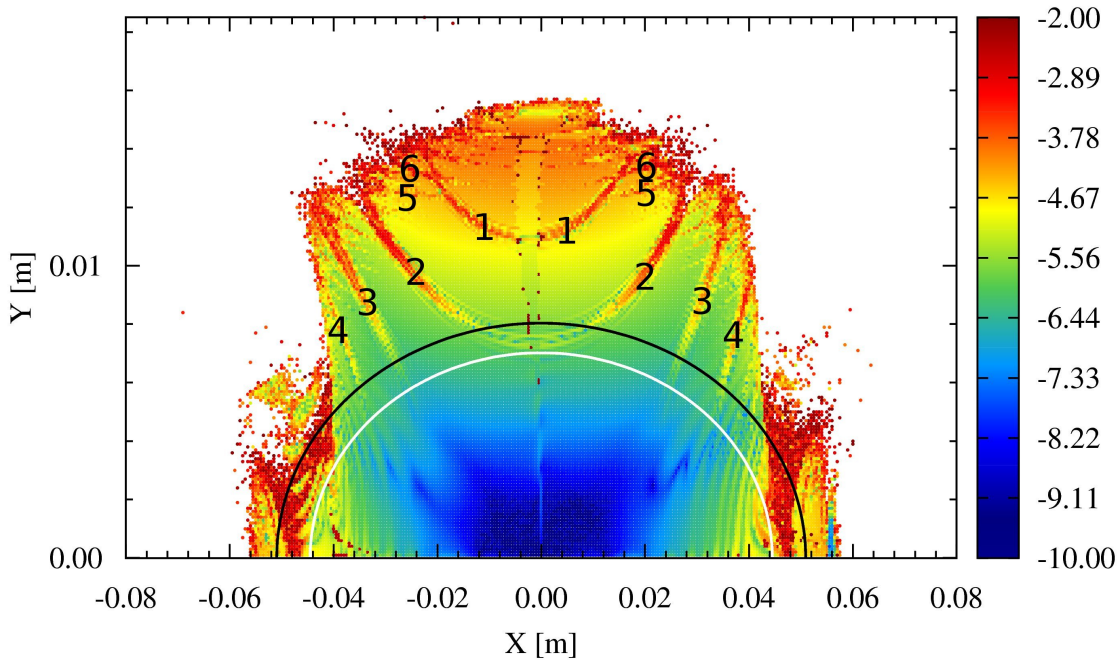

(b) Dynamic aperture

Figure 5.3: Frequency map and corresponding dynamic aperture for $\frac{\Delta p}{p} = 0$. The color scale represent the diffusion coefficient. The two curves in b) represent emittances at the geometrical acceptance limit (white) and at the dynamic aperture (black). The numbers in b) denote the resonances: 1) 1,7,61; 2) 0,8,61; 3) 1,-9,-61; 4) 2,-10,-61; 5) 5,-8,-23; 6) 4,-7,-23

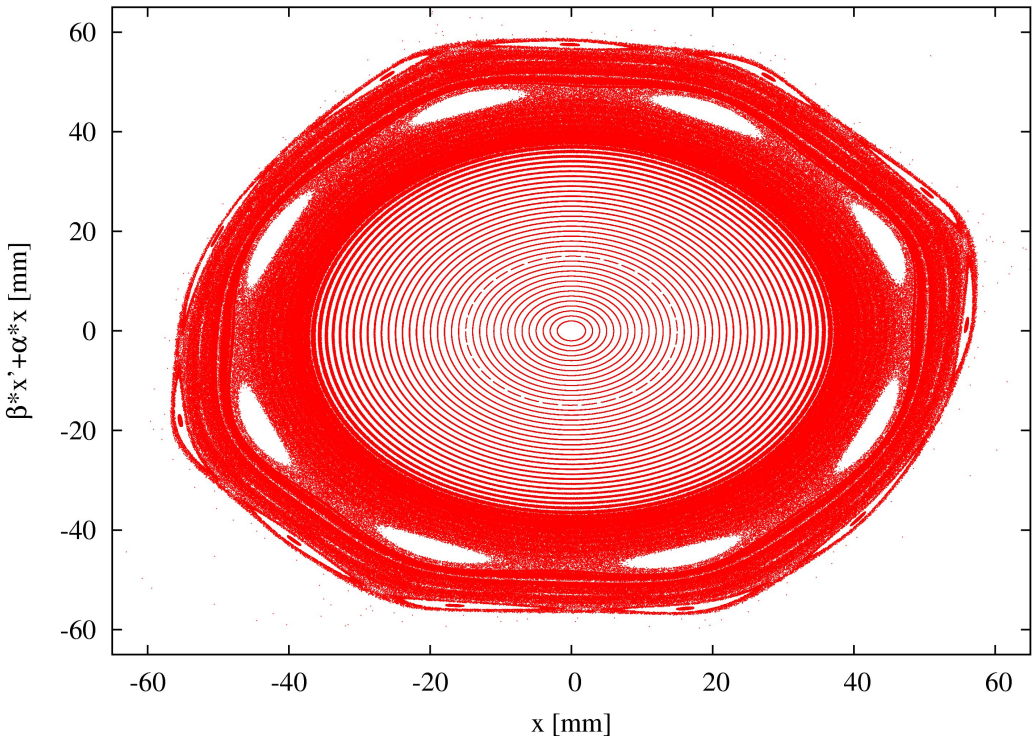

(a) Phase space with canonical variables

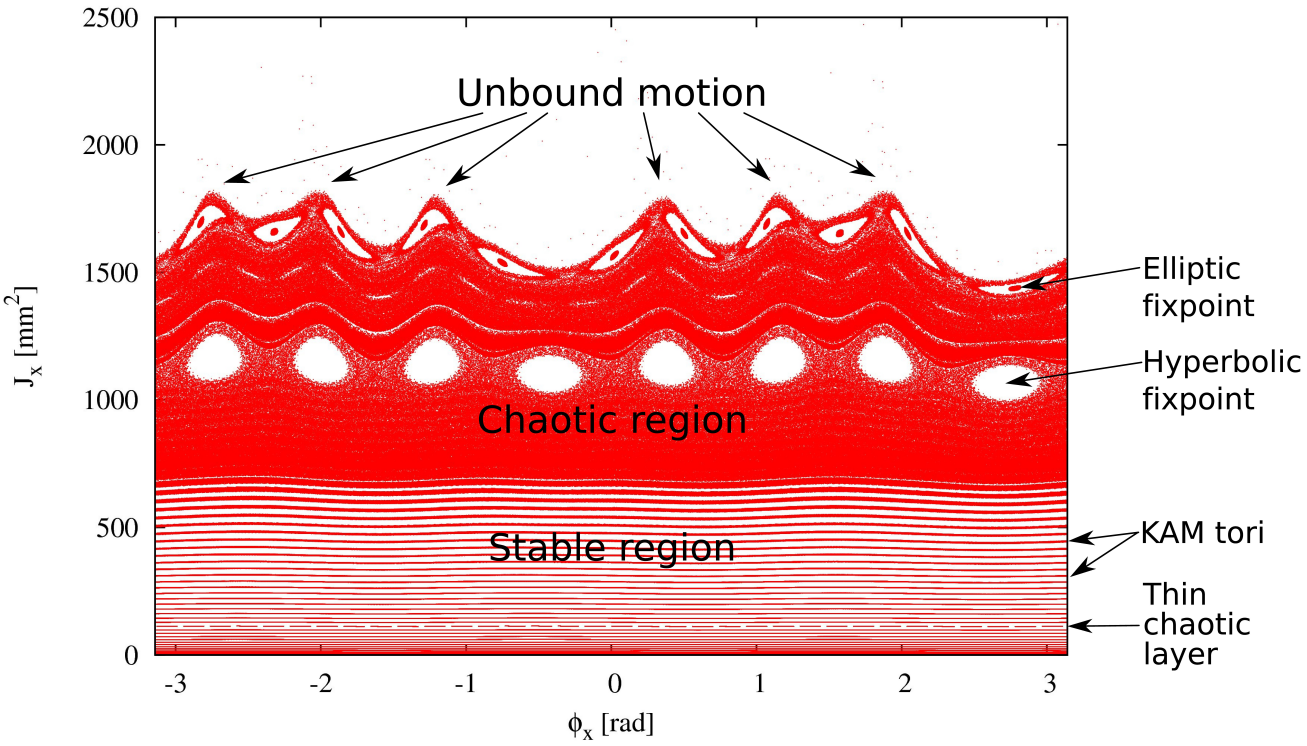

(b) Phase space with action-angle variables

Figure 5.4: Horizontal phase space plot for $\gamma_{tr} = 6.2$ lattice at design tunes. Particles with no initial momenta ($p_x = p_y = 0$), a fixed vertical coordinate of $y = 1\,mm$, and a positive x with a step size of $1\,mm$ are tracked over 50000 turns to fill the phase space. Plot a) shows the horizontal phase space where the axes are $\beta_x \cdot p_x + \alpha_x \cdot x$ versus x so that the regular KAM tori become circles and are not elliptic. Plot b) shows the same phase space but transformed to action-angle variables.

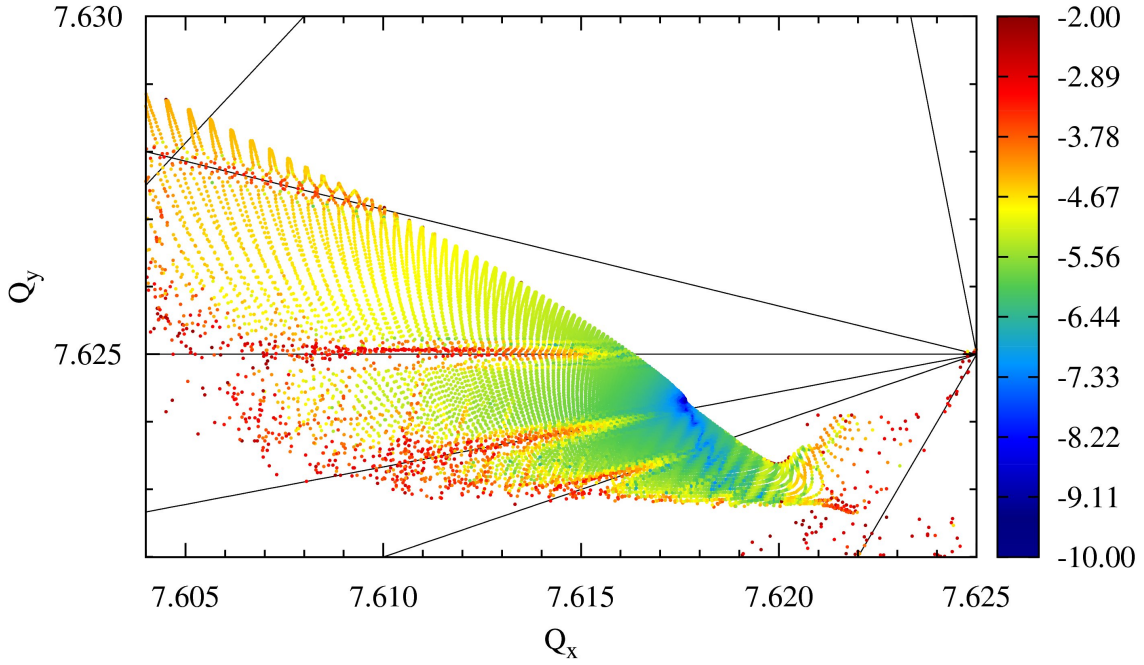

Figure 5.5: Enlarged view on main parts of frequency map of Figure 5.3a. The color scale represent the diffusion coefficient. The strong resonance lines are marked by black lines although without a triplet identification. Weaker resonances within the resonance web can also be observed.

lighter blue. The KAM tori broaden in the outer region of the stable area until the transition to the chaotic region is reached where the KAM tori break open. This happens at nearly 36 mm where the first yellow stripe appears in the dynamic aperture plot. Besides the eight hyperbolic fixpoints, there are also eleven elliptic ones further outside. Based on the knowledge about the strong 20-pole field component of the quadrupole magnets, it is extremely probable that this eleven islands reflect a eleventh order resonance driven by this field components in second order. Also the strong 12-pole field components can be observed. The outer shape of the phase space plot a) is almost hexagonal. This is shown even more clearly in plot b) where from the six "hills" particles move further away where the amplitude becomes unbound and the particles are going to be lost.

Figure 5.5 contains a closer look on the main part of Figure 5.3a and reveals the existence of weaker resonances within the resonance web.

The dynamic aperture plot demonstrates clearly the advantage of the diffusion coefficient when used together with dynamic aperture: The diffusion coefficient provide information about long-term stability even with a short-term dynamic aperture. Furthermore the resonance structure seen in the frequency map is transferred to the dynamic aperture. With the knowledge about the resonance lines in the frequency map, an identification in the dynamic aperture plot is straight forward. A mapping of those resonance lines which are easy to see in the dynamic aperture plot is listed in the caption of Figure 5.3.

The dynamic aperture plot does not show an island like the frequency map but two structures on the left and right of the "main" area with a more or less clear cut transition. These two structures contain particles on the island and on the skew quadrupole resonance. Although the dynamic aperture seems to be symmetric in most parts there are some deviations, e.g. the shapes of the structures left and right and of the upper left part. The geometrical acceptance limit is $6.63\,mm\,mrad$ (approximately $104\,\sigma$) and is marked with a white curve. The dynamic aperture is marked with a black curve. The emittance which corresponds to the dynamic aperture is $8.67\,mm\,mrad$ (roughly $136\,\sigma$).

There is an obvious deformation in the central and the upper region of the dynamic aperture plot. It is framed by dark red points reflecting chaotic behavior. The particles within this areas reside on a sextupole or a decapole resonance line. The strongest resonances which can be easily seen in the dynamic aperture plot are crossing the resonance knot at $Q_x = Q_y = 7.625$ and are marked with number 1 to 4. Stronger resonances hardly reach into the geometric acceptance limit.

This situation changes if the particles are off momentum. A momentum deviation can lead among other things to tune shifts and to changes of the closed orbit due to dispersion. For the momentum deviation a value of $3 \cdot 10^{-4}$ was chosen, which corresponds to three times the rms momentum spread of the high luminosity mode. The results can be seen in Figure 5.6.

For $\frac{\Delta p}{p} = 3 \cdot 10^{-4}$ the dynamic aperture is not reduced but increased to $9.12\,mm\,mrad$ (approximately $146\,\sigma$). Although it is bigger, the situation became worse: The resonance line $8 \cdot Q_y = 61$ reaches into the geometric acceptance. The main part of the dynamic aperture is smaller in width. The unstable areas from the structures left and right are now within the geometrical acceptance limit. Furthermore the inner area with long-term stability decreased significantly.

The relative momentum offset of $\frac{\Delta p}{p} = -3 \cdot 10^{-4}$ also shows a changed situation. The dynamic aperture is reduced $8.03\,mm\,mrad$. The structures on both sides are smaller. The resonance line $1 \cdot Q_x + 7 \cdot Q_y = 61$ moved further into the unstable area at the top of the dynamic aperture plot. The resonance lines at the sides of the dynamic aperture plot are distorted. This distortion reflects a folding of the frequency map. A folding can appear if terms of higher degrees in the Hamiltonian become dominant over the quadratic terms. Stable areas can be folded on resonance lines which then provide particles a way of fast diffusion [88]. The folding can be observed in the lower right corner of the main part in the frequency map. An view of this folding area in the frequency map is shown in Figure 5.7.

The edge of the frequency map is folded near the $2 \cdot Q_x - 10 \cdot Q_y = -61$ resonance line. Due to the folding, two different areas are crossed by a resonance line in the same tune area. Figure 5.8 shows the dynamic aperture plot 5.6b where particles are colored black if their tunes are confined within a tune range of $\Delta Q = 5 \cdot 10^{-4}$ around a specified resonance line. This has been done for the resonance lines $1 \cdot Q_x - 9 \cdot Q_y = -61$ and $2 \cdot Q_x - 10 \cdot Q_y = -61$. Plot a) does not highlight a deformation of a resonance line but clarifies that two separated areas in the dynamic aperture plot are crossed by a resonance line at the same location in tune space. The real resonance is the upper black area whereas the one below is inside the folded stable area. Plot b) shows how the resonance line $2 \cdot Q_x - 10 \cdot Q_y = -61$ is bent outwards.

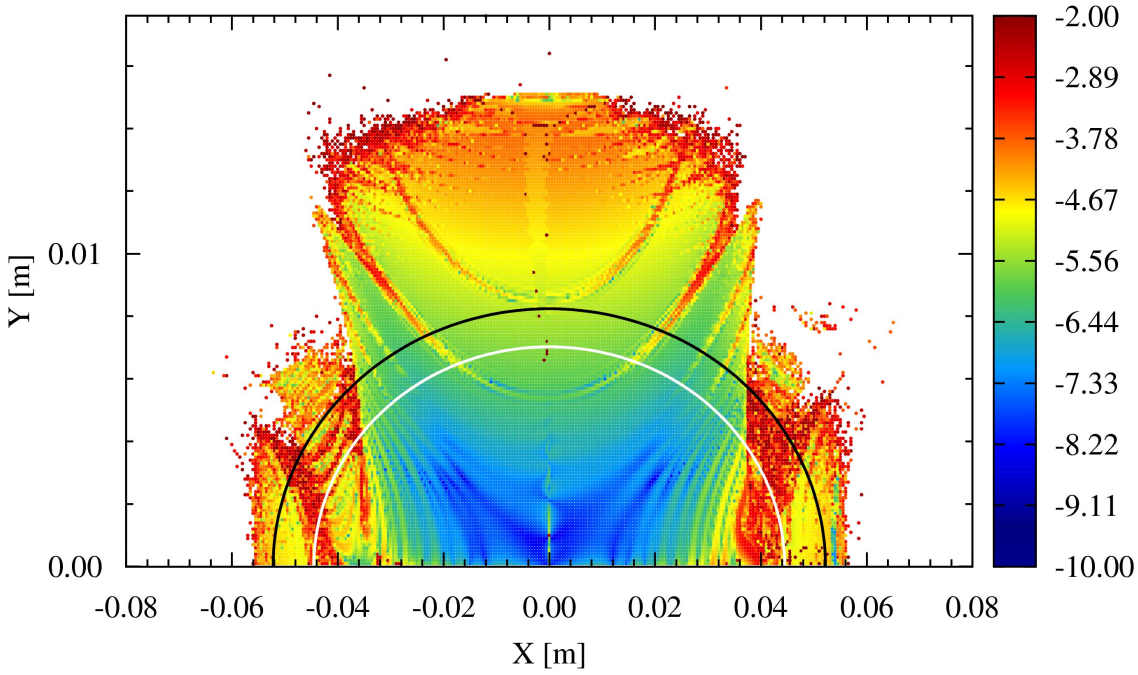

(a) Dynamic aperture for $\frac{\Delta p}{p} = 3 \cdot 10^{-4}$

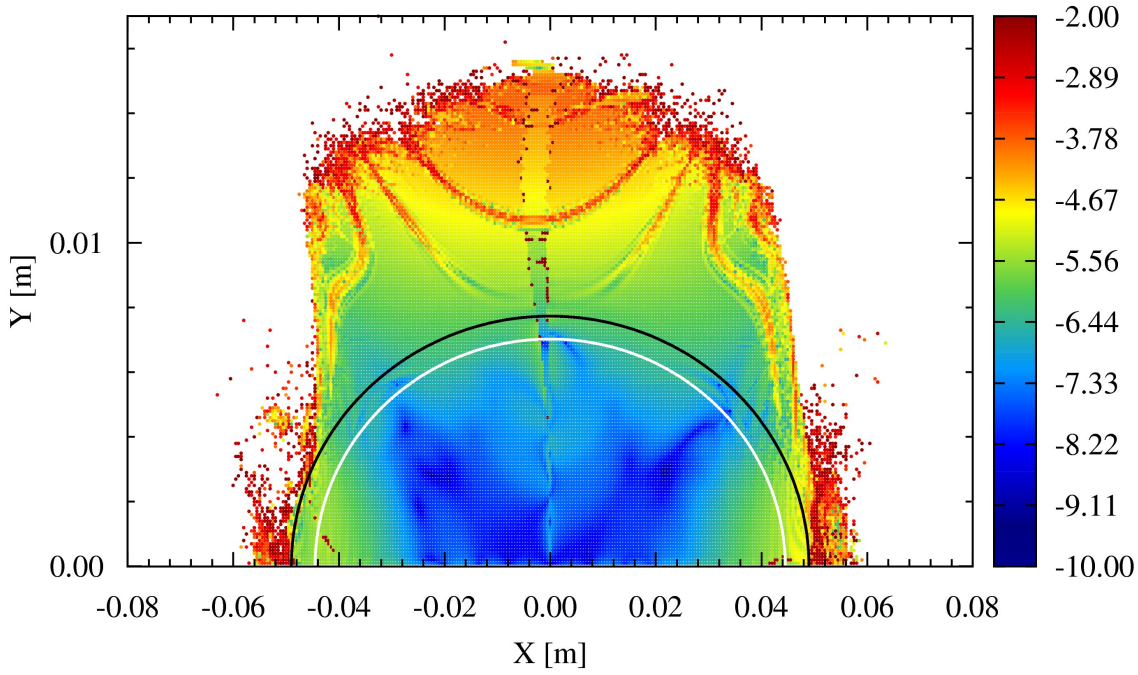

(b) Dynamic aperture for $\frac{\Delta p}{p} = -3 \cdot 10^{-4}$

Figure 5.6: Dynamic aperture for off-momentum particles with a momentum deviation of $\frac{\Delta p}{p} = \pm 3 \cdot 10^{-4}$. The color scale represent the diffusion coefficient. For a relative momentum offset of $\frac{\Delta p}{p} = -3 \cdot 10^{-4}$ some resonances are distorted. The are with long-term stability is smaller for $\frac{\Delta p}{p} = 3 \cdot 10^{-4}$. The geometric acceptance limit is given as a white line whereas the dynamic aperture as a black one.

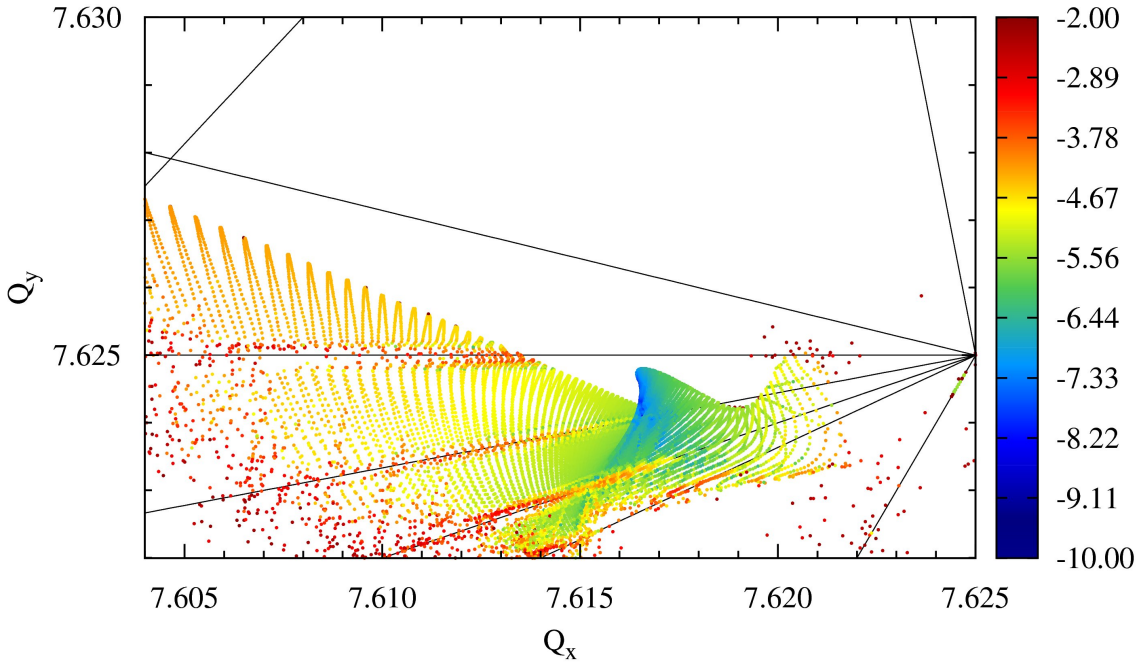

Figure 5.7: Folding of frequency map for $\frac{\Delta p}{p} = -3 \cdot 10^{-4}$. The color scale represent the diffusion coefficient.

The presented values of the dynamic aperture of the $\gamma_{tr} = 6.2$ lattice for the different momentum deviations have been determined for one specific set of field errors. The calculations have been repeated with 99 other seeds for the pseudo random number generator. The statistics for all 100 sets is given in Table 5.3.

$\Delta p/p$	$-3 \cdot 10^{-4}$	0	$3 \cdot 10^{-4}$
DA $[mm\,mrad]$	7.95 ± 0.09	8.54 ± 0.05	8.99 ± 0.04
DA $[\sigma]$	124.80 ± 1.41	134.04 ± 0.77	141.13 ± 0.63

Table 5.3: Statistics of dynamic aperture calculations with 100 different seeds

5.4.3 Optimization

There are different ways to optimize the dynamic aperture. The two main ways are a different choice of tunes and the reduction of field errors in the first place. A third possibility though is the introduction of corrector magnets. These can be used to manipulate single resonances but introduce additional non-linearities themselves and are therefore not always preferable.

Tunes As resonance driving terms depend on phase advances, a proper choice of tunes and thus also a change of phase advance can help to improve the situation. In the following, two sets of tunes are suggested: Firstly the tunes $Q_x = 7.615$, $Q_y = 7.605$ where no strong resonance is reaching inside the geometric

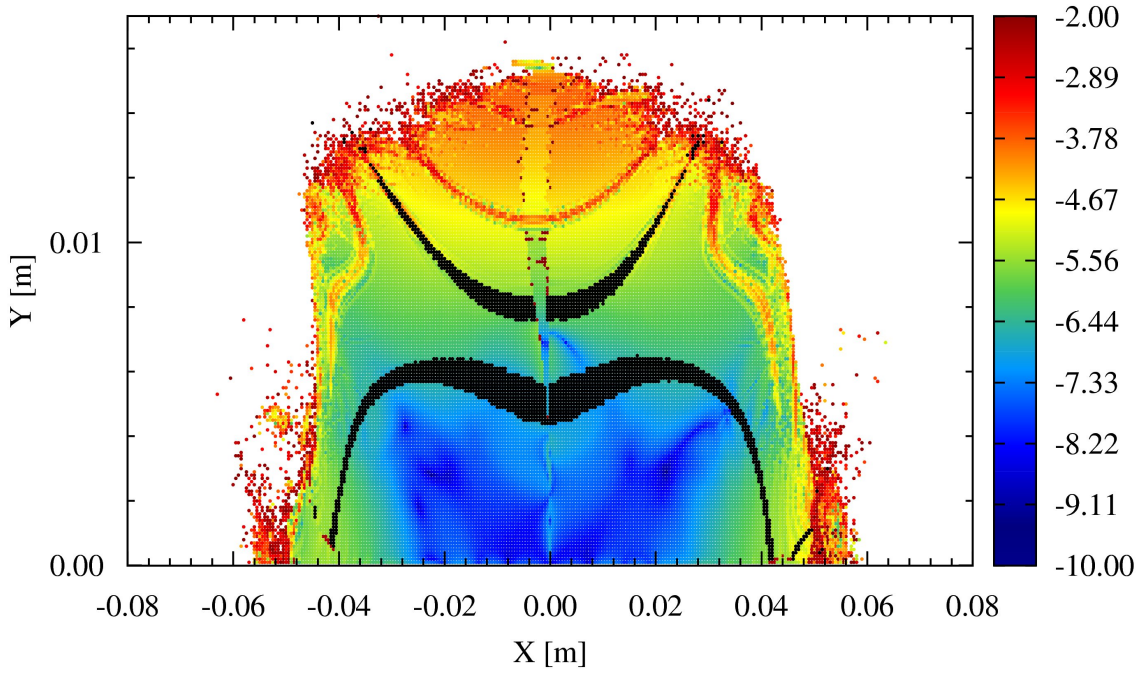

(a) $1 \cdot Q_x - 9 \cdot Q_y = -61$ (1,-9,-61)

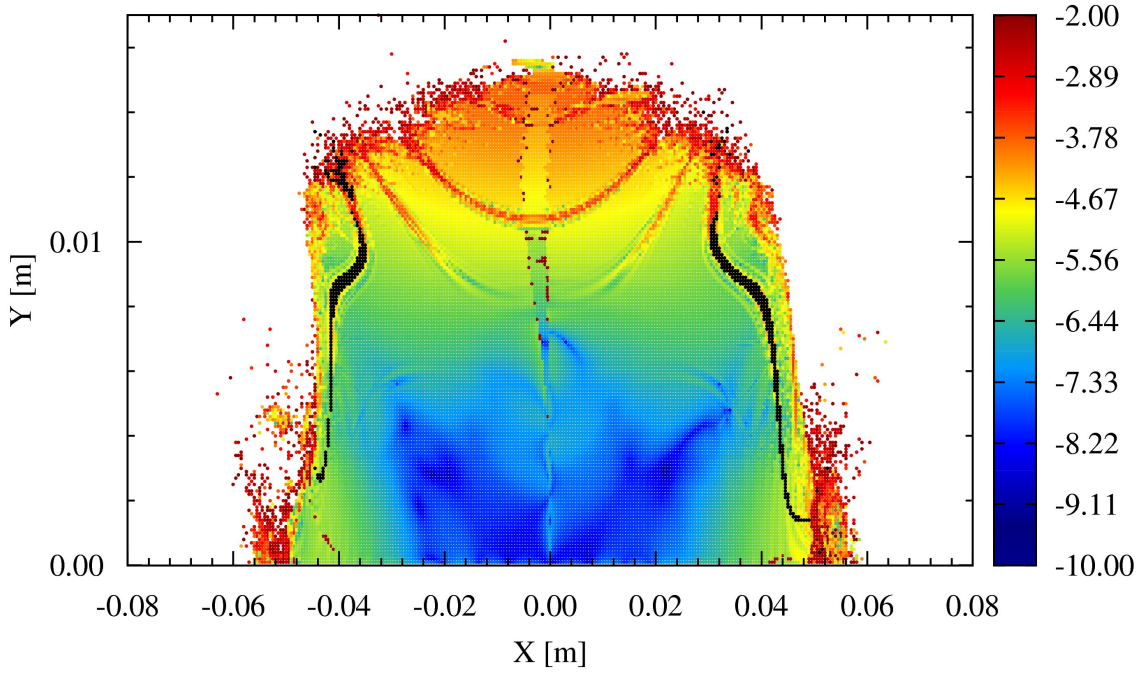

(b) $2 \cdot Q_x - 10 \cdot Q_y = -61$ (2,-10,-61)

Figure 5.8: Distortion of resonance lines in dynamic aperture plot for $\frac{\Delta p}{p} = -3 \cdot 10^{-4}$. The color scale represent the diffusion coefficient. Black colored particles mark the specified resonance with a maximum distance of $5 \cdot 10^{-4}$ from the resonance in the frequency map.

acceptance limit and secondly $Q_x = 7.568$, $Q_y = 7.582$ where the dynamic aperture is increased by more than $1\,mm\,mrad$ (more than 15σ).

Figure 5.9a shows the dynamic aperture for on-momentum particles at the different tune settings. For the first plot the tunes have been set to $Q_x = 7.615$, $Q_y = 7.605$. The dynamic aperture could be determined to be $9.70\,mm\,mrad$ (approximately $152\,\sigma$). The dynamic aperture plot shows a structure at the upper end which is split in two pieces. The naive assumption that this structure is related to an island in the frequency plot which is split in half by a resonance could be verified to be true. The dynamic aperture plot also shows that none of the stronger resonances reach inside the geometric acceptance limit. Although this is true even for off-momentum particles inside the $\frac{\Delta p}{p} = \pm 3 \cdot 10^{-4}$ boundary, the dynamic aperture differs with the momentum offset: The dynamic aperture is increased slightly to $9.88\,mm\,mrad$ for $\frac{\Delta p}{p} = 3 \cdot 10^{-4}$ and decreased by more than $0.5\,mm\,mrad$ to $9.07\,mm\,mrad$ for a momentum deviation of $\frac{\Delta p}{p} = -3 \cdot 10^{-4}$.

Dynamic aperture calculations have also been performed for the other tune setting at $Q_x = 7.568$, $Q_y = 7.582$. The dynamic aperture compared to the previous tunes is increased by 10.7% to $10.74\,mm\,mrad$ (approximately $169\,sigma$). For off-momentum particles, the dynamic aperture increases to $11.01\,mm\,mrad$ ($\frac{\Delta p}{p} = 3 \cdot 10^{-4}$) and $11.00\,mm\,mrad$ ($\frac{\Delta p}{p} = -3 \cdot 10^{-4}$). The dynamic aperture and frequency map for on momentum particles are shown in Figure 5.9b.

Field errors Investigations have shown that the field errors of the quadrupole magnet are dominant. The 12- and 20-pole field components of the quadrupole magnets are by far the strongest (see Table 5.2). In the following a series of reductions of both field errors has been performed. Since the quadrupole design has not been finished yet, this investigation was performed and the results will be incorporated in an optimized quadrupole design.

Already the tune scan reflected the strong 12- and 20-pole field components of the quadrupole magnet design. A reduction of both field components will help to increase the dynamic aperture on one hand and the area with long-term stability in the inner region on the other. The dynamic aperture has been calculated for reduced strengths of the 12- and 20-pole field components. The results of these reductions are shown in Table 5.4.

There are some values reflecting a smaller dynamic aperture even with reduced field components, e.g. $13.35\,mm\,mrad$ for $b_5 = 12.5 \cdot 10^{-4}$ and $b_9 = 5.0 \cdot 10^{-4}$ compared to $14.66\,mm\,mrad$ for $b_5 = 25.0 \cdot 10^{-4}$. This can happen due to chaotic behavior at the outer region. Furthermore, a compensation of certain driving terms can occur and disappear since many driving terms may contribute to a single resonance.

Nevertheless, a clear tendency can be observed: It is obvious that the 20-pole field component restricts the dynamic aperture much more than the 12-pole field component. As one can expect if one field component is dominant, the reduction of the 12-pole field component lead to a smaller increase of the dynamic aperture. The size of the dynamic aperture is heading towards $15\,mm\,mrad$ with the reduction of the 20-pole field component. In order to further increase the dynamic aperture a simultaneous reduction of both multipole components has to be performed. Based

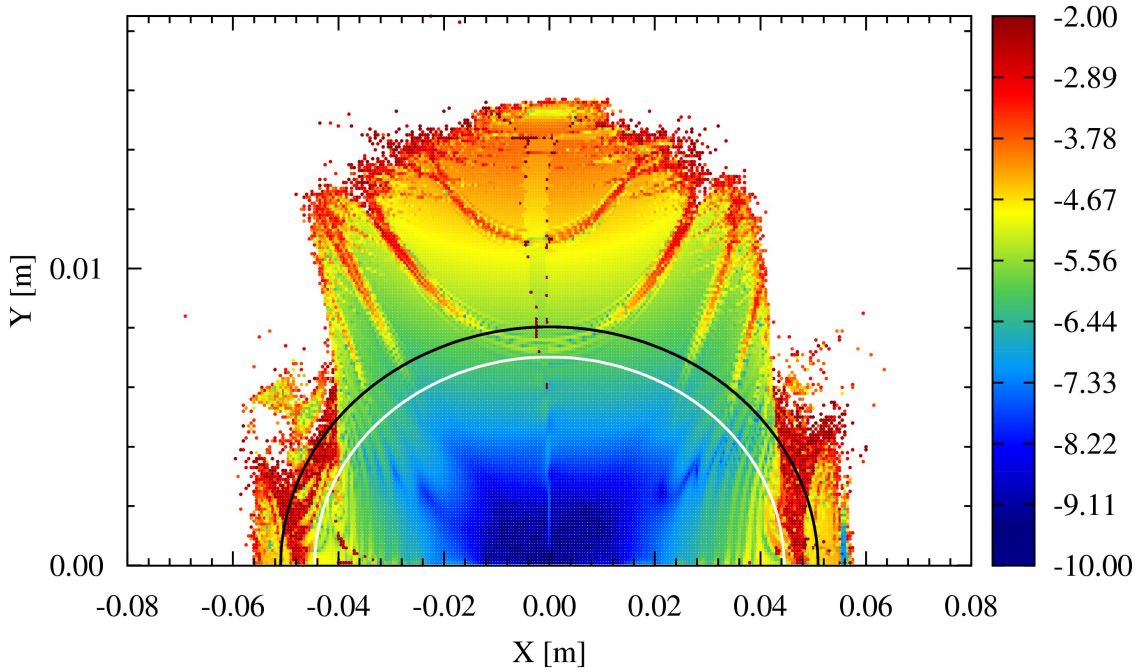

(a) Dynamic aperture for tunes $Q_x = 7.615$, $Q_y = 7.605$

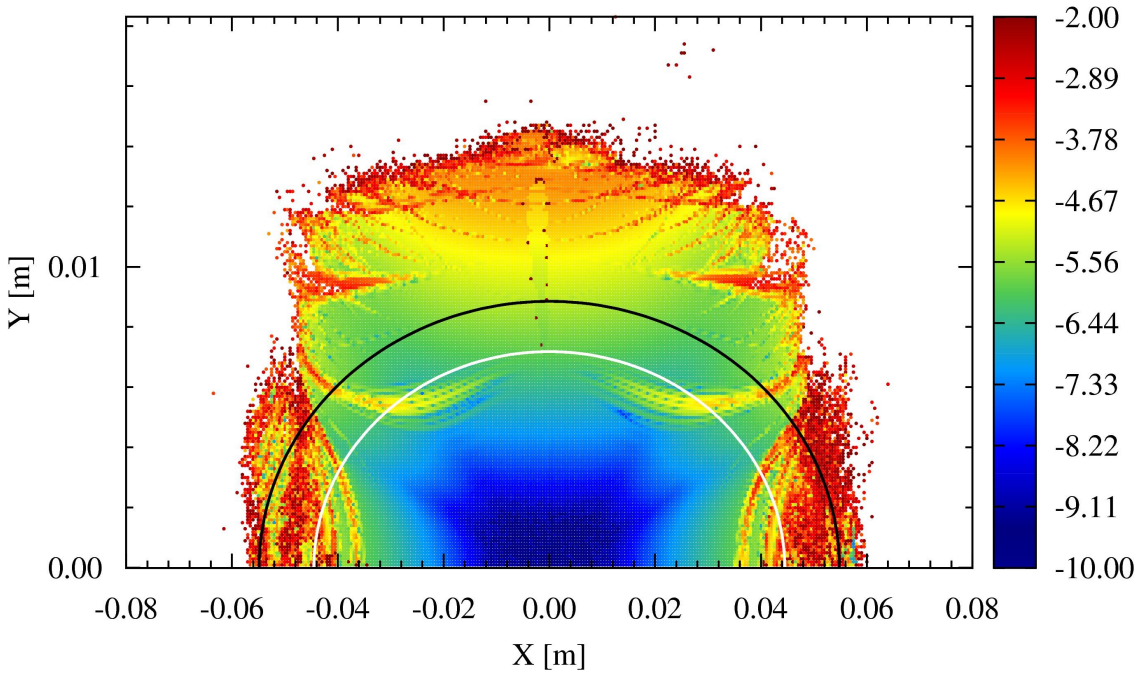

(b) Dynamic aperture for tunes $Q_x = 7.568$, $Q_y = 7.582$

Figure 5.9: Dynamic aperture for different tune settings a) $Q_x = 7.615$, $Q_y = 7.605$ and b) $Q_x = 7.568, 7.582$. The color scale represent the diffusion coefficient. The geometric acceptance limit is given as a white line whereas the dynamic aperture as a black one.

20-pole \ 12-pole	25.0	12.5	10.0	7.5	5.0
100.0	8.42	8.91	9.06	9.15	9.32
50.0	9.68	10.17	10.30	10.46	10.74
25.0	10.78	11.12	11.29	11.58	12.22
12.5	12.02	12.13	12.57	12.89	13.36
10.0	12.58	13.01	12.94	13.38	13.88
7.5	13.86	13.23	13.19	13.47	14.19
5.0	14.66	13.35	13.90	13.70	14.71

Table 5.4: Dynamic aperture calculated with 12- and 20-pole quadrupole field components at $15\,GeV/c$. The relative field errors include the 10% increase and are given in units of 10^{-4}. The dynamic aperture is given in $mm\,mrad$.

on the reduction of the dipole magnets sextupole field component, a reduction of both strong field components of the quadrupole magnets by roughly a factor five appears to be reasonable. The 20-pole field component is set to $b_9 = 25 \cdot 10^{-4}$ while reducing the 12-pole field component to $b_5 = 10 \cdot 10^{-4}$. The resulting dynamic aperture for the design tunes is shown in Figure 5.10.

The dynamic aperture of $11.29\,mm\,mrad$ corresponds to approximately $183\,\sigma$. This is an increase by 30%. As the dynamic aperture plot shows, the area within the geometric acceptance limit is mostly colored blue with only a few green parts which means that there are no strong resonances reaching inside and the area with long-term stability increased. The observed structure in the center of the plot is mainly created by the skew quadrupole difference resonance $Q_x - Q_y = 0$.

The frequency map with reduced multipoles is more compact and does not show the subtle web of resonances as the frequency map for full field errors did. Nevertheless the stronger resonances crossing the frequency map are still the same and easy to identify.

Combination of different tunes and reduced field components Better results can be achieved with the combination of both investigated optimization methods. Changing the tune settings while reducing the 12- and 20-pole field components can further improve the dynamic aperture. Taking again the same reduced field errors as before and setting the tunes to $Q_x = 7.568$, $Q_y = 7.582$, the dynamic aperture rises even to $15.72\,mm\,mrad$ with none of the resonances reaching inside the geometric acceptance limit. The dynamic aperture is different for off-momentum particles: An increase to $15.86\,mm\,mrad$ for $\frac{\Delta p}{p} = 3 \cdot 10^{-4}$ and a decrease to $13.84\,mm\,mrad$ for $\frac{\Delta p}{p} = -3 \cdot 10^{-4}$. This means that the dynamic aperture is more than twice as large as the geometric acceptance limit even for off-momentum particles.

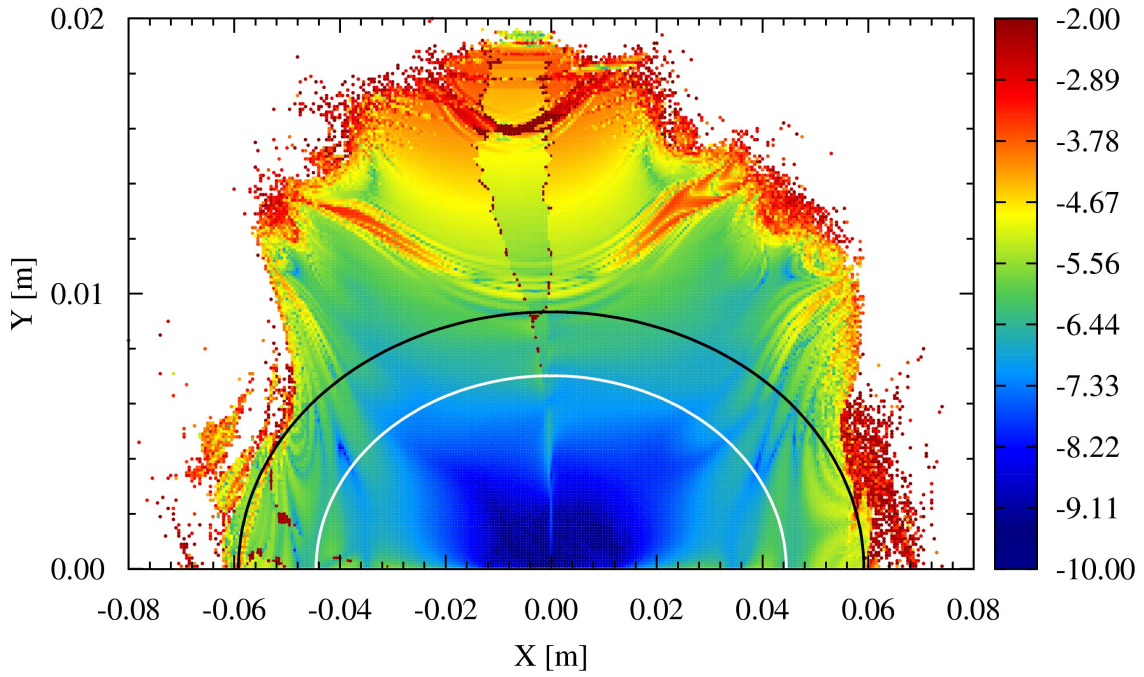

Figure 5.10: Dynamic aperture of $\gamma_{tr} = 6.2$ lattice with reduced quadrupole errors at design tune for on-momentum particles. The color scale represent the diffusion coefficient. The relative field errors of the 12- and 20-pole are reduced to $b_5 = 10{\cdot}10^{-4}$ and $b_9 = 25 \cdot 10^{-4}$. The geometric acceptance limit is given as a white line whereas the dynamic aperture as a black one.

5.5 The $\gamma_{tr} = 13.3$ lattice

The other defined ion-optical setting for the PANDA experiment is the $\gamma_{tr} = 13.3$ lattice. It will be used for the low energy region of the HESR in order to optimize the stochastic cooling. The following calculations assume an energy of $1.5\,GeV/c$. The geometric emittance is $\varepsilon = 0.637\,mm\,mrad$ ($\varepsilon_{norm} = 1\,mm\,mrad$). The field errors which are taken into account are errors of the dipole magnet at $0.17\,T$ main field and of the quadrupole magnet at gradient of roughly $3.6\,T/m$ ($200\,A$). The design tune are chosen to be $Q_x = 7.614$, $Q_y = 7.615$.

5.5.1 Tune scans

Also for the $\gamma_{tr} = 13.3$ lattice a tune scan has been performed. It is shown in Figure 5.11.

Compared to the $\gamma_{tr} = 6.2$ lattice, the $\gamma_{tr} = 13.3$ lattice is even more sensitive to mismatches which is demonstrated by an increase of the black area. There is a general decrease of dynamic aperture when given in terms of 1σ-emittance. This is mainly due to the fact that the 1σ-emittance is by one order of magnitude larger caused by the lower energy. Similar resonances can been observed as for the $\gamma_{tr} = 6.2$ lattice tune scan. Although sextupole resonances are strong and the sextupoles for the chromaticity does not perform as good as for the $\gamma_{tr} = 6.2$ lattice, these sextupole resonance lines are most likely mainly driven by the 12-pole field components. Since

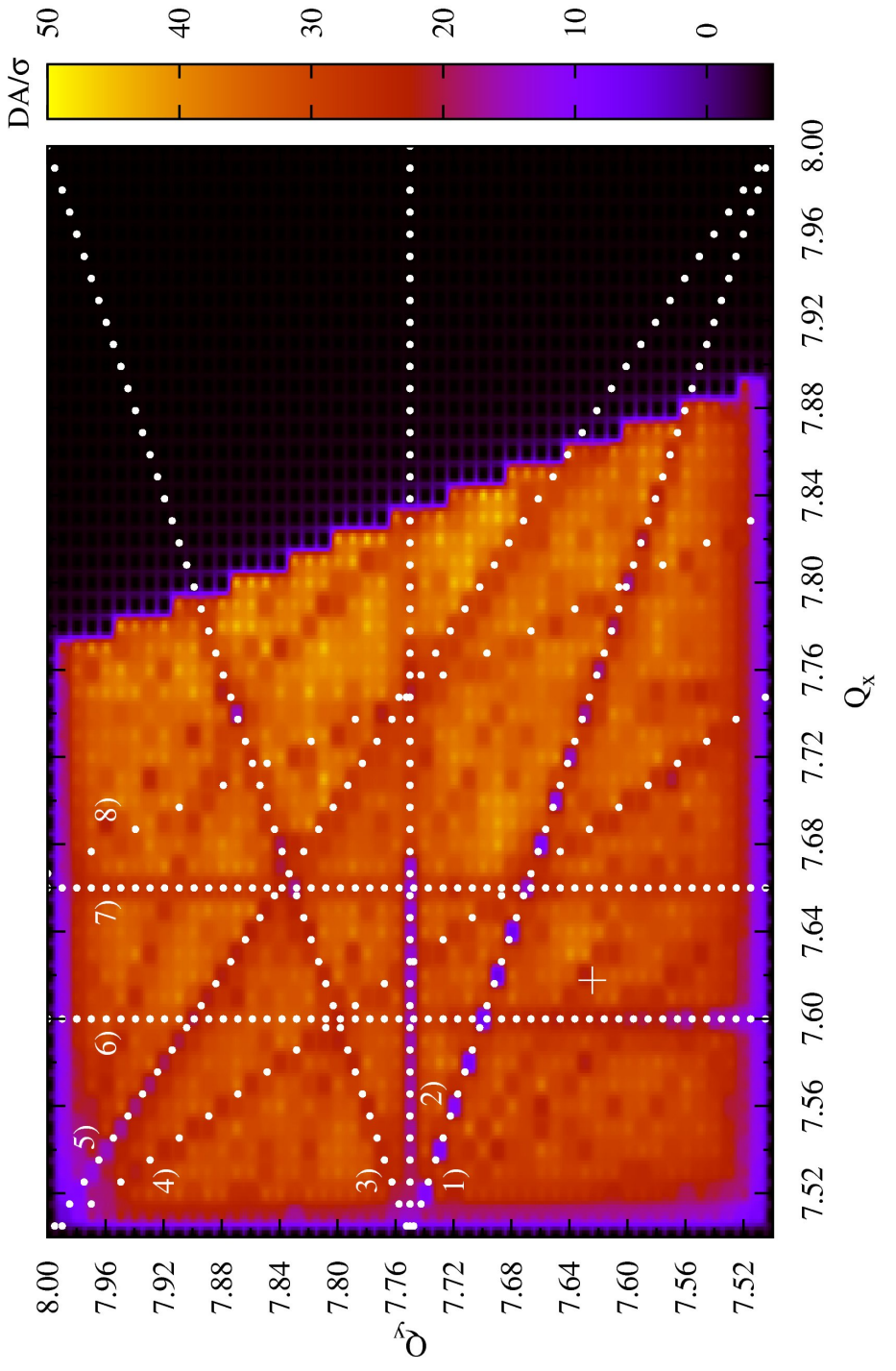

Figure 5.11: Tune scan for $\gamma_{tr} = 13.3$ lattice and 1000 turns. The color scale is given in DA/σ. The negative value (colored black) is not realistic but represent an unstable linear lattice and is used to separate unstable tunes of the linear modell from zero DA. The strongest resonance lines have been identified and marked: 1) Sextupole $Q_x + 2 \cdot Q_y = 23$; 2) Octupole $4 \cdot Q_y = 31$; 3) Sextupole $Q_x - 2 \cdot Q_y = -8$; 4) Skew Sextupole $2 \cdot Q_x + Q_y = 23$; 5) Octupole $2 \cdot Q_x + 2 \cdot Q_y = 31$; 6) Decapole $5 \cdot Q_x = 38$; 7) Sextupole $3 \cdot Q_x = 23$; 8) Skew Octupole $3 \cdot Q_x + Q_y = 31$. The cross indicates the design tunes.

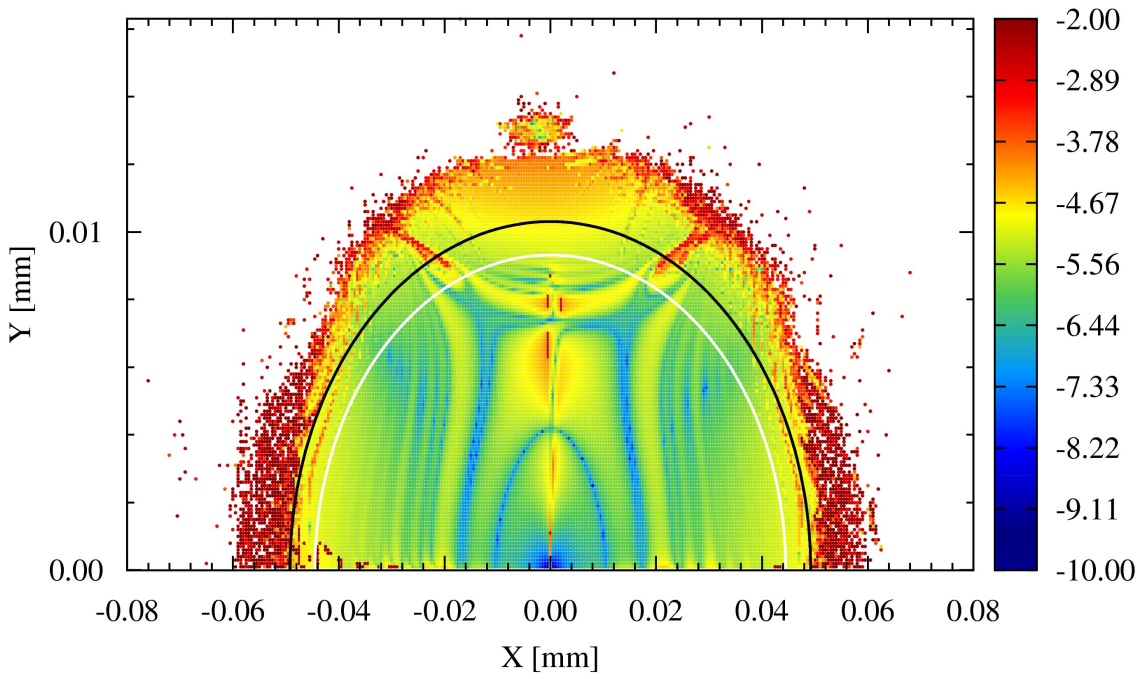

Figure 5.12: Dynamic aperture for on-momentum particles at design tune. The color scale represent the diffusion coefficient. Only a very small area with long-term stability is observed. The geometric acceptance limit is given as a white line whereas the dynamic aperture as a black one.

it is a simulation, it is easy to exclude certain multipoles. Without the chromatic sextupoles, the resonance lines are nearly unchanged which is a strong indication that the sextupole resonance lines are not mainly driven by the sextupoles. The main contribution to these resonance lines also come from higher-order multipoles like 12- and 20-pole field components:

All sextupole resonance lines and the skew sextupole resonance line can be driven by the 12-pole field component in first order. The 20-pole field component can e.g. drive the decapole resonance in first order. All upright and skew octupole resonance lines can be 16-pole resonance lines driven by 12- and 20-pole field components.

5.5.2 Design tunes

The design tunes of the $\gamma_{tr} = 13.3$ lattice are $Q_x = 7.614$, $Q_y = 7.615$ which means they are even closer to the difference resonance line $Q_x - Q_y = 0$. The tunes being so close, it is to expect a relatively small dynamic aperture and what is even more important smaller long term stability. The dynamic aperture can be seen in Figure 5.12.

From the dynamic aperture plot alone it should be clear that the design tunes have to be chosen differently when it comes to non-linear beam dynamics. The particles with long term stability are restricted to an area which is smaller than $\frac{1}{4}\sigma$. The dynamic aperture is $16.78\,mm\,mrad$ for on-momentum particles. But it is increased for particles with an momentum deviation. The biggest increase with

a value of $17.95\,mm\,mrad$ is for $\frac{\Delta p}{p} = -3 \cdot 10^{-4}$. A general growth of the dynamic aperture can be observed and can mainly be explained with the different ion-optical setting where e.g. the field errors are smaller. Furthermore the maximum beta functions are smaller by a factor two: $150\,m$ compared to the $300\,m$ of the $\gamma_{tr} = 6.2$ lattice. The maximum beta functions in x and y have similar values. This is reflected by the fact that the dynamic aperture is not longer dominated by the horizontal limit only. The vertical limit of the dynamic aperture is close to the edge of the stable area.

The frequency map demonstrates how close the design tunes are to the difference resonance. There is also a folding for on-momentum particles in the frequency map. The analysis of the phase space provide similar information as for the $\gamma_{tr} = 6.2$ lattice.

Since different tunes have to be chosen anyway, the dynamic aperture plot is not shown for off-momentum particles.

5.5.3 Optimization

The two main ways of optimization are covered: The decrease of field errors and the different choice of tunes.

Tunes From the tune scan an area of large dynamic aperture and as close as possible to the design tune has been picked. This area is closely located to $Q_x = 7.630$, $Q_y = 7.640$. One the best results have been found at $Q_x = 7.637$, $Q_y = 7.647$. The dynamic aperture for on-momentum particles is $23.92\,mm\,mrad$ and can be seen in Figure 5.13. This is an increase by 45%. The increase for off-momentum particles is smaller and ranges from 12% for $\frac{\Delta p}{p} = 3 \cdot 10^{-4}$ to 19% for $\frac{\Delta p}{p} = -3 \cdot 10^{-4}$. The most important change is the increase of the area of long term stability which covers $3-4\sigma$. Also here the calculation have been repeated with different seeds. The results are shown in Table 5.5.

$\Delta p/p$	$-3 \cdot 10^{-4}$	0	$3 \cdot 10^{-4}$
DA $[mm\,mrad]$	21.43 ± 0.08	23.92 ± 0.07	18.92 ± 0.10
DA $[\sigma]$	33.65 ± 0.13	37.55 ± 0.11	29.70 ± 0.16

Table 5.5: Statistics of dynamic aperture calculations for tunes $Q_x = 7.637$, $Q_y = 7.647$ with 100 different seeds.

Field errors The field errors at the lower energy limit are a bit more relaxed since the 12-pole field component of the quadrupole magnets is roughly a factor five smaller. Even the 20-pole field components are with $b_9 = 92.03 \cdot 10^{-4}$ compared to the $b_9 = 118.54 \cdot 10^{-4}$ reduced by more than 20%. Nevertheless, the 20-pole field components is still absolutely dominant (see Table 5.6) and has to be reduced in order to increase the dynamic aperture and, what is probably more important, the area of long term stability. Since the design tunes had to be changed anyway, this investigation was carried out for the new tunes at $Q_x = 7.637$, $Q_y = 7.647$.

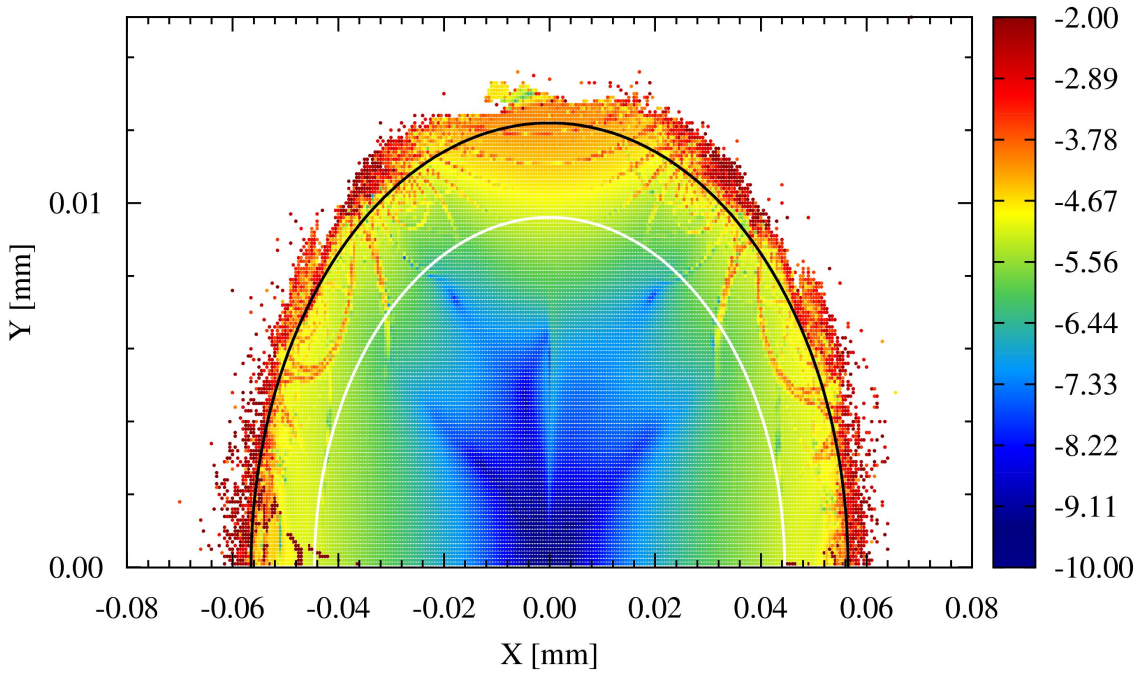

Figure 5.13: Dynamic aperture of the $\gamma_{tr} = 13.3$ lattice for optimized tunes $Q_x = 7.637$, $Q_y = 7.647$. The color scale represent the diffusion coefficient. The geometric acceptance limit is given as a white line whereas the dynamic aperture as a black one.

12-pole \ 20-pole	50.0	25.0	12.5	10.0	7.5	5.0
10.0	26.13	30.27	33.35	33.96	34.25	34.84
7.5	26.47	30.78	34.26	34.88	35.08	35.57
5.0	26.88	31.52	35.15	35.80	35.99	36.19

Table 5.6: Independent reductions of 12- and 20-pole quadrupole field components at $1.5\,GeV/c$. The relative field errors include the 10% increase and are given in units of 10^{-4}.

A reduction by a factor five appears to be reasonable also at $1.5\,GeV/c$. The 20-pole field component is set to $b_9 = 20 \cdot 10^{-4}$. The resulting dynamic aperture for on-momentum particles has a size of $31.67\,mm\,mrad$ which is an overall increase of 89%. The dynamic aperture is up to 10.4% smaller for off-momentum particles, namely $27.77\,mm\,mrad$ for $\frac{\Delta p}{p} = 3 \cdot 10^{-4}$ and $26.31\,mm\,mrad$ for $\frac{\Delta p}{p} = -3 \cdot 10^{-4}$.

5.6 Multipole correction

The driving terms provide a way to access resonances. Manipulating the driving terms can be useful to correct certain resonances which was done e.g. at RHIC to preserve polarization [89]. This correction was performed using chromatic sextupole families. In contract to RHIC, there are not enough families possible in the HESR to manipulate the sextupole first order resonance driving terms independently. Fur-

thermore, the splitting into four families was based on dynamic aperture and not on resonance driving terms directly. This means that the phase advances do not fit to correct a specific resonance driving term. Stating this, there is only one way to access the sextupole first order driving terms: The introduction of geometric sextupoles in the straights. Such sextupole magnets can be used independently of the chromatic ones because they do not contribute to chromaticity correction. There is one drawback though: While changing the driving terms in first order, they also contribute in higher orders and introduce additional non-linearities themselves.

Nevertheless, the inclusion of geometric sextupole magnets has been investigated. The results are that the additional non-linearities are much worse than the gain for the sextupole resonances. Furthermore the gain itself is small since the chromaticity correction scheme performs well enough to make sextupole resonances a minor problem. The main problem concerning resonances is related to the 12- and 20-pole field components of the quadrupole magnets. That means that the investigation of a multipole correction scheme has to be delayed until the design of the quadrupole magnet has been finished.

5.7 Discussion of the results

The reduction of the sextupole field component of the dipole magnets made a chromaticity correction feasible. The developed chromaticity correction scheme does hardly affect the dynamic aperture of the $\gamma_{tr} = 6.2$ lattice. The $\gamma_{tr} = 13.3$ lattice is stronger influenced by the sextupole magnets. The beta functions and phase advances between sextupole magnets do not fit nearly as good as for the $\gamma_{tr} = 6.2$ lattice and compensating sextupole magnet pairs cannot be found easily. Even though, with the grouping into four families the dynamic aperture restrictions by the sextupole magnets can be decreased.

Nevertheless, the main restrictions of the dynamic aperture is due to field errors of the quadrupole magnets. Thus an investigation was carried out concerning the improvement of the dynamic aperture. Both investigated ion-optical settings, the $\gamma_{tr} = 6.2$ and the $\gamma_{tr} = 13.3$ lattice, provide at least in the short term regime a dynamic aperture which is larger than the geometrical acceptance limit. The acceptance limit of the dynamic aperture itself depends on the beta functions and the dispersion. While for the $\gamma_{tr} = 6.2$ lattice the dynamic aperture is limited horizontally, it is almost equal for both transverse directions for the $\gamma_{tr} = 13.3$ lattice.

The change of tunes and the reduction of field errors were successfully applied and lead to an overall increase of the dynamic aperture of roughly a factor two. Based on the reduction of the sextupole field component of the dipole magnets, a reduction of the dominating field errors (the 12- and 20-pole field components) of a factor five appeared to be reasonable. Further improvements of the field errors lead to an additional increase of the dynamic aperture. For the $\gamma_{tr} = 13.3$ lattice a different choice of tunes is inevitable since the design tunes provide an area of long

term stability which is less than $\frac{1}{4}\sigma$ which is not sufficiently large. Without any optimization of field errors, this area could be increased to $3-4\sigma$ just by choosing a different tune setting.

Overall it can be stated that the area with long term stability is after correction large enough to accept necessary beam width including the specified orbit deviations of $5\,mm$. This implies that the closed orbit should be corrected all the time even during acceleration.

Chapter 6

Summary and outlook

Simulations of the closed orbit have shown that an uncorrected closed orbit in the HESR is larger than the geometric acceptance limited by the beam pipe. Therefore, a closed orbit correction scheme consisting of beam position monitors and closed orbit correction dipole magnets has been developed and verified by numerical simulations. It fulfills the requirements of a resulting closed orbit of $5\,mm$ realized with a maximum correction strength of $1\,mrad$. Local closed orbit bumps e.g. at the target and injection has been checked to be feasible.

Furthermore, the effect of the electron cooler's toroid magnets have been investigated and the deflection of the circulating antiproton beam caused by the toroid magnets calculated. The location of compensation dipole magnets and their necessary strength have been determined.

The orbit correction method using the orbit response matrix could be verified at the Cooler Synchrotron COSY. The measurement showed good agreement with the ion-optical model of COSY. Although the closed orbit correction at COSY was not as successful as it has to be for the HESR, the limiting factors have been identified and can be overcome by a different setup of the electron cooler compensation bump.

A chromaticity correction scheme for the HESR has been developed and optimized using dynamic aperture methods. A splitting of the two sextupole families into four families (two horizontal and two vertical) leads to further improvement by increasing the dynamic aperture. In this context it became obvious that the sextupole field component of the dipole magnet design in the upper field range affected the chromaticity strongly. The chromaticities became too large to be correctable. Therefore, the dipole magnet design was optimized and a reduction by roughly a factor eight has been achieved by a modification of the iron yoke.

With the inclusion of field errors of dipole and quadrupole magnets, betatron resonances have been simulated. Since the quadrupole magnet design is not finished yet, possible multipole optimizations has been investigated. Especially the 12- and 20-pole field components have been identified as a major limitation. Furthermore, tune scans revealed areas with large dynamic aperture and presented a global overview of the strongest resonances in the resonance web. The frequency map analysis together with the diffusion coefficient provided additional information about long-term stability and the local resonance structure. This information has been used to improve the tune settings of the HESR. The dynamic aperture was

increased by roughly a factor two with reasonable reductions of field errors and different choices of tunes. In order to prevent beam loss due to resonances during injection, acceleration, and storage, closed orbit corrections have to be applied at all times to keep the beam within the specified limits.

In future, dynamic aperture calculations and frequency map analysis for COSY will provide insight into the non-linear motion and the resonance structure. A related optimization strategy could also improve experimental conditions e.g. for spin-filter experiments.

The investigation of a multipole correction scheme for the HESR has to be carried out after the quadrupole magnet design is finished. Latest developments and improvements in the field of supercomputing offer the opportunity to investigate long-term stability while overcoming necessary restrictions of dynamic aperture calculations which had to be applied for this thesis. The long term dynamic aperture and its logarithmic dependence on the number of turns should be investigated for HESR especially if other effects which act on longer time scales (e.g. space charge) are taken into account including the non-linear forces created by the electron beam of the electron cooler.

List of Tables

List of Figures

Bibliography

[1] *An International Accelerator Facility for Beams of Ions and Antiprotons - Conceptional Design Report*, , 2001
URL `http://www.gsi.de/GSI-Future/cdr/`

[2] *An International Accelerator Facility for Beams of Ions and Antiprotons - Baseline Technical Report*, , Sep 2006
URL `http://www.gsi.de/fair/reports/btr.html`

[3] R. Maier et al., *HESR (normal conducting version with dispersion suppressor)*, 3.1, HESR Consortium, 2008

[4] PANDA collaboration, *Physics Performance Report for: PANDA, Strong Interactions Studies with Antiprotons*, Technical Report, 2009, arXiv:0903.3905v1 [hep-ex]

[5] K. Kilian et al., *Cooler Synchrotron COSY-Jülich*, 1990, user guide

[6] R. Maier et al., *Cooler Synchrotron COSY*, Nuclear Physics A, 626:pp. 395c – 403c, 1997

[7] H. Wiedemann, *Particle Accelerator Physics I + II*, Springer, 2003, ISBN 3–540–00672–9

[8] R. Gupta et al., *RHIC IR quadrupoles and field quality state of the art in superconducting accerlerator magnets*, in *Proceedings of the 1999 Particle Accelerator Conference PAC99*, pp. 185–187, New York, 1999

[9] M. Livingston and J. Blewett, *Particle accelerators*, McGraw-Hill, New York, 1962

[10] F. Iselin, *The MAD Program Physical Methods Manual*, 1994
URL `http://cern.ch/Hans.Grote/mad/mad8/doc/phys_guide.ps.gz`

[11] M. Sands, *The Head-Tail Effect*, SLAC-TN-69-8 and 10, SLAC National Accelerator Laboratory, Menlo Park

[12] S. Guiducci, *Chromaticity*, in *CERN Accelerator School*, CERN 94-01, Jyväskylä, 1994

[13] R. Talman, *Single particle motion*, in *Frontiers of Particle Beams; Observation, Diagnosis and Correction*, volume 343 of *Lecture Notes in Physics*, Springer, New York, 1988

[14] H. Koziol, *Beam diagnostics for accelerators*, in *CERN Accelerator School 94-01*, volume 2, pp. 565–600, 1994

[15] G. H. Hoffstaetter et al., *Orbit-Response Matrix Analysis at HERA*, in *Proceedings of the 2002 European Particle Accelerator Conference EPAC02*, pp. 407–409, Paris, 2002

[16] D. Reistad, The Svedberg Laboratory, *private communication*

[17] K. Erdmann and M. J. Wildon, *Introduction to Lie Algebras*, Springer, 2006

[18] L. Laslett, *On Intensity Limitations Imposed by Transverse Space-Charge Effects in Circular Accelerators*, BNL Report, BNL-7534, 1963, reprint in LBL PUB-616 (1987)

[19] A. Luccio and N. D'Imperio, *Simbad User's Manual Version 1.36*, C-A/AP/222, Brookhaven National Labaratory, Upton, NY, 2005

[20] J. Galambos et al., *ORBIT - A Ring Injection Code with Space Charge*, in *Proceedings of the 1999 Particle Accelerator Conference PAC99*, New York, 1999

[21] H. Grote and F. Iselin, *The MAD (Methodical Accelerator Design) program Version 8.19, User's Rerence Manual*, CERN/SL/90-13, Geneva, 1996

[22] *MAD-X, Methodical Accelerator Design*
URL `http://mad.web.cern.ch/mad/`

[23] J.-P. Koutchouk, *The LHC Dynamic Aperture*, in *Proceedings of the 1999 Particle Accelerator Conference PAC99*, pp. 372–374, New York, 1999

[24] J. Bengtsson, *The Sextupole Scheme for the Swiss Light Source (SLS): An Analytic Approach*, SLS Note 9/97, Paul Scherer Institut (PSI), Villingen, 1997

[25] L. Nadolski and J. Laskar, *Review of single particle dynamics for third generation light sources through frequency map analysis*, Phys. Rev. ST Accel. Beams, 6(11):p. 114801, Nov 2003

[26] N. Nekhoroshev, *An Exponential Estimate of the Time of Stability of Nearly-Integrable Hamiltonian Systems*, Russian Mathematical Surveys, 32, 1977

[27] M. Giovannozzi et al., *Inverse Logarithm Decay of Long-Term Dynamic Aperture in Hadron Colliders*, in *Proceedings of the Particle Accelerator Conference PAC97*, pp. 1445–1447, 1997

[28] V. I. Arnold et al., *Mathematical Aspects of Classical and Celestial Mechanics*, Springer, Berlin, 2nd edition, 1991, ISBN 3-540-61224-6

[29] F. Schmidt, *Untersuchung zur dynamischen Akzeptanz von Protonenbeschleunigern und ihre Begrenzung durch chaotische Bewegung*, Ph.D. thesis, 1988, DESY HESR 88-02

[30] B. Chirikov, *A universal instability of many-dimensional oscillator systems*, Physics Reports, 52(5):pp. 263 – 379, 1979

[31] J. von Milczewski et al., *Frequency Analysis of 3D Electronic* $1/r$ *Dynamics: Tuning between Order and Chaos*, Phys. Rev. Lett., 78(8):pp. 1436–1439, Feb 1997

[32] Y. Papaphilippou and J. Laskar, *Frequency map analysis and global dynamics in a galactic potential with two degrees of freedom.*, Astronomy and Astrophysics, 307:pp. 427–449, March 1996

[33] J. Laskar, *Secular evolution of the solar system over 10 million years*, Astronomy and Astrophysics, 198:pp. 341–362, June 1988

[34] R. Bartolini and F. Schmidt, *A Computer Code for Frequency Analysis of Non-Linear Betatron Motion*, SL-Note-98-017-AP, CERN, Geneva, Feb 1998

[35] J. Laskar, *Frequency analysis for multi-dimensional systems. Global dynamics and diffusion*, Physica D Nonlinear Phenomena, 67:pp. 257–281, August 1993

[36] R. B. Blackman and J. W. Tukey, *The Measurement of Power Spectra, From the Point of View of Communications Engineering*, chapter Particular Pairs of Windows., pp. 98–99, Dover, New York, 1958

[37] C. Bocchetta, *Frequency Map Analysis*, July 2003, CERN Accelerator School Lectures
URL `http://cas.web.cern.ch/cas/BRUNNEN/Bocchetta1.html`

[38] Y. Papaphilippou, *Frequency Maps of LHC Models*, in *Proceedings of the 1999 Particle Accelerator Conference PAC99*, New York, 1999

[39] PANDA collaboration, *Strong Interaction Studies with Antiprotons*, 2004, Letter-of-Intent

[40] R. Stassen et al., *COSY as Ideal Test Facility for HESR RF and Stochastic Cooling Hardware*, in *Proceedings of the Particle Accelerator Conference PAC09*, Vancouver, 2009

[41] H. Poth, *Electron cooling*, in *CERN accelerator school CERN 87–03*, volume 2, pp. 534–569, 1987

[42] D. Möhl, *Stochastic cooling*, in *CERN accelerator school CERN 87–03*, volume 2, pp. 453–533, 1987

[43] ASSIA collaboration, *A Study of SPIN-dependent Interactions with Antiprotons*, Jan 2004, Letter-of-Intent
URL `http://www.gsi.de/documents/DOC-2004-Jan-152-1.ps`

[44] PAX collaboration, *Antiproton-Proton Scattering Experiments with Polarization*, Jan 2004, Letter-of-Intent
URL `http://www.gsi.de/documents/DOC-2004-Jan-125-1.ps`

[45] F. Rathmann et al., *A method to polarize stored antiprotons to a high degree*, Physical Review Letters, 94(1), 2005

[46] A. Lehrach et al., *Polarized beams in the high-energy storage ring of the future GSI project*, in *Proceedings of the 16th International Spin Physics Symposium SPIN2004*, World Scientific, Trieste, 2004, ISBN 981-256-315-6

[47] A. Lehrach, *Strahl- und Spindynamik von Hadronenstrahlen in Mittelenergie-Ringbeschleunigern*, volume 8 of *Schriften des Forschungszentrum Jülich, Reihe Schlüsseltechnologien*, Jülich, 2008, ISBN 978-3-89336-548-7

[48] L. Groening et al., *The 70-MeV Proton Linac for the Facility for Antiproton and Ion Research FAIR*, in *Proceedings of the Linear Accelerator Conference LINAC2006*, pp. 186–188, Knoxville, 2006

[49] K. Blasche et al., *The SIS Heavy Ion Synchrotron Project*, in *Proceedings of the Particle Accelerator Conference PAC85*, volume NS-32 No. 5, IEEE Transactions on Nuclear Science, 1985

[50] P. Spiller et al., *Status of the FAIR SIS100/300 Synchrotron Design*, in *Proceedings of the Particle Accelerator Conference PAC07*, pp. 1419–1421, Albuquerque, 2007

[51] N. Tahir et al., *Design of a Target for Antiproton Production at the Future FAIR Facility*, in *High Energy Density Physics with Intense Ion and Laser Beams: Annual Report 2006*, GSI Report 2007-2, 2007

[52] A. Dolinskii et al., *Optimized lattice for the Collector Ring (CR)*, Nuclear Instruments and Methods in Physics Research A, 532:pp. 483–487, 2004

[53] P. Beller et al., *Layout of an Accumulator and Decelerator Ring for FAIR*, in *Proceedings of the European Particle Accelerator Conference EPAC06*, pp. 199–201, Edinburgh, 2006

[54] U. Bechstedt, *Status of the Main Magnets for HESR*, Talk at 26th HESR Consortium Meeting in Jülich, 2009

[55] U. Bechstedt, Forschungszentrum Jülich, private communication

[56] D. Reistad et al., *Calculations on High-Energy Elentron Cooling in the HESR*, in *Proceedings of the Workshop on Beam Cooling and Related Topics COOL07*, pp. 44 – 48, Bad Kreuznach, 2007

[57] H. Stockhorst et al., *Stochastic Cooling for the HESR at FAIR*, in *Proceedings of the Workshop on Beam Cooling and Related Topics COOL07*, pp. 30 – 34, Bad Kreuznach, 2007

[58] O. Boine-Frankenheim et al., *Cooling equilibrium and beam loss with internal targets in high energy storage rings*, Nuclear Instruments and Methods in Physics Research A, 560(2):pp. 245 – 255, 2006

[59] A. Lehrach et al., *Beam performance and luminosity limitations in the high-energy storage ring (HESR)*, Nuclear Instruments and Methods in Physics Research A, 561(2):pp. 289 – 296, 2006

[60] *HESR ELECTRON COOLER Design study*, Technical Report, The Svedberg Laboratory, 2009

[61] *Electron cooling for HESR, Technical Feasibility of Fast Electron Cooling of Antiproton Beams in the Energy Range 0.8 to 14.5 GeV*, , Novosibirsk, January 2003

[62] *Electron cooling for HESR, Second Progress Report (Technical Feasibility of Fast Electron Cooling of Antiproton Beams in the Energy Range 0.8 to 14.5 GeV)*, , Novosibirsk, 2003

[63] O. Bazhenov et al., *Electron Cooling for HESR, Final Report (Technical Feasibility of Fast Electron Cooling of Antiproton Beams in the energy range 0.8 to 14.5 GeV)*, , Novosibirsk, 2003

[64] H. Stockhorst et al., *Stochastic Cooling for the HESR at the FAIR Facility*, in *Proceedings of the Particle Accelerator Conference PAC09*, 2009

[65] R. Maier, *Cooler synchrotron COSY - performance and perspectives*, Nuclear Instruments and Methods in Physics Research A, 390:pp. 1 – 8, 1997

[66] H. Stockhorst et al., *Progress and Developments at the Cooler Synchrotron COSY*, in *Proceedings of the European Particle Accelerator Conference EPAC02*, pp. 629–631, Paris, 2002

[67] D. Albers et al., *Proton-Proton Elastic Scattering Excitation Functions at Intermediate Energies*, Phys. Rev. Lett., 78(9):pp. 1652–1655, Mar 1997

[68] V. Schwarz et al., *EDDA as internal high-energy polarimeter*, in *Proceedings of the 13th International Symposium on High-Energy Spin Physics SPIN98*, Protvino, 1998

[69] S. Barsov et al., *ANKE, a new facility for medium energy hadron physics at COSY-Jülich*, Nuclear Instruments and Methods in Physics Research A, 462(3):pp. 364 – 381, 2001, ISSN 0168-9002

[70] J. Ritman, *Experiments with the WASA detector at COSY*, Int. J. Mod. Phys., A20:pp. 525–531, 2005

[71] A. Böhm et al., *The COSY-TOF barrel detector*, Nuclear Instruments and Methods in Physics Research A, 443:pp. 238–253, 2000

[72] J. Dietrich et al., *Status of the 2 MeV Electron Cooler for COSY Juelich*, in *Proceedings of the Workshop on Beam Cooling and Related Topics COOL2009*, Lanzhou, 2009

[73] J. Dietrich et al., *Beam Profile Measurements Based On Light Radiation Of Atoms Excited By The Particle Beam*, in *Proceedings of the Particle Accelerator Conference PAC07*, pp. 3955–3957, Albuquerque, 2007

[74] J. Milutinovic and A. Ruggiero, *Closed orbit analysis for RHIC*, in *Proceedings of the 1989 IEEE Partical Accelerator Conference PAC89*, pp. 1370–1372, Chicago, 1989

[75] D. M. Welsch, *Auslegung eines Orbitkorrektursystems für den Hochenergie Speicherring HESR im Projekt FAIR*, 2006, diploma thesis

[76] G. Krol, Forschungszentrum Jülich, private communication

[77] *FAIR Baseline Technical Report - Volume 2: Accelerator and Science Infrastructure*, , Sep 2006
URL `http://www.gsi.de/documents/DOC-2006-Jul-40-1.pdf`

[78] J. Dietrich, Forschungszentrum Jülich, private communication

[79] F. Schmidt, *MAD-X PTC Integration*, in *Proceedings of the 2005 Particle Accelerator Conference PAC05*, pp. 1272–1274, Knoxville, 2005

[80] D. Oellers et al., *Polarizing a stored proton beam by spin flip?*, Physics Letters B, 674(4-5):pp. 269 – 275, 2009

[81] H. J. Stein, *Some characteristics of the electron-cooled proton beam at COSY: A first summary of experimental results from PAX runs Sept. 2008 and Feb. 2009*, April 2009, working draft

[82] J. Safranek, *Experimental determination of storage ring optics using orbit response measurements*, Nuclear Instruments and Methods in Physics Research A, 388:pp. 27–36, 1997

[83] V. Ziemann, *Resonances driven by the electric field of the electron cooler*, 1998, The Svedberg Laboratory, TSL-Note 98-43

[84] S. Sorge et al., *Studies of non-linear and collective effects relevant for HESR*, 2007, GSI Scientific Report 2006, GSI Report 2007-1

[85] D. M. Welsch et al., *Closed Orbit Correction and Sextupole Compensation Schemes for Normal-conducting HESR*, in *Proceedings of the European Particle Accelerator Conference EPAC08*, pp. 3161–3163, Genoa, 2008

[86] G. Franchetti, Helmholtzzentrum für Schwerionenforschung, private communication

[87] J. de Villiers et al., *Numerical Field Analysis of the HESR Dipole Magnet in 3D*, 2008, Internal Report

[88] J. Laskar, *Frequency Map Analysis and Particle Accelerators*, in *Proceedings of the Particle Accelerator Conference PAC03*, pp. 378–382, 2003

[89] Y. Luo et al., *Measurement and Correction of Third Resonance Driving Term in the RHIC*, in *Proceedings of 2007 Particle Accelerator Conference PAC07*

Acknowledgments

First of all, I want to express my deep gratitude to my doctoral referee Prof. Dr. Rudolf Maier. I am more than thankful to him for the great opportunity to do research and write my dissertation at the institute for nuclear physics of the Forschungszentrum Jülich. His excellent support and his trust in my capabilities and work made this thesis possible.

I thank Prof. Dr. Jens Bisplinghoff who kindly accepted to be co-referee for my thesis.

I am deeply grateful to my supervisor Priv.-Doz. Dr. Andreas Lehrach. His excellent supervision and his constructive criticism as well as his constant readiness for inspiring discussions have been essential for my thesis work. His guidance was substantial for my scientific advancement.

I have enjoyed being a member of the institute for nuclear physics and would like to thank all of its members for the friendly working atmosphere. I am especially thankful to Dr. Ulf Bechstedt, Dr. Klaus Bongardt, Prof. Dr. Dr. h.c. Jürgen Dietrich, Dr. Bernd Lorentz, Dr. Dieter Prasuhn, Prof. Dr. Yury Senichev, Dr. Rolf Stassen, Dr. Hans-Joachim Stein, Dr. Hans Stockhorst, and Dr. Raimund Tölle for their assistance, for the many fruitful discussions, and for providing inspirations.

I am also indebted to Dr. Alfredo U. Luccio and Nicholas L. D'Imperio who provided the tracking code SIMBAD as well as useful information and their help.

I sincerely thank Priv.-Doz. Dr. Frank Rathmann for provding the possibility to benchmark the closed orbit correction method at COSY during a PAX beam time.

My thanks goes also to Dr. Guiliano Franchetti for his help and for introducing me to dynamic aperture calculations.

I am very thankful to Dr. Andrea Raccanelli for proof-reading my thesis.

Finally, I express my deepest thanks to my wife Britta and to my son Max for their love, encouragement, support, and patience.

Jül-4328
August 2010
ISSN 0944-2952